Characterization of Particulate Matter Morphology and Volatility for Two Direct-Injection Engines

by

Brian Mackenzie Graves

A thesis submitted in partial fulfillment of the requirements for the degree of
Master of Science

Department of Mechanical Engineering
University of Alberta

Abstract

Particulate matter emitted from two direct injection engines has been characterized by morphology, volatility, mass-mobility exponent, effective density, and size distribution using tandem measurements from a centrifugal particle mass analyzer (CPMA) and differential mobility analyzers (DMA). The engines consisted of a heavy duty, natural gas, compression ignition engine fitted with a high pressure direct injection (HPDI) system, and a four cylinder gasoline direct injection (GDI) engine fueled with gasoline and ethanol blends. The HPDI engine was tested at six conditions which varied load, speed, EGR fraction, and fuel delivery strategy. The GDI was tested at three engine loads at 2250 RPM (4%, 13%, and 26% of maximum load) in addition to an idle condition, while it was fueled using gasoline mixed with ethanol fractions of 0% (E0), 10% (E10), and 50% (E50) by volume. An increase in engine load increased particle number concentration for both engines, but the GDI idle condition produced approximately as many particles as at 13% load. An increase in ethanol fraction in the GDI decreased number concentration, but E10 produced more particles than E0 at idle and 26% load. HPDI size distributions were log-normal whereas GDI size distributions were not log-normal and were instead skewed. The fraction of the number of purely volatile particles to total number of particles (number volatile fraction, f_N) for the HPDI engine decreased as load increased, although the low-speed, partially premixed mode had the lowest f_N. The f_N for the GDI both overall and as a function of particle mobility-equivalent diameter was under 10 percent at all engine conditions and fuels. The size-segregated ratio of the mass of internally mixed volatile material to total particle mass (f_m) was similarly low for the GDI. The f_m for the HPDI was higher; however it decreased with an increase in load and with particle mobility-equivalent diameter. HPDI effective

density was seen to collapse to approximately a single line, but engine modes with higher f_m values had slightly higher effective densities suggesting that the soot structures have collapsed into more dense shapes. Effective density and mass-mobility exponent for the GDI engine increased with load. Effective density decreased with an increase in ethanol fraction and a slight decrease in mass-mobility exponent was also observed for all conditions except idle. Effective density trends from both engines were compared to data from other GDI engines, a port fuel injection engine, and diesels, and the data is relatively similar between all engine types, with 90% of data points being within ±27% of a common trend line.

Preface

Research for this thesis is part of two collaborations, with Dr. Olfert being the lead collaborator at the University of Alberta. Chapter 2 of this thesis has been published as:

Graves, B., Olfert, J., Patychuk, B., Dastanpour, R., and Rogak, S. (2015). Characterization of Particulate Matter Morphology and Volatility from a Compression-Ignition Natural Gas Direct-Injection Engine. *Aerosol Science and Technology*. 49(8): 589–598.

I assisted in constructing the experimental setup, and was responsible for data collection and analysis, as well as manuscript composition. Ramin Dastanpour, Bronson Patychuk, and Dr. Olfert assisted with data collection (Ramin Dastanpour was also responsible for all aspects of the TEM work), while Dr. Rogak was involved in concept formation. All authors contributed to manuscript edits. A similar version of chapter 3 of this thesis will be submitted to the Journal of Aerosol Science. I collaborated with Dr. Olfert and Dr. Koch in designing the experimental setup and was responsible for its construction. I also performed the data collection and analysis, and prepared the manuscript. Dr. Olfert provided manuscript edits. The literature review in chapter 1 and the discussion and conclusions in chapter 4 are my original work.

Table of Contents

Appendices

List of Tables

List of Figures

List of Variables

A	Vehicle frontal area
a	Acceleration
α	Percentage of power lost through vehicle powertrain
β	Dilution ratio
C	Prefactor for mass-mobility relation
C_{U}	Prefactor for undenuded mass-mobility relation
C_1	Amplitude coefficient in sigmoidal fit
C_2	Horizontal stretch coefficient in sigmoidal fit
C_3	Horizontal offset coefficient in sigmoidal fit
C_4	Vertical offset coefficient in sigmoidal fit
C_{d}	Drag coefficient
C_{rr}	Rolling resistance coefficient
$\mathrm{dlog}d_{\mathrm{m}}$	Mobility-equivalent diameter bin width
$\mathrm{dlog}d_{\mathrm{m,U}}$	Mobility-equivalent diameter bin width for undenuded particles
$\frac{\mathrm{d}M}{\mathrm{dlog}d_{\mathrm{m}}}$	Mass concentration normalized by bin width
$\left(\frac{\mathrm{d}M}{\mathrm{dlog}d_{\mathrm{m}}}\right)_{\mathrm{internal\ volatile}}$	Normalized mass concentration of internally mixed volatile material
$\left(\frac{\mathrm{d}M}{\mathrm{dlog}d_{\mathrm{m}}}\right)_{\mathrm{external\ volatile}}$	Normalized mass concentration of externally mixed volatile material
$\left(\frac{\mathrm{d}M}{\mathrm{dlog}d_{\mathrm{m}}}\right)_{\mathrm{non-volatile}}$	Normalized mass concentration of non-volatile material
D_{m}	Mass-mobility exponent
$D_{\mathrm{m,U}}$	Mass-mobility exponent for undenuded particles
d_{m}	Mobility-equivalent diameter
$d_{\mathrm{m,U}}$	Undenuded mobility-equivalent diameter
$\frac{\mathrm{d}N}{\mathrm{dlog}d_{\mathrm{m}}}$	Number concentration normalized by bin width
$\frac{\mathrm{d}N_{\mathrm{U}}}{\mathrm{dlog}d_{\mathrm{m,U}}}$	Normalized number concentration of undenuded particles

d_{side}	Fractional thickness of tire sidewall
d_{tire}	Width of tire
d_{wheel}	Diameter of wheel
F_0	Coefficient in empirical road load equation
F_1	Coefficient in empirical road load equation
F_2	Coefficient in empirical road load equation
F_{aero}	Force due to aerodynamic drag
F_{inertia}	Force due to acceleration
f_{m}	Mass volatile fraction
f_{N}	Number volatile fraction
$F_{\mathrm{Road\ load}}$	Force between tires and road surface
F_{Rolling}	Force due to rolling resistance
f_{v}	Volume volatile fraction
g	Gravitational acceleration
k	Prefactor for mobility-equivalent diameter and effective density relation
M	Particle mass concentration
$M_{\mathrm{non-volatile}}$	Mass concentration of non-volatile material
M_{volatile}	Mass concentration of volatile material
M_{m}	Molar mass
m	Individual particle mass
m_{denude}	Mass of particle when passed through denuder heating line
m_{undenude}	Mass of particle when passed through denuder bypass line
$\dot{m}_{\mathrm{da}}$	Mass flow rate of dilution air
$\dot{m}_{\mathrm{DMA}}$	Mass flow rate of sample through DMA
$\dot{m}_{\mathrm{Makeup}}$	Mass flow rate of makeup air
N_1	Number concentration upstream of diluter (undiluted)
N_2	Number concentration downstream of diluter (diluted)
N_{denude}	Number concentration through denuder heating line

$N_{\text{non-volatile}}$	Number concentration of non-volatile particles
N_{undenude}	Number concentration through denuder bypass line
N_{volatile}	Number concentration of purely volatile particles
η_{denude}	Transmission efficiency through thermodenuder
η_{dilute}	Transmission efficiency through diluter
P	Air pressure
P_{Trac}	Tractive power
R	Universal gas constant
R_{A}	Axle ratio
R_{T}	Transmission gear ratio
r_{w}	Radius of wheel and tire assembly
ρ	Air density
ρ_{eff}	Effective density
T	Temperature
T_{Engine}	Torque applied by engine crankshaft
$\vec{V}$	Velocity of vehicle
φ_1	Upstream (undiluted) concentration of gas
φ_2	Downstream (diluted) concentration of gas
φ_{da}	Gas concentration in dilution air stream
ω_{Engine}	Engine rotational velocity

List of Acronyms

AFR	Air-to-fuel ratio
AKI	Anti-Knock Index
ANCOVA	Analysis of Covariance
CO	Carbon Monoxide
CO_2	Carbon Dioxide
COPD	Chronic Obstructive Pulmonary Disease
CPC	Condensation Particle Counter
CPMA	Centrifugal Particle Mass Analyzer
DMA	Differential Mobility Analyzer
DOC	Diesel Oxidation Catalyst
DPF	Diesel Particulate Filter
EGR	Exhaust Gas Recirculation
EPA	Environmental Protection Agency
EQR	Equivalence Ratio
GDI	Gasoline Direct Injection
GIMEP	Gross Indicated Mean Effective Pressure
GMD	Geometric Mean Diameter
GPF	Gasoline Particulate Filter
GRP	Gas Rail Pressure
HC	Hydrocarbon
HPDI	High Pressure Direct Injection
MON	Motor Octane Number
NEDC	New European Driving Cycle
NO_x	Nitrogen Oxides
PFI	Port Fuel Injection
PM	Particulate Matter
RON	Research Octane Number
SCRE	Single Cylinder Research Engine
SMPS	Scanning Mobility Particle Spectrometer
STEM	Scanning Transmission Electron Microscopy

TDC	Top Dead Center
TEM	Transmission Electron Microscopy
TPS	Thermophoretic Particle Sampler
TWC	Three-Way Catalyst
WHSC	World Harmonized Steady Cycle
WHTC	World Harmonized Transient Cycle

Acknowledgements

I would like to thank Dr. Olfert for his guidance, advice, patience, and support over the course of my studies. He has been hugely helpful technically and otherwise, and is always relaxed, positive, and encouraging. My knowledge, abilities, and confidence have all improved as a result. His ability to give his students independence and responsibility while still being accessible is greatly appreciated by everyone in the research group. I couldn't ask for a better supervisor!

Thank you to Daniel Stang and Dr. Koch for their help and advice on running the engine, as well as to everyone else in the research group who has contributed over the past two years. Also, a huge thank you to Bernie Faulkner for the help with the setup and troubleshooting. His knowledge and experience have been invaluable.

Finally, thank you to all my friends and family for keeping me balanced and grounded. I also need to extend my gratitude to my parents and girlfriend for their support, love, and understanding. They have been with me every step of the way, and I certainly wouldn't be where I am without them. I am forever grateful.

1. Introduction

1.1 Particulate Matter from Engines

Particulate matter (PM) produced from internal combustion engines consists mainly of solid carbonaceous aggregates and volatile organic material. Solid elemental carbon primary particles form during incomplete combustion. These primary particles agglomerate into larger aggregate structures which grow in fractal-like patterns, similar to the non-volatile aggregates in Figure 1.1. The mass (m) of these particles scales with mobility-equivalent diameter (d_m) as

$$m = C {d_\mathrm{m}}^{D_\mathrm{m}} . \qquad 1.1$$

D_m is the mass-mobility exponent and C is a prefactor. The mass mobility exponent is useful for describing the structure of the aggregate particles (Abegglen et al., 2015). Particle samples with large mass-mobility exponents (near the maximum value of 3) will be compact and relatively spherical, whereas lower mass-mobility exponents are associated with more branched aggregates that contain more open space.

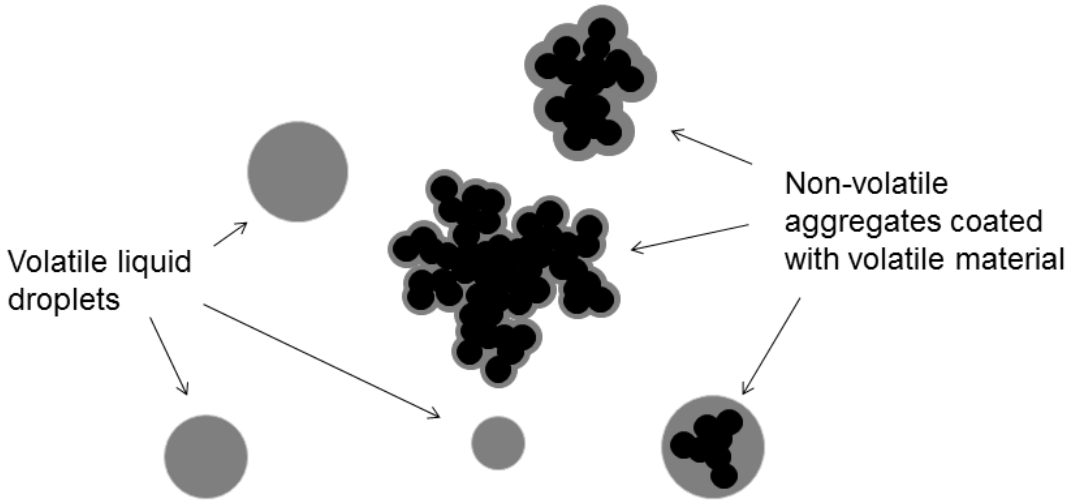

Figure 1.1: Volatile and non-volatile PM from engine.

Volatile material is often composed of unburned fuel or engine oil (Maricq, 2007). This material can coat non-volatile aggregate particles as well as form separate droplets, as seen in Figure 1.1. When volatile material coats the non-volatile particles, it tends to smooth the contours of the particle, and if enough volatile material is present, it can form a droplet around the solid aggregate core. The volatile coating makes the

particle more spherical and increases the mass-mobility exponent (up to 3 in the case of a spherical droplet). Likewise, comparison of the mass-mobility exponent for unconditioned particles and after conditioning the sample to remove volatile material gives an indication of the proportion of volatile material to non-volatile material and thus the composition of the PM sample.

Example number size distributions for PM containing both volatile and non-volatile material are shown in Figure 1.2. Number concentrations (*N*) are normalized by diameter bin width $\left(\frac{\mathrm{d}N}{\mathrm{dlog}d_{\mathrm{m}}}\right)$. The overall distribution is comprised of two distributions which are often referred to as the nucleation and accumulation modes. The distribution at the smaller size contains purely volatile particles (nucleation mode), and the distribution at the larger size contains aggregate particles (accumulation mode). The individual distributions are often log-normal (Kittleson, 1998), although depending on their relative sizes and positions the total distribution may show the two peaks (Figure 1.2a) or it may appear as a single distribution that is more broad or skewed (Figure 1.2b).

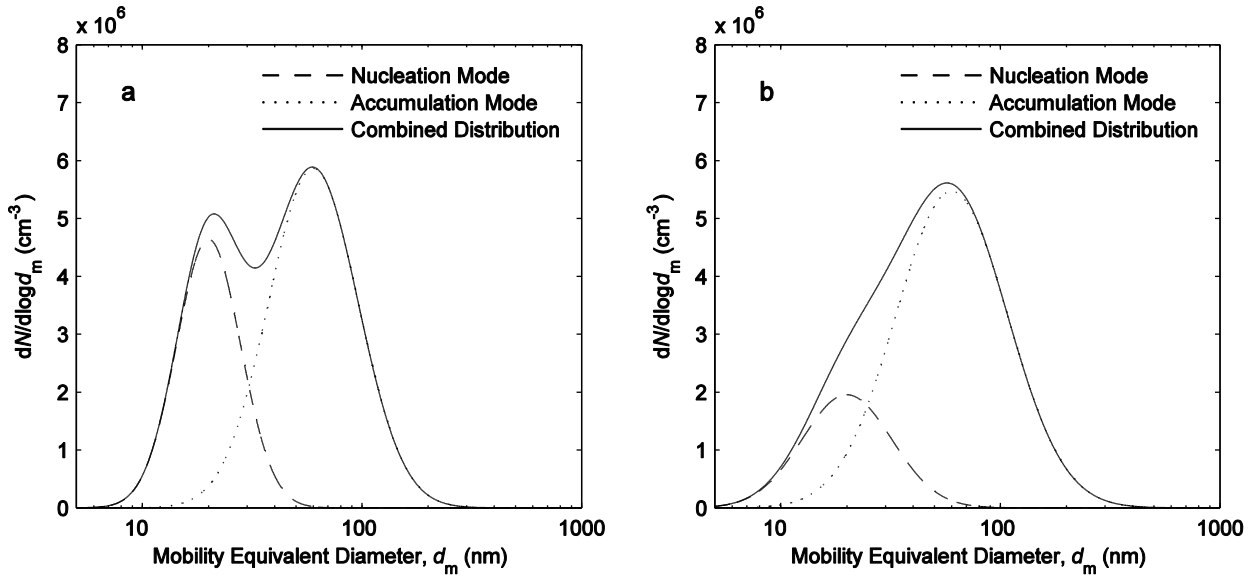

Figure 1.2: Example size distributions of PM sample containing volatile and non-volatile species. (a) has a significant nucleation mode and (b) has a smaller nucleation mode.

1.2 Fuel Injection and Particulate Matter

The method by which fuel is delivered to an engine has a large effect on the combustion characteristics (Stone, 2012). As a result the performance, efficiency, and emissions are all sensitive to fuel injection properties. Most diesel engines use direct fuel injection, whereas gasoline engines have traditionally used port injection but have transitioned to direct injection as well. Direct fuel injection offers advantages over port injection in relation to efficiency and performance; however their particulate matter number and mass emissions are higher (Khalek et al., 2010; Stone, 2012). This is largely because fuel is not mixed homogeneously with the air and PM is formed in locally fuel-rich zones (Steimle et al., 2013). Work must be done to understand these PM emissions and the mechanisms by which they are formed.

1.2.1 Port Fuel Injection Engines

Before gasoline engines adopted direct fuel injection, port fuel injection (PFI) was the common method of fuel delivery (Zhao et al., 1997). In a PFI engine, fuel is injected in the intake manifold, upstream of the intake valves, as seen in Figure 1.3. This provides a relatively long time for fuel droplets to evaporate and mix with the air, and typically results in a well-mixed, homogeneous charge. Because of the long time available for fuel mixing, port injectors operate at lower pressures than direct injectors (Liang et al., 2013). The homogeneous nature of the charge also means that port injection engines must operate on a narrow range of equivalence ratios (EQR) so that the mixture is flammable near the spark plug (and so the catalyst can reduce pollutants most effectively). Unlike a diesel engine for example, PFI engines are not able to run very lean, so at part load the intake manifold pressure must be throttled, which results in flow and heat losses, and can reduce engine efficiency.

The excellent fuel mixing properties of port fuel injected engines and the scarcity of locally fuel-rich zones where incomplete combustion can occur also means they are light emitters of PM. PFI engines have been seen to produce less PM than gasoline direct injection (GDI) engines (Oh and Cha, 2012; Bielaczyc et al, 2014; Karavalakis et

al., 2014a; Karavalakis et al., 2015). The PM emissions from port injection engines are partly composed of elemental carbon soot aggregates. They contain small primary particles that have agglomerated to form larger fractal-like particles, which resemble the non-volatiles in Figure 1.1. Alger et al. (2010) and Karavalakis et al. (2014b) have also found a significant amount of volatile material present in the PM. Saeed et al. (2014) noted that the majority of particles observed through scanning transmission electron microscopy (STEM) were aggregates with primary particle diameters between 18-59 nm; however they did notice evidence of liquid material which could have originated from engine oil, as well as a small number of what appeared to be salt particles. Su et al. (2013) found the size distributions to be bimodal with a clearly distinguishable nucleation and accumulation modes, regardless of engine load. The nucleation mode had a geometric mean diameter (GMD) of about 10 nm whereas the accumulation mode's GMD was approximately 65 nm.

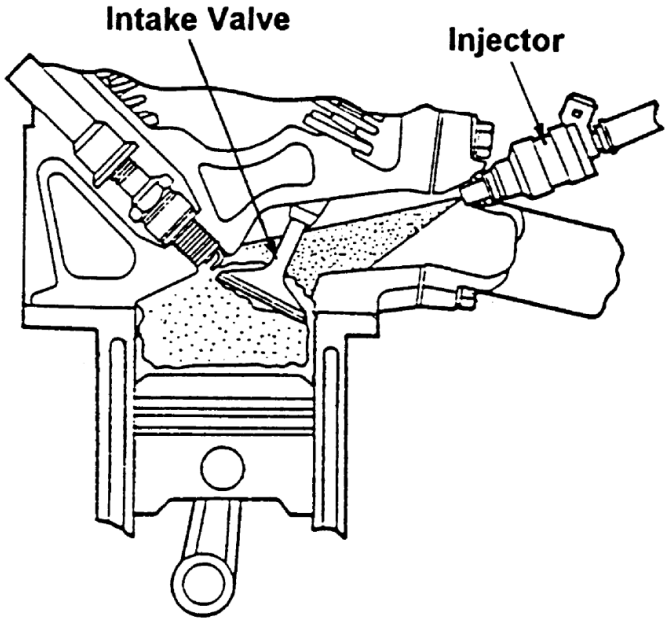

Figure 1.3: Port fuel injection schematic. Fuel is injected in the intake manifold (Zhao et al., 1999).

1.2.2 Diesel Engines

A diesel cylinder schematic is shown in Figure 1.4. Without a spark plug, diesel engines (those which don't use glow plugs) rely on direct injection to control ignition. The fuel injection in a diesel engine occurs at the end of the compression stroke, near

top dead centre (TDC). At this point, the air is highly compressed and very hot, so the fuel ignites immediately as a diffusion flame upon entering the cylinder. This provides a small time interval for fuel evaporation and mixing, so diesel injectors operate at extremely high pressure to atomize fuel into smaller droplets which evaporate more quickly (e.g. 1600 bar, Gupta et al., 2014). Unlike spark ignition engines, diesel engines control load by the amount of fuel injected rather than by manipulating manifold air pressure. At low loads, a small amount of fuel is injected, yet it is still able to ignite because the local AFR (around the fuel spray) is unchanged, even if overall the combustion is lean. This eliminates flow losses incurred from restricting manifold air pressure, and the excess air in the exhaust can be used to oxidize organic emissions.

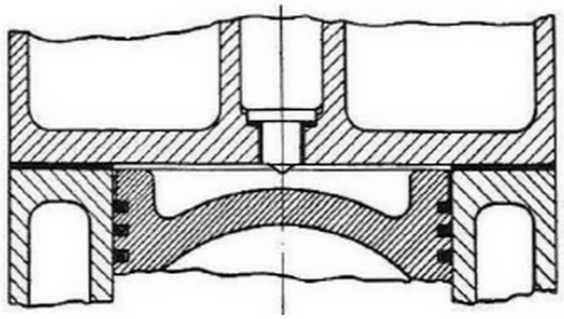

Figure 1.4: Diesel injection schematic. The injector is located above the center of the piston (Stone, 1999).

Because diesel combustion takes place in a local region surrounding the fuel spray, parts of the combustion occur under locally rich conditions, even if the overall equivalence ratio is lean. This results in higher levels of PM than from PFI. It is these small regions of fuel-rich combustion which produce the largest portion of PM. The majority of this PM is typically fractal-like elemental carbon aggregates comprised of primary particles between 15-40 nm in diameter (Burtscher, 2005). Other constituents are ash, organic liquid from unburned fuel or engine oil, and depending on the fuel, sulfur compounds (although these are less prevalent with new fuels which contain less than 10 ppm sulfur, EU, 2003). The size of particles are often log-normally distributed and normally have a GMD between 60 and 100 nm, although depending on the relative prominence of other PM species (especially volatile organic droplets) a second peak can be observed (Burtscher, 2005). Young et al. (2012) observed unimodal distributions with a peak at 75 nm while at load; however at no load the peak of the distribution was

39 nm. Moreover, after heating the sample to remove any volatile material, the peak at no load reduced to 15 nm along with a 57% reduction in number concentration. These are indications that volatile material is present in the PM, and is both coating the non-volatile particles (hence the reduction in particle size after thermal conditioning) as well as forming particles comprised solely of volatile material (removal of these particles is responsible for the reduction in number concentration). Chuepeng et al., (2011) found bi-modal distributions over a range of operating conditions. On average, the count mean diameters of the nucleation and accumulation modes were 38 nm and 102 nm. Sakurai et al. (2003) also found bi-modal distributions, and noted that the nucleation mode was highly volatile whereas the accumulation mode contained particles with non-volatile cores. The relative amount of volatile material coating these non-volatile cores can vary with particle size. A decreasing trend was observed by Sakurai et al. (2003) using volatile volume fractions and by Ristimäki et al. (2007) using volatile mass fractions, yet an increase in the volatile content with particle size was seen by Park et al. (2004) by observing the change in inherent material density.

1.2.3 Gasoline Direct Injection Engines

A schematic of GDI injection is displayed in Figure 1.5. GDI engines offer a range of combustion strategies that are not available for port injection engines. Fuel can be injected during the intake stroke, in which case it will have more time to mix with the air, and the charge will be largely premixed. Alternatively, fuel can be injected during the compression stroke, leaving less time for the air and fuel to mix and resulting in a more heterogeneous charge (in general, fuel injection in a GDI occurs earlier than for a diesel, so injection pressures tend to be lower, although still higher than PFI injectors). This stratified charge results in a flammable mixture in the vicinity of the spark plug even if the overall equivalence ratio is lean. This can increase fuel efficiency because intake air does not need to be throttled to the same extent as with a homogeneous charge, and less heat is lost due to the smaller amount of fuel injected (Stone, 2012). In addition to airborne droplets reducing the heterogeneity of the charge, fuel may be inadvertently sprayed onto surfaces such as the piston head, cylinder walls, and valves. Here, pools of liquid fuel can form which create local fuel-rich zones due to a high concentration of

fuel as it evaporates. Once again, this results in higher PM production. This can be a particularly difficult issue to overcome for a GDI engine due to the variability in injection timing. If fuel is injected during the intake stroke, fuel may impinge on the open intake valve. In this instance, a narrower spray cone angle may be beneficial to direct fuel past the valve. It is also possible for fuel to impinge on the piston head, especially if injection occurs when the piston is near TDC (Steimle et al., 2013). Precise control of injection timing and spray properties is needed to ensure fuel impingement and pool formation are minimized for as many engine conditions as possible (Steimle et al., 2013).

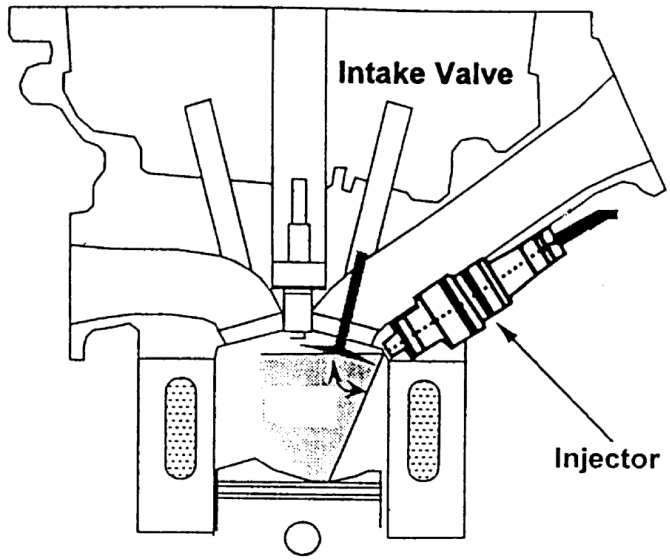

Figure 1.5: GDI injection schematic (Zhao et al., 1999).

As with diesel engines, PM emissions from GDIs are significantly higher than PFI engines (Khalek et al., 2010; Liang et al., 2013; Bielaczyc et al., 2014; Karavalakis et al., 2014a), and this presents strong motivation to characterize these emissions in an effort to mitigate them. Similar to diesel engines, GDIs produce elemental carbon aggregates which can be mixed with organic liquid material. The relative amount of organic material has been found to be high pre-catalyst (Storey et al., 2010), with mass-based organic carbon to elemental carbon ratios ranging from approximately 2 to 50 depending on operating condition and fuel composition; however this ratio was much lower after the catalyst (<0.5). Maricq et al. (2012) also found tailpipe-out PM to be primarily elemental carbon. The volatile or semi-volatile liquids can be present as separate droplets or they can coat the solid aggregates. Momenimovahed and Olfert

(2015) found that the amount of volatile material in relation to the total particle mass increased as tractive power increased, and that the relative amount of volatile material decreased as mobility-equivalent diameter increased. They also found mass-mobility exponents of 2.4 to 2.7 for undenuded particles and 2.5 to 2.7 for denuded particles. Quiros et al. (2015) observed mass-mobility exponents of 2.45±0.05, which decreased to 2.30±0.02 at higher loads.

Chen et al. (2012) saw bimodal size distributions in both their pre and post-catalyst measurements, although post-catalyst distributions contained smaller nucleation modes. Catapano et al. (2013) found particle size distributions which were bimodal and had a large nucleation mode (without the use of a catalyst); whereas others have observed size distributions which were unimodal (Gu et al., 2012; Zhang et al., 2014).

1.3 Effects of Particulate Matter

Particulate emissions have potential negative impacts on health and the environment. PM is ranked as the 13th most common cause of death (responsible for approximately 800 000 deaths yearly) (Anderson et al., 2012). Moreover, it was predicted that in 2012 3.7 million premature deaths worldwide were caused by exposure to PM smaller than 10 μm (WHO, 2014). In 2008, it was predicted that 21 000 Canadians died from causes linked to air pollution, and the effects of air pollution are estimated to be $8 billion (CMA, 2008). Sufficiently small particles are able to penetrate into the body through the lungs and intestines, and can deposit for long periods of time. Depending on their size, shape, and chemistry, the particles can result in a host of potential negative health effects on many organs (Hoet et al., 2004; Balasubramanian et al., 2010). PM exposure has been correlated with negative effects on cardiovascular and cerebrovascular health, as well as respiratory diseases through systemic inflammation, coagulation activation, and translation into systemic circulation (Anderson et al., 2012). Miller et al. (2007) found that increased long-term exposure to PM resulted in a 24% increase in cardiovascular incidents for postmenopausal women. Moreover, a 76% increase in cardiovascular-related deaths was observed. Likewise, a decrease in black smoke concentration of 35.6 μg/m^3 following a sales ban of bituminous coal

resulted in a decrease in respiratory and cardiovascular mortality of 15.5% in the area (Clancy et al., 2002). Potential links to increased frequencies of asthma, chronic obstructive pulmonary disease (COPD), and reduced lung function for people with cystic fibrosis have also been reported (Anderson et al., 2012), and negative effects specifically from automotive PM have been inferred by Riediker et al. (2004).

PM can also potentially contribute toward climate change through several mechanisms, and its effects on radiative forcing are compared in Figure 1.6. Particles scatter solar radiation; preventing it from being transmitted to the earth surface. However, carbon particles absorb radiation, and the resultant energy heats the atmosphere (Boucher et al., 2013), although this effect is not as significant as radiation scattering. As a result, a net cooling effect is observed from aerosol-radiation interaction (IPCC, 2013). Elemental carbon may also increase the albedo of the area, particularly when the terrain is composed of elements with high albedos such as snow or ice. This increases the amount of radiation absorbed and has a small positive effect on radiative forcing. The particles have an indirect effect on the climate as well: they can act as nucleation sites for water droplets, which leads to increased cloud formation (Albrecht, 1989; Giordano et al., 2015). As clouds have relatively high albedos, more solar radiation is reflected which results in a cooling effect of a similar magnitude to the aerosol-radiation interaction.

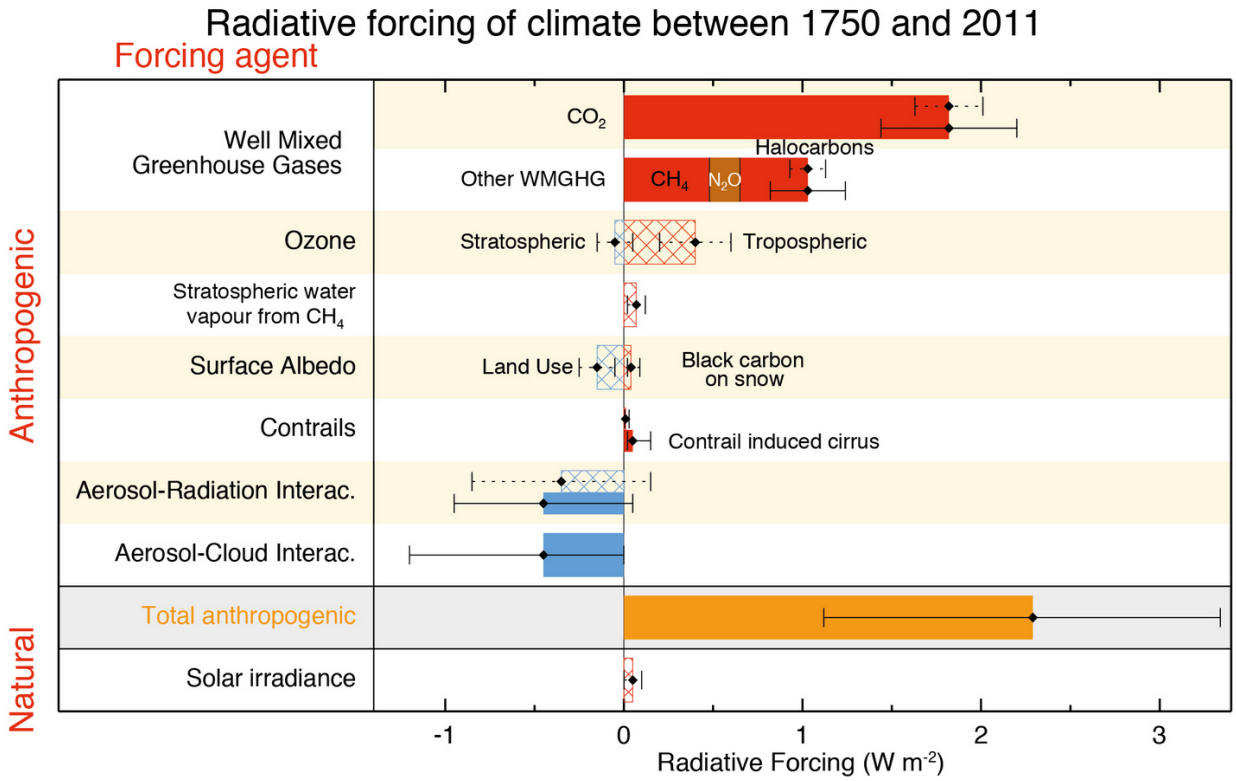

Figure 1.6: Comparison of agents on global radiative forcing. Hatched bars represent radiative forcing and solid bars represent effective radiative forcing (IPCC, 2013).

1.4 Emission Regulations

Euro 5 regulations limited particle mass from light duty vehicles (both compression ignition and spark ignition) to 4.5 mg/km for the New European Driving Cycle (NEDC) (Giechaskiel et al., 2014), although the first installation of Euro 5 (Euro 5a) did not invoke any regulations on particle number (EEA, 2007). With the introduction of Euro 5b, compression ignition vehicles were limited to particle number emissions of 6×10^{11} /km (EEA, 2008). Current Euro 6 regulations (introduced September 2014) have not altered particle mass limitations but have imposed a number regulation of 6×10^{11} /km for direct injection spark ignition vehicles (EEA, 2012). This particle limit is extended to 6×10^{12} /km for direct injection vehicles for the first three years following Euro 6 implementation.

Euro 6 heavy duty vehicles are to be tested on the World Harmonized Transient and Steady Cycles (WHTC and WHSC, respectively) and held to regulation UN/ECE 49 which limits mass emissions to 10 mg/kWh. Number emissions are limited to 6×10^{11} /km for the WHSC cycle and 8×10^{11} /km for the WHTC cycle (Giechaskiel et al., 2014).

American regulation Tier 3 regulations do not have a number limit, but restrict light duty mass emissions to 3 mg/mile on the FTP cycle and 10 mg/mile on the US06 cycle. Heavy duty vehicles must meet a mass emission level of 10 g/bhp/h (Giechaskiel et al., 2014).

1.5 Abatement

Measures can be taken with engine control to reduce PM emissions to meet the above regulations. Allowing more time for the fuel to mix with the air before combustion reduces fuel-rich zones and can significantly lower PM concentrations. This can be done by injecting fuel early or by delaying ignition (Steimle et al., 2013; Su et al., 2013; Pei et al., 2014). An increase in exhaust gas recirculation (EGR) fraction has also been seen to improve PM emissions from gasoline direct injection (GDI) engines (Hedge et al., 2011; Sabathil et al., 2011; Pei et al., 2014), although EGR has also been seen to increase PM mass emissions for a direct injection natural gas engine (Patychuk and Rogak, 2012).

Reductions in PM can also be made in the exhaust. Volatile organic material can be oxidized using a catalytic converter. Diesel engines use diesel oxidation catalysts (DOC) (pictured in Figure 1.7) which are usually coated in metals within the platinum group (platinum, palladium, rhodium) (Stone, 1999). The catalyst reacts CO, unburned hydrocarbons, and volatile particles in conjunction with excess air in the exhaust. An active technique known as selective catalytic reduction can also be used to eliminate some of these organic species, although its primary function is to remove oxides of nitrogen, or NO_x (typically for diesel engines). For gasoline engines, a three-way catalyst (TWC) is used. Its name is derived from the three gaseous species it removes (CO, unburned hydrocarbons, and oxides of nitrogen or NO_x), although it also oxidizes

volatile PM. The portion which removes NO_x is a reduction catalyst, whereas removal of organic species is done with an oxidation catalyst.

A catalytic converter is advantageous because there is relatively little impedance to the exhaust flow so performance and efficiency are not compromised. However, the catalyst must be hot to attain good conversion efficiency (Stone, 1999), so performance at low load for diesel engines can suffer. Several advanced strategies are available to keep the catalyst temperature above the necessary lightoff temperatures of its various target species. The injection of fuel late in the power stroke or into the exhaust can provide enough reactive material (unburned fuel) that the heat from its oxidation is sufficient to keep the temperature above lightoff (Wirojsakunchai et al., 2009). Although not used in practise, a system of valves can be used to periodically reverse the exhaust flow direction to keep all portions of the catalyst sufficiently hot (Liu et al., 2000; Wirojsakunchai et al., 2009). A caveat for this method is that the exhaust must be hot enough to keep at least the first portion of the catalyst above lightoff, as no new energy is added to the system. Finally, the catalyst can be heated electrically (Liu et al., 2000). These advanced techniques are of greater importance for reduction of gaseous emissions (especially methane), as it has been shown that the effective lightoff temperature for PM is lower than for gaseous species (Whelan et al., 2013). Nevertheless, at low power, benefits may be seen in regard to PM reduction as well.

In the case of elemental carbon, it is too inert to react unless temperatures are high (oxidation occurs readily above 600°C, Goldenberg et al., 1983), so a filter is necessary. Diesel particulate filters (DPF) like that shown in Figure 1.7 can achieve filtration efficiencies of at least 85% (EPA, 2010), although periodically the trapped soot must be oxidized to regenerate the filter. This happens to some extent at high loads when exhaust temperatures are elevated (passive regeneration); however in many cases active regeneration is also necessary. Fuel is injected late in the combustion stroke or into the exhaust, and its oxidation results in temperatures which are sufficiently high to oxidize the PM and regenerate the DPF. The process produces some CO_2 and a small amount of residual ash. DPFs add resistance to the exhaust flow; so power and

efficiency penalties may be observed. As such, PM mitigation strategies which involve prevention of PM formation rather than removal of existing PM are desirable. These include control methods as mentioned above, as well as novel fuels and engine technologies.

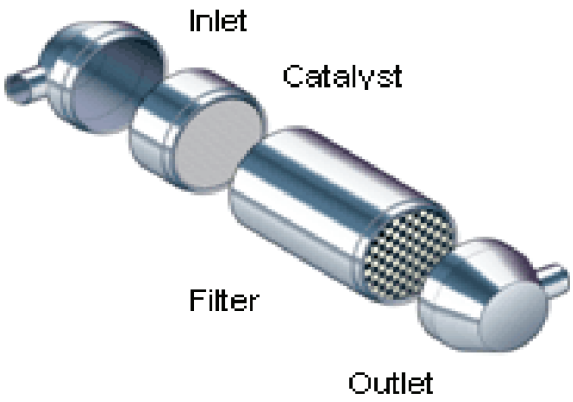

Figure 1.7: DOC and DPF schematic (EPA, 2010).

1.6 Research Overview and Implications

In this research, PM emissions from two direct injection engines were studied: a natural gas compression-ignition engine fitted with a high pressure direct injection (HPDI) system, and a spark-ignition, GDI engine. A CPMA and tandem differential mobility analyzers were used to characterize the PM emissions with regard to size distributions, mass-mobility exponents, effective densities, volatility, and mixing state. Information gleaned concerning particle morphology and volatility is useful for choosing suitable exhaust aftertreatment and can be used to determine mass concentrations using methods such as the integrated particle size distribution (IPSD) technique which can be much faster than gravimetric methods. Moreover, knowledge of the PM morphology from the HPDI engine can help distinguish any differences between natural-gas HPDI soot and diesel soot, which can be useful when assessing the value of introducing more natural gas vehicles in the heavy duty fleet. The GDI was tested using various fractions of ethanol mixed with gasoline. This research will contribute to the ongoing debate regarding the potential for ethanol to reduce PM emissions, and will elucidate the effects ethanol has on the particles themselves. Should new regulations

for PM emissions or fuel composition be put in place, this work will help determine the steps which must be taken to control GDI emissions.

1.7 Thesis Organization

This thesis is comprised of four chapters. Chapter 2 discusses the HPDI experiments, and Chapter 3 is dedicated to GDI experiments. Finally Chapter 4 offers an overall discussion and summary, and presents conclusions based on both data sets.

2. Characterization of Particulate Matter Morphology and Volatility from a Compression-Ignition Natural-Gas Direct-Injection Engine

2.1 Introduction

Despite the many benefits of compression-ignition engines, they tend to produce a large amount of particulate matter (PM) in comparison to port-injected spark ignition engines (Fujita et al., 1995). The PM can have potential adverse effects on the environment and human health, and as a result, emissions regulations are becoming increasingly stringent (Johnson 2012). While the combustion of natural gas tends to produce a lower amount of PM than diesel fuel, it is still important to understand these emissions, both quantitatively and qualitatively. The nature of the particles emitted may dictate the type of exhaust after-treatment that is used on natural-gas compression-ignition engines.

The High-Pressure Direct-Injection (HPDI) system uses natural gas and diesel fuel at pressures up to 300 bar. Both fuels are introduced using concentric passages with separate holes on the same injector, as seen in Figure 2.1. Near top dead center (TDC), the diesel pilot is injected (approximately 5% of the total energy; panel a), and autoignites. The natural gas is then injected (panel b) and is ignited by the diesel pilot flame. The natural gas combustion is predominately unmixed, which helps avoid knock and allows for a high-compression ratio and thermal efficiency, like those associated with diesel engines (McTaggart-Cowan et al. 2012). In this engine, soot particles are mainly formed by incomplete combustion of natural gas (Jones 2004). Strategies to reduce PM (reviewed below) resemble those used for conventional diesel engines. In contrast, “dual-fuel” or “fumigated” engines use late-cycle diesel injections (Wong et al. 1991; Mustafi et al. 2010) to ignite natural gas that is mixed with the intake air. In fumigated engines, soot emissions are almost entirely due to the diesel fuel, while the premixed charge gives rise to NOx, CO, and HC emissions resembling those of spark-ignited engines. Because the HPDI system allows independent control of the gas and diesel injections, it is possible to inject the gas earlier than the diesel pilot, producing

conditions that are closer to the fumigated natural-gas engine. One of these conditions is included in the experiments described in this chapter.

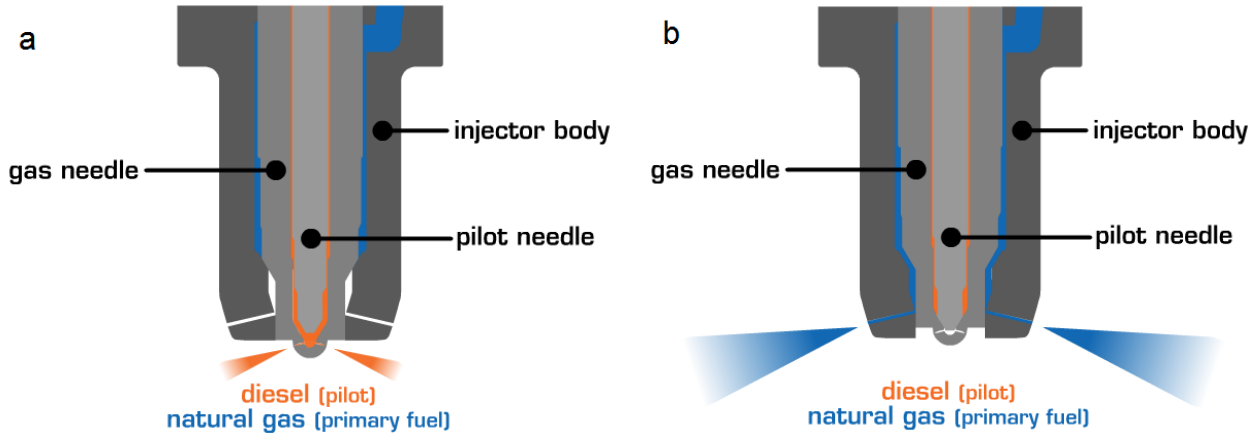

Figure 2.1: HPDI injector schematic depicting diesel pilot injection (a) and primary natural gas injection (b) (Westport Innovations Inc., 2015).

Several studies have already been conducted on this single cylinder research engine (SCRE) equipped with an HPDI fuel system. Patychuk and Rogak (2012) studied PM mass, size, and composition while varying equivalence ratio (EQR), gas rail pressure (GRP), exhaust gas recirculation (EGR), injection timing, and diesel injection mass for a mid-speed (1500 RPM), high load (16.5 bar gross indicated mean effective pressure [GIMEP]) engine condition. They determined that PM mass emissions were affected primarily by EGR and EQR, and PM number emissions were also affected by EGR and EQR, and less strongly by GRP and diesel pilot quantity.

McTaggart-Cowan et al. (2012) worked to reduce the PM mass emissions for the same engine mode used by Patychuk and Rogak (2012). They found that PM could be reduced by adjusting the relative phasing of the diesel and natural gas injections to allow for more premixing of the natural gas with air. In addition, a reduction in pilot mass to increase ignition delay and lower EGR levels also helped. These conditions were also found to reduce CO, but increased the levels of unburned hydrocarbons and NOx. The reduction in pilot injection mass significantly reduced PM for a given NOx level at high load, although not much effect was seen at low load. They determined that optimized

conditions give a large reduction in PM while sacrificing some NOx emissions. A smaller improvement in PM emissions is possible with no NOx cost.

Faghani et al. (2013) also investigated methods of reducing PM levels from this engine. They determined that a split gas injection strategy where 15–20% of the natural gas is injected 1.5–2.5 ms after the end of the first injection can reduce PM and CO emissions by 80%. Methane emissions were also reduced, NOx did not seem to be affected, and fuel consumption increased marginally (~1%).

Patychuk (2013) observed the effects of engine speed and load, injection timing, EQR, EGR, GRP, diesel injection mass, and amount of fuel premixing (fuel premixing is where some of the natural gas is injected into the cylinder before the diesel pilot and given time to mix before ignition) on the morphology of the PM emissions. An increase in engine load increased particle mass and number concentrations. Engine speed showed the same trends, although a weaker relationship was seen. Mean particle size also increased with load, and mass and number volatile fractions (f_m and f_N) decreased. At single mode operation, EQR, variations in GIMEP, and GRP had the largest bearing on PM mass emissions. Overall, primary particle size exhibited a weak negative correlation with speed, although there was a positive correlation for mid and high loads between the low and mid speeds (1200 RPM and 1500 RPM). Primary particle size was also seen to correlate positively with aggregate size (Dastanpour and Rogak 2014).

For these experiments, we studied PM morphology and volatility in more detail through size-segregated particle mass, measured using a centrifugal particle mass analyzer (CPMA), and through transmission electron microscopy (TEM). The CPMA classifies particles based on mass-to-charge ratio (Olfert and Collings 2005). The CPMA (or a related instrument, the aerosol particle mass analyzer, APM) has been used to measure the mass-mobility relationship of particles emitted from several engines including: diesel engines (Park et al. 2003; Olfert et al. 2007; Barone et al. 2011), natural-gas fueled homogenous-compressed charge-ignition engines (Bullock and Olfert 2014), and aircraft turbines (Durdina et al. 2014; Johnson et al. 2015).

TEM is a commonly accepted ex-situ method for direct characterization of the soot morphology (Medalia and Heckman 1969; Rogak et al. 1993; Brasil et al. 1999; Dastanpour and Rogak 2014; Seong et al. 2014). Primary particle diameter, aggregate maximum length and width, projected area equivalent diameter, and gyration radius can be measured from these images. Three-dimensional morphology parameters, e.g., number of the primary particles in individual particles, can be inferred from these two-dimensional parameters (Rogak et al. 1993; Brasil et al. 1999; Park et al. 2004; Tian et al. 2007).

In this article, a CPMA, TEM, and tandem differential mobility analyzers are used to thoroughly characterize the PM emissions in terms of their size distributions, morphology, mass-mobility exponents, effective densities, volatility, mixing state, and primary particle size. This work analyzes these characteristics both in absolute terms and in relation to aggregate size. Knowledge of the particle volatility (f_N, f_m, and mixing state) is useful for choosing suitable exhaust aftertreatment (e.g., oxidation catalyst or particulate filters). Furthermore, an understanding of the mass-mobility relationship allows PM mass concentration to be calculated from size distribution measurements instead of filter methods that are time consuming and susceptible to measurement artifacts, especially at low particle concentrations (Liu et al. 2012). Moreover, knowledge of PM morphology can help distinguish any differences between natural-gas HPDI soot and diesel soot observed with light scattering or other optical techniques.

2.2 Experimental Setup

The experimental configuration is displayed in Figure 2.2. This work was conducted on a single-cylinder engine located in the University of British Columbia's Clean Energy Research Centre. The engine specifications are outlined in Table A1 in the appendices. The engine is a six-cylinder Cummins ISX engine modified so that only a single cylinder fires using an HPDI injector. Further information on the engine is reported by McTaggart-Cowan et al. (2007) and Patychuk (2013). This single-cylinder engine uses a prototype fueling system, and the operating conditions and results, while generally representative of non-premixed natural gas combustion, do not relate directly to any

previous, current, or future Westport engines. The testing was performed at six different operating conditions, which were based on the European Stationary Cycle (ESC-13; EU 1999). The ESC-13 modes are a common starting point when determining relevant operating conditions for heavy-duty engines (McTaggart-Cowan et al. 2012). Engine modes were selected at 25%, 37%, 50%, and 75% of maximum load at an engine speed of 1500 RPM (denoted B25, B37, B50, and B75 corresponding to 5.5, 8.25, 11, and 16.5 bar GIMEP). These modes operated with 20% EGR; however, at the highest load a 0% EGR mode was also examined.

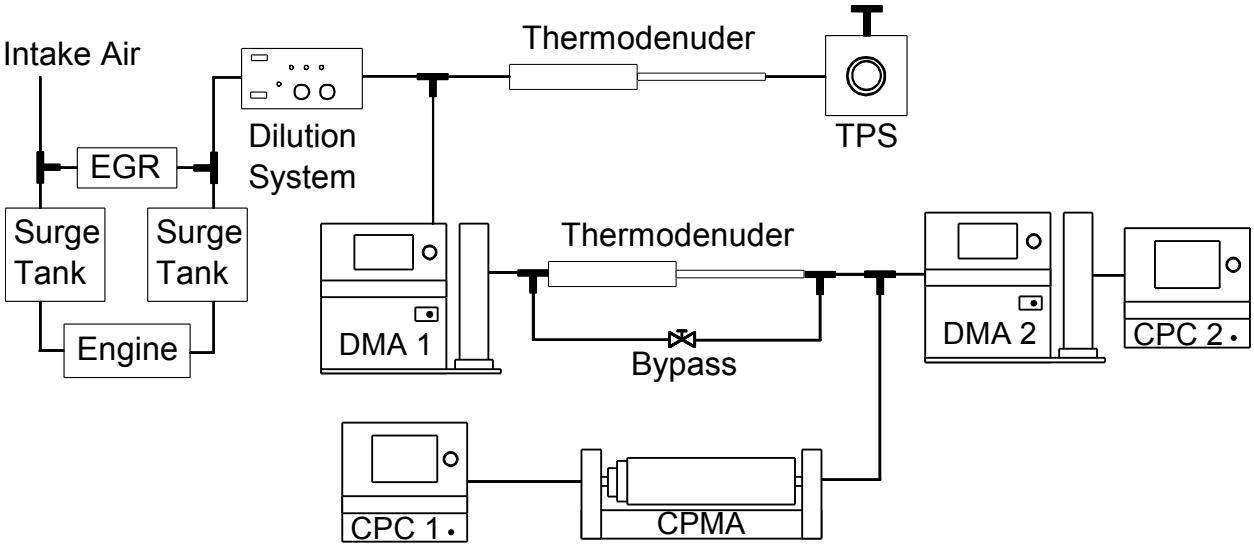

Figure 2.2: Experimental Setup.

A lower speed of 1200 RPM at 63% maximum load and 0% EGR (denoted A63) was also tested. At this mode, the majority (~80%) of the natural gas was injected into the combustion chamber during the intake stroke, allowing the bulk of the gas to premix before ignition. A diesel pilot was used near TDC to initiate the combustion event. This mode was selected as it provided relatively low total PM emission (on a mass basis) due to the premixed nature of the combustion. As such, it was hypothesized that the characteristics of the PM formed at this mode would be very different from that at other modes.

For PM sampling, the exhaust gas was first passed through a two-stage ejector dilutor system with an overall dilution ratio of approximately 11:1. This is done to lower

the partial pressure of water vapour and prevent it from condensing. Flow was then split into two streams, one of which fed a series of instruments to quantify the particles' mass-mobility relationship, volatility, and the mixing state of the volatile material. The particles first passed into a differential mobility analyzer (DMA1; Model 3081, TSI Inc., Shoreview, MN, USA), which classifies particles by mobility-equivalent diameter. It charges the particles then passes them into a gap between two concentric cylinders. As the particles move down the length of the cylinders, they are subjected to an electrostatic force caused by a potential difference between the cylinders. This force attracts the (oppositely) charged particles towards the inner cylinder, and the speed the particles move inward is dependent on their aerodynamic drag (electrical mobility). Particles with a certain electrical mobility move inward at a speed which causes them to pass through the sample outlet. The DMA was set at a constant voltage to admit a constant, narrow range of particles with the same electrical mobility. DMA1 was operated with a sheath flow of 6 L/min and aerosol flowrate of 0.6 L/min.

The aerosol flow then proceeded through either a thermodenuder or its bypass. A thermodenuder contains a section of heated tubing in which volatile material is evaporated. As the sample exits the heating section and begins to cool, the volatile material condenses on the tube walls rather than the particles due to the Kelvin effect (Hinds, 1999), and the remaining PM sample is comprised solely of non-volatile material. After exiting the thermodenuder, the flow was split again. Half of this flow was sent to a scanning mobility particle spectrometer (SMPS) system which consists of a DMA (DMA2) and a condensation particle counter (CPC, Model 3775, TSI Inc., Shoreview, MN, USA). An SMPS progressively steps though the DMA voltage range (classifying a range of mobility-equivalent diameters) and records the associated number concentrations with the CPC. This results in a particle number distribution as a function of mobility-equivalent diameter. The DMA had a sheath flow of 3 L/min and the CPC had an aerosol flow of 0.3 L/min. Because the particles had already been sent through the first DMA, the second DMA's charger was bypassed. The mobility-equivalent diameter was taken to be the geometric mean diameter (GMD) of a lognormal fit of the data. For an undenuded sample, a mean bias of 0.5% was observed

between the first DMA's mobility-equivalent diameter set point and the GMD reported by the second DMA. Total particle distributions were also measured by bypassing the first DMA and performing SMPS scans on the entire particle sample. Number concentrations for denuded scans were corrected for diffusional deposition losses through the thermodenuder using the formulation in Gormley and Kennedy (1949). The losses are a function of a single dimensionless parameter proportional to tube length, volumetric flowrate, and the particles' diffusion coefficient. Tube length was taken to be the additional length of tube in the denuder, compared to the flow path of the undenuded samples. Particles are also lost due to thermophoresis in the thermodenuder. Experimentally, it was determined that the thermophoretic losses were relatively small (~5–10%). A correction for thermophoretic losses was not applied to the data as it was found (in some cases) to overcompensate the losses (the corrected denuded number concentrations were higher than the undenuded samples).

The remaining half of the aerosol exiting the thermodenuder was sent to a CPMA, which classifies particles based on their mass-to-charge ratio (Olfert and Collings 2005). The charged particles are passed into a gap between two rotating concentric cylinders with a potential difference between them. The rotation produces a centrifugal force on the particles toward the outer cylinder, and the electrical potential attracts the particles to the inner cylinder. These opposing forces are balanced for particles with the correct mass-to-charge ratio, which pass straight through the classifier. The CPMA was stepped through various particle mass settings, by stepping both the rotation speed and voltage to ensure a constant resolution across the CPMA range. The resolution, defined as the inverse of the normalized full-width half-maximum of the transfer function, was approximately 10 (i.e., the resolution was approximately a tenth of the CPMA set point). Particle counts at these mass settings were measured using a CPC (Model 3025, TSI Inc., Shoreview, MN, USA). Under the assumptions that there are no multiply charged particles and that the effective density is approximately constant for a given mobility (reasonable for the narrow range of classified particles), the distribution function is normal and the peak is equivalent to the average particle mass classified by the CPMA. If multiply charged particles are present, they may be seen as a second concentration

peak, given that the CPMA and DMA resolutions are high enough. A least-squares minimization can be performed that fits the data with a lognormal distribution (or bi-modal lognormal distribution if multiple charged particles are present), as seen in Tajima et al. (2011). The second line from the diluter leads to the thermophoretic sampler (TPS), which deposits particles onto carbon grids (300 Mesh Cu) using thermophoretic deposition for TEM analysis. The samples were collected downstream of the upper thermodenuder in Figure 2.2 operating at 200°C to remove the semi-volatile material. On average, 40 images were produced for each test point using a Hitachi H7600 transmission electron microscope operating at 80 kV under high-resolution mode. Images were taken at the center and four other locations around the grid. Images considered in size characterization were collected at optimum optical focus with nominal resolution of 0.2 nm. Morphology parameters of soot particles were extracted from TEM images using a semi-automated image processing program written in MATLAB (see the supplemental information of Dastanpour and Rogak 2014).

2.3 Experimental Results

2.3.1 Size Distributions

The undenuded size distributions for all engine modes can be seen in Figure 2.3. A clear trend is observed whereby an increase in engine load produces a higher PM number concentration, as well as a larger GMD. Mode A63 80% Premixed was seen to have the broadest distribution, in addition to the lowest number concentration. Its GMD also followed the relationship with load: found between mode B50 20% EGR and the B75 modes.

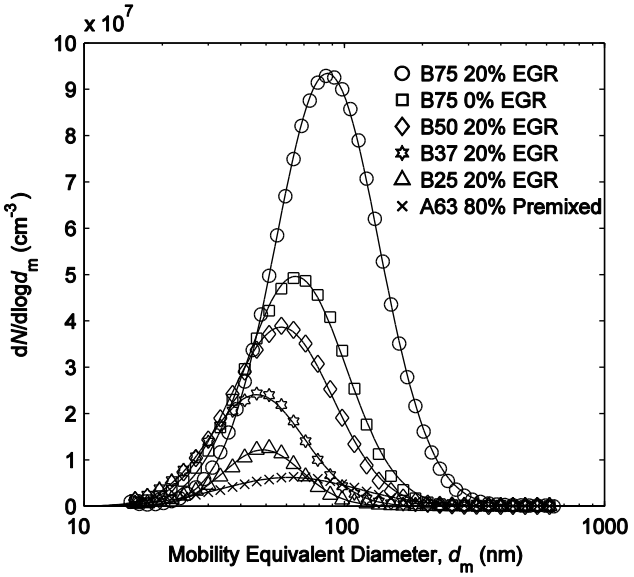

Figure 2.3: Undenuded SMPS size distributions, corrected by dilution ratio of 11:1.

2.3.2 Volatility and Mixing State

SMPS scans of denuded particles were also performed for each engine mode. Figure 2.4 highlights the comparison between denuded and undenuded scans for mode B25 20% EGR. The change in GMD is related to the amount of internal mixing between semi-volatile liquids and solid fractal-like carbonaceous particles. Internal mixing implies that both species are present on a single particle (a solid elemental carbon particle coated with liquid volatile material). As such, the particle diameter will decrease once it is denuded. Also, the reduction in total number concentration is indicative of externally mixed volatility—semi-volatile droplets are mixed separately from the soot particles (i.e., some semi-volatile droplets contain no soot). Denuding this type of mixed aerosol will eliminate all particles comprised solely of semi-volatile material.

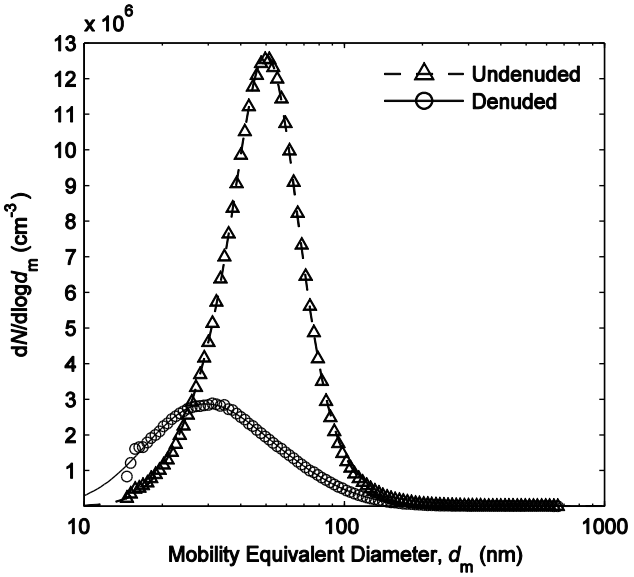

Figure 2.4: Denuded and undenuded particle number concentration for mode B25 20% EGR, corrected by dilution ratio of 11:1.

The amount of external mixing can be quantified using f_N. f_N of a particle distribution is equal to the number of purely volatile particles that are removed by denuding, divided by the total number of nascent particles (the total number concentration measured by the SMPS). The f_N for each engine mode is compared in Figure 2.5, along with the number of times each mode was reproduced. An increase in engine load results in a smaller f_N, whereas the decrease in EGR at condition B75 resulted in an increase in f_N. Finally, the lower-speed, fumigation-style mode A63 80% Premixed contained the lowest f_N of all.

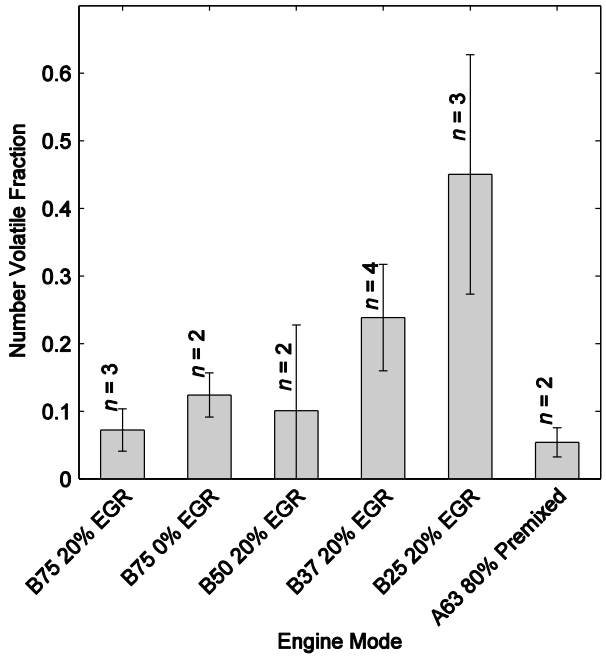

Figure 2.5: Number volatile fraction. Error bars represent one standard deviation.

In diesel-fueled compression-ignition engines, the externally mixed semi-volatile particles are generally thought to be contained in the nucleation mode—a mode of the size distribution generally below 50 nm in diameter and readily distinguished from the accumulation mode comprised of internally mixed soot particles of larger size (Kittelson 1998). In contrast, particles emitted from the HDPI engine contain significant numbers of externally mixed semi-volatile particles (Figure 2.5), yet the size distributions are all unimodal (Figure 2.3). Although these particles are generated by very different processes (e.g., nucleation vs. agglomeration of soot followed by condensational growth), these modes are not distinguishable in the undenuded size distribution. This is because when the number fraction of externally mixed particles is large, the size of the soot particles is relatively small (e.g., B25 20% EGR), and when the size of the soot particles is relatively large, the number fraction of externally mixed particles is relatively low (e.g., B75 20% EGR).

In addition to quantifying volatility on a number basis, more information on the PM mixing state can be gained from presenting the volatility on a mass basis. The f_m within a single particle (internally mixed volatility) is defined as the mass of volatile material

condensed on a particle (denuded mass subtracted from undenuded mass) divided by the total (undenuded) mass of the internally mixed particle. f_m as a function of particle size is plotted in Figure 2.6. Error bars represent one standard deviation, and included in the legend are the number of times each mode was reproduced. Almost all of the uncertainty in these results stem from the low reproducibility of the engine modes and the variability in volatility rather than inaccuracies in the instruments. The same engine conditions on a different day can yield different levels of volatility. This can be due to factors such as variation within the engine itself or the dilution system causing changes in particulate composition. The highly volatile modes are more susceptible to this variation.

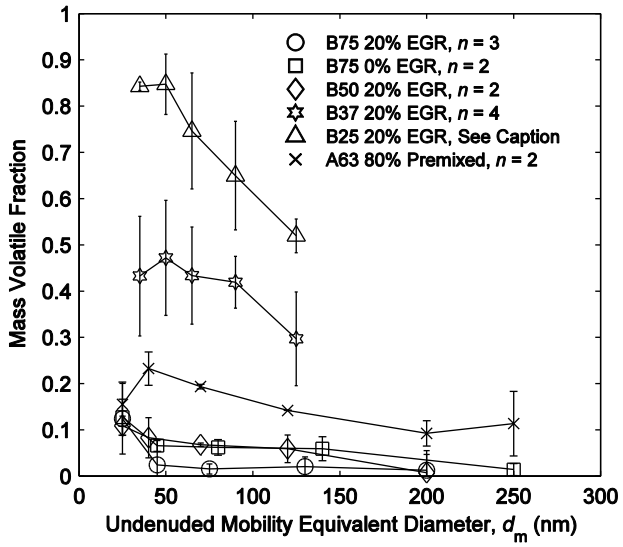

Figure 2.6: Mass volatile fraction of exhaust particles. Error bars represent one standard deviation. Mode B50 20% EGR at 250 nm was reproduced n = 3 times, and mode B25 20% EGR was reproduced n = 2 times at 50 nm, n = 3 times at 35 and 125 nm, and n = 4 times at 65 and 90 nm.

High-load modes such as B75 20% EGR, B75 0% EGR, and B50 20% EGR showed low amounts of internally mixed volatile matter. In comparison to mode B75 20% EGR, the 0% EGR case had an f_m that was several percentage points higher. As load decreased however, f_m increased, as with modes B37 20% EGR and B25 20% EGR. Volatile material may be partially derived from lubricating oil (which would produce approximately the same amount of volatile material independent of load), yet the f_m decrease may be due to the larger number concentration of aggregate particles at high

loads. The f_m of mode A63 80% Premixed was found to be between the high-load modes and B37 20% EGR, at around 20%. The decreasing trend in volatility as mobility-equivalent diameter increases has also been observed for diesel exhaust (Sakurai et al. 2003; Ristimäki et al. 2007), as well as McKenna and inverted burners (Ghazi et al. 2013).

2.3.3 Effective Density

The mass of a particle (m) is often found to scale with mobility-equivalent diameter (d_m) in a power-law relationship,

$$m = C {d_m}^{D_m}, \quad 2.1$$

where C is a prefactor, and D_m is the mass-mobility exponent. This formula can then be used to determine the effective density of the particles,

$$\rho_{eff} = \frac{m}{\frac{\pi}{6}{d_m}^3} = \frac{6}{\pi} C {d_m}^{D_m - 3} = k {d_m}^{D_m - 3}. \quad 2.2$$

Because aggregate particles typically incorporate more open space as they grow, their effective density tends to decrease as size increases. The prefactor k and exponent D_m are determined by fitting a power-law relation through several corresponding masses and mobility-equivalent sizes throughout the particle size distribution.

Effective density measurements for all engine modes, without denuding the particles, can be seen in Figure 2.7, with the prefactors and mass-mobility exponents listed in the legend. The B75 modes and mode B50 20% EGR possess similar trends, having mass-mobility exponents of about 2.4. Modes A63 80% Premixed and B37 20% EGR have larger mass-mobility exponents and effective densities. Mode B25 20% EGR has a mass-mobility exponent of approximately 3, meaning that the particles are spherical, and hence their effective density does not change with size. As discussed above, the externally mixed volatile modes B25 20% EGR and B37 20% EGR would normally be expected to show two concentration peaks in the CPMA scans; however, this was not observed. Therefore, the effective densities of the aggregate particles and the volatile droplets must be similar. The density of engine oil or similar hydrocarbon

liquid is usually between 800 and 1000 kg/m^3. If the aggregate effective density is close to this range, a single concentration peak should be observed despite the fact that two particle species are present.

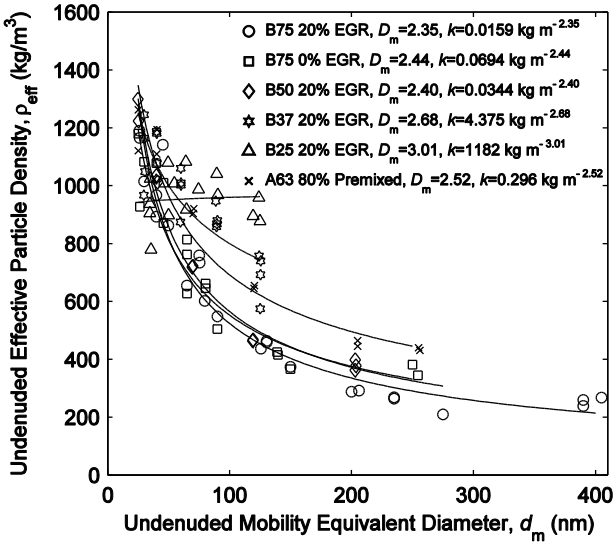

Figure 2.7: Effective density versus diameter for undenuded particles.

Denuded effective density data is plotted in Figure 2.8, with the prefactors and mass-mobility exponents shown in the legend. The majority of the data collapses to mass-mobility exponents of 2.4 to 2.6. Despite the different mass-mobility exponents, the denuded effective density data is still somewhat grouped, and so it may be convenient to represent all modes with a single relationship for mass concentration calculations via SMPS scans. This can also be seen in Figure 2.8. Data points are plotted using the denuded mobility-equivalent diameter measured with the second DMA, after volatile material was removed. The shaded region represents an uncertainty of ± 20% in effective density. The effective density data for diesel soot from Olfert et al. (2007), as well as that from Maricq and Xu (2004), are within the region of uncertainty of the combined trendline throughout the given size range; however, the effective densities determined by Park et al. (2003) were found to be higher for mobility equivalent sizes below 220 nm. In comparison to these previous diesel studies, the mass-mobility exponents determined here are similar or slightly higher. For reference, Park et al. (2003) found exponents of between 2.33 and 2.41, Maricq and Xu (2004) had exponents of 2.3 ± 0.1, and Olfert et al. (2007) had mass-mobility exponents of 2.22 to

2.48 when the volatility was low. It is interesting to note that although natural gas reduces the PM number and mass concentrations in relation to diesel, the morphology of the soot remains quite similar in terms of mass-mobility exponent.

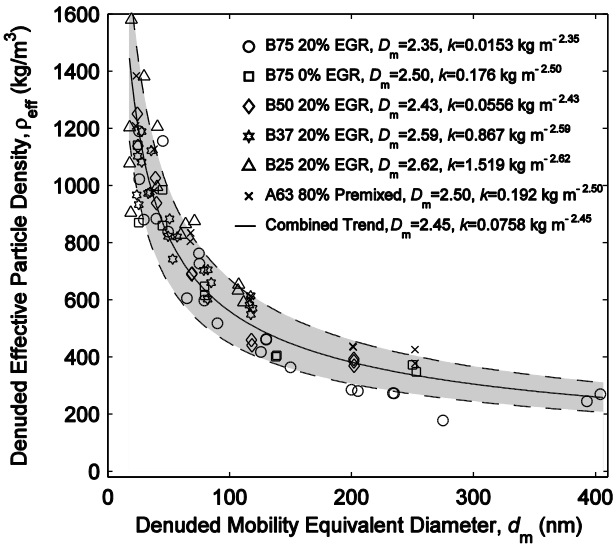

Figure 2.8: Combined trendline for denuded data.

A comparison of Figure 2.7 to Figure 2.8 elucidates that there was in fact some volatile material coating the particles that was subsequently evaporated inside the thermodenuder. This conclusion agrees well with the above-mentioned volatility results: low-load modes such as B25 20% EGR and B37 20% EGR contained the highest levels of volatile matter. The spherical particles observed at undenuded mode B25 20% EGR are likely coated with (or entirely comprised of) liquid material, and fittingly, the observed density is similar to that of engine oil or liquid hydrocarbon. The intermediate exponents of modes A63 80% Premixed and B37 20% EGR likely also result from the presence of volatile material; however, in these cases, the amount present is not sufficient to form a sphere around the soot structure, as with B25 20% EGR.

2.3.4 Morphology, Mass-Mobility Exponent, and Primary Particle Diameter

Sample TEM images of the test points are shown in Figure 2.9. Image processing results are also summarized in Table A2. TEM images demonstrated the collapse (or restructuring) of some soot aggregates at the high-volatility engine mode (mode B25 20% EGR). The restructuring of soot into more compact clusters when volatile material

is condensed on them is reported in the literature (Slowik et al. 2007). This is also consistent with Figure 2.8, which shows the effective densities of denuded B25 20% EGR particles tend to be higher (especially at higher mobility diameters) than the densities from other engine modes. The slightly elevated effective densities seen in Modes B37 20% EGR and A63 80% Premixed suggest that this effect may be present there as well. The degree to which the aggregate is restructured is dependent on the amount of volatile material coating the particle, as shown by Ghazi and Olfert (2013). This effect is noticeable for the more volatile engine modes with elevated internally mixed f_m because the amount of material coating the particle is sufficient to cause the soot to collapse. Note that the DMA-CPMA system will show this collapse in particle structure for a given mode even if the majority of particles (but not all) have collapsed, because their measurements are number-based. Alternatively, effective density has also been shown to scale with primary particle diameter (see below).

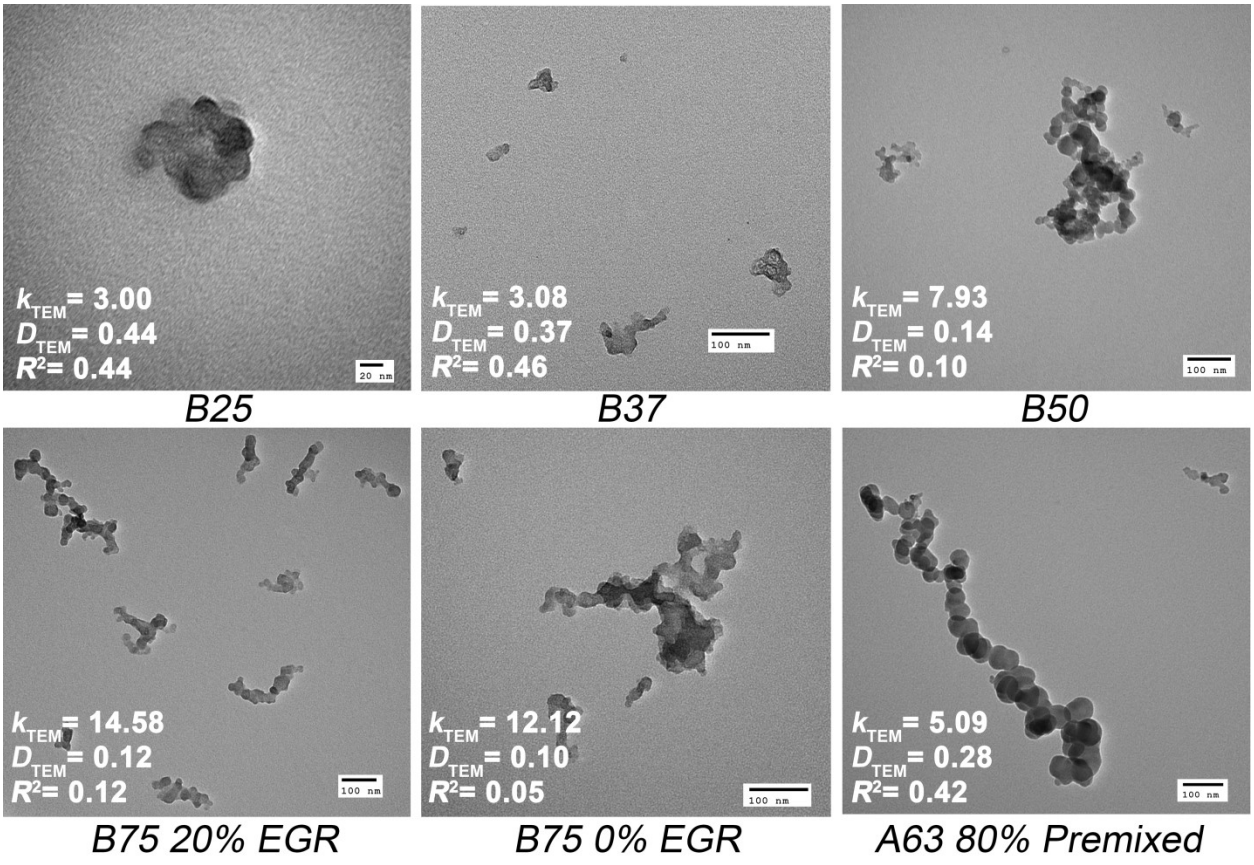

Figure 2.9: Sample TEM images. All scale bars are 100 nm, except for B25, which is 20 nm.

TEM results show that the primary particle diameter (d_p) first reduces when load increases from low to medium and then increases again from medium to high load conditions. For all operating conditions, the standard deviations of the primary particle size distributions are approximately 35% of the average primary particle diameter. Primary particle diameter is affected by different parameters including local EQR, temperature, and residence time of the particles in the combustion region (Glassman 1989; Park et al. 2005). The reduction observed in primary particle diameter when load increased from low to high levels may attribute to faster carbonization and higher oxidation rates due to higher temperature. Further increases in load result in higher EQRs in the combustion chamber. This may ultimately shift the balance between formation and oxidation rates and result in the formation of larger primary particles.

TEM results also show that the EGR results in an increase in primary particle diameter from 18.6 nm at 0% EGR to 25.7 nm at 20% EGR. This contrasts with previous findings by Patychuk (2013) where EGR had no effect on primary particle diameter. However, this agrees with the presence of a correlation between aggregate and primary particle diameters (Dastanpour and Rogak, 2014).

Primary particle diameter highly depends on engine operating condition. The average diameter of the primary particles varies between 13 nm and 26 nm in this study. Changing the engine operating conditions, Patychuk (2013) has measured primary particle diameter in the range of 23 to 33 nm for the same engine. The range of primary particle diameters measured on the HPDI engine (13–33 nm) is similar to the measurements of primary particle diameter in diesel engines (Lee et al. 2002; Wentzel et al. 2003; Park et al. 2004; Zhu et al. 2005; Neer and Koylu, 2006). Combining results obtained in this study with those reported by Mabson (2015) for the same engine, mean gyration radius of soot aggregates varies between 25 nm and 87 nm for the HPDI engine considered here. This is considerably smaller than the results reported for diesel engines, 75–180 nm (Lee et al. 2002; Zhu et al. 2005; Neer and Koylu, 2006). Previous studies conducted on the same HPDI engine (Soewono 2008; Mabson 2015) showed the fractal dimension and prefactor of the soot particles to be in the range of 1.4 to 1.8

and 1.43 to 2.53, respectively. Measured fractal dimensions and prefactors are approximately consistent with the range of 1.46 to 1.88, and 1.3 to 4.0 reported for diesel engines, respectively (Lee et al. 2002; Wentzel et al. 2003; Park et al. 2004; Zhu et al. 2005; Neer and Koylu, 2006). However, a precise comparison of the fractal prefactors is difficult because of differences in the methods used.

Dastanpour and Rogak (2014) have discussed the presence of a correlation between primary particle size and aggregate size. This correlation can be explained if soot aggregates are formed in homogenous microscopic regions, and aggregates with different formation and growth patterns are mixed. Their database comprised of four different soot sources including 14 different operating conditions of the HPDI engine considered in this study. They reported a correlation for the primary particle diameter as a function of projected area equivalent diameter of aggregates in the form of $d_{\mathrm{p}} = k_{\mathrm{TEM}}\, d_{\mathrm{a}}^{D_{\mathrm{TEM}}}$, where k_{TEM} = 6.49 (5.46, 7.52), D_{TEM} = 0.29 (0.26, 0.32), and R^2 = 0.327 (values in parenthesis are 95% confidence intervals) for the HPDI engine considered here. The fit parameters (k_{TEM}, D_{TEM}, R^2) obtained for the individual operating conditions considered in this study are shown inset to Figure 2.9 (details on the TEM analysis are given in Table A2 in the appendices). As shown in the figure, decreasing load or speed results in stronger correlations (larger D_{TEM}) between the primary particle and aggregate sizes. This trend might be an indication of more (relatively) heterogeneous charge distribution and lower mixing rates of the soot particles at lower engine loads and speeds, respectively.

2.4 Conclusion

The characteristics of the particulate emitted from a single-cylinder, compression-ignition, natural-gas research engine fitted with an HPDI system were studied in terms of their size distributions, morphology, mass-mobility exponents, effective densities, volatility, mixing state, and primary particle diameter. Number concentration and GMD were seen to increase with engine load. The f_{N} decreased as load increased, although mode A63 80% Premixed had the lowest f_{N} (but is a very different combustion regime).

f_m also decreased with load, and A63 80% Premixed had an f_m between that of B37 20% EGR and the higher-load modes. It is speculated that a roughly constant amount of volatile material is produced at each engine mode, and the decrease in f_m is due to the increase in PM number with load. The f_m was also seen to decrease as mobility-equivalent diameter increased.

The effective density and mass-mobility exponent results also indicate that more volatile material is present for the low load modes, especially for mode B25 20% EGR where the undenuded particles are spherical and are likely entirely coated with volatile liquid. Denuded effective density trends were observed to collapse to within approximately ±20% of a line of best fit. This single effective density function could be used to calculate particle mass concentrations for denuded PM using particle number distributions (Liu et al. 2012). However, the effective densities of undenuded soot were highly variable with respect to load due to the presence of relatively high amounts of volatile material at low load. Therefore, load-dependent effective density functions would be needed to calculate mass concentrations for undenuded particulate.

Although denuded effective densities were relatively similar with respect to load, it was observed the effective densities of modes with high levels of volatility were slightly higher, which suggests the soot structures collapsed into slightly more compact shapes. This was supported by TEM images of mode B25 20% EGR. TEM results also revealed that primary particle size reduces when load increases from low to medium and then increases again from medium to high load. This non-monotonic trend may be due to competing effects from the higher temperatures achieved from the initial load increase, and the higher EQRs seen at even higher loads. An increase in EGR was also seen to increase primary particle size.

Finally, coefficients were determined for a relation that gives primary particle diameter as a function of projected area equivalent diameter. A decrease in load or speed results in a stronger correlation.

These results can be useful in determining which type of after-treatment will be most effective at mitigating PM emissions. Results show that the PM consists of non-volatile soot aggregates either internally or externally mixed with semi-volatile material. Soot aggregates have similar primary particle size, aggregate size, and effective density as diesel soot, suggesting diesel particulate filters would be an effective means of reducing their emission.

2.4.1 Acknowledgements

We thankfully acknowledge the technical support and expertise provided by Westport Innovations Inc.

2.4.2 Funding

Funding for this project was provided by the Natural Science and Engineering Research Council of Canada ENGAGE grant program.

2.4.3 Supplemental Material

Supplemental material for this chapter can be seen in Appendix A.

2.4.4 References

Barone, T. L., Lall, A. A., Storey, J. M. E., Mulholland, G. W., Prikhodko, V. Y., Frankland, J. H., Parks, J. E., and Zachariah, M. R. (2011). Size-Resolved Density Measurements of Particle Emissions from an Advanced Combustion Diesel Engine: Effect of Aggregate Morphology. *Energy and Fuels*. 25(5):1978–1988.

Brasil, A. M., Farias, T. L., and Carvalho, M. G. (1999). A Recipe for Image Characterization of Fractal-Like Aggregates. *Journal of Aerosol Science*. 30(10): 1379–1389.

Bullock, D. S., and Olfert, J. S. (2014). Size, Volatility, and Effective Density of Particulate Emissions from a Homogeneous Charge Compression Ignition Engine Using Compressed Natural Gas. *Journal of Aerosol Science*. 75: 1–8.

Dastanpour, R., and Rogak, S. N. (2014). Observations of a Correlation between Primary Particle and Aggregate Size for Soot Particles. *Aerosol Science and Technology*. 48(10): 1043–1049.

Durdina, L., Brem, B. T., Abegglen, M., Lobo, P., Rindlisbacher, T., Thomson, K. A., Smallwood, G. J., Hagen, D. E., and Wang, J. (2014). Determination of PM Mass Emissions from an Aircraft Turbine Engine Using Particle Effective Density. *Atmospheric Environment*. 99: 500–507.

European Union (EU). Directive 1999/96/EC of the European Parliament and of the Council. December, 1999.

Faghani, E., Patychuk, B. D., McTaggart-Cowan, G. P., and Rogak, S. N. (2013). Soot Emission Reduction from Post Injection Strategies in a High Pressure Direct-Injection Natural Gas Engine. *SAE International*. Doi: 10.4271/2013-24-0114.

Fujita, E., Zielinska, B., Campbell, D., Arnott, P., Sagebiel, J., Mazzoleni, L., Chow, J., Gabele, P., Crews, W., Snow, R., Clark, N., Wayne, S., and Lawson, D. (1995) Variations in Speciated Emissions from Spark-Ignition and Compression-Ignition Motor Vehicles in California's South Coast Air Basin. *Journal of the Air and Waste Management Association*. 57(6): 705–720.

Ghazi, R., and Olfert, J. S. (2013). Coating Mass Dependence of Soot Aggregate Restructuring Due to Coatings of Oleic Acid and Dioctyl Sebacate. *Aerosol Science and Technology*. 47(2):192–200.

Ghazi, R., Tjong, H., Soewono, A., Rogak, S. N., and Olfert, J. S. (2013). Mass, Mobility, Volatility, and Morphology of Soot Particles Generated by a McKenna and Inverted Burner. *Aerosol Science and Technology.* 47(4):395–405.

Glassman, I. (1989). Soot Formation in Combustion Processes. *Symposium (International) on Combustion.* 22(1): 295–311.

Gormley, P. G., and Kennedy, M. (1949). Diffusion from a Stream Flowing Through a Cylindrical Tube. *Proceedings of the Royal Irish Academy*. 52A: 163–169.

Hinds, W. (1999) Aerosol Technology: Properties, Behavior, and Measurement of Airborne Particles, 2nd Edition. John Wiley and Sons. Hoboken, NJ.

Johnson, T. (2012). Vehicular Emissions in Review. *SAE International Journal of Engines*. 5: 216–234.

Johnson, T., Olfert, J. S., Symonds, J., Johnson, M., Rindlisbacher, T., Swanson, J. J., Boies, A. M., Thomson, K., Smallwood, G., Walters, D., Sevcenco, Y., Crayford, A., Durdina, L., Bahk, Y. K., Brem, B., and Wang, J. (2015). Effective Density and Mass-Mobility Exponent of Aircraft Turbine Particulate Matter. *Journal of Propulsion and Power*. 31(2): 573–582.

Jones, H. L. (2004). Source and Characterization of Particulate Matter from a Pilot-Ignited Natural Gas Fuelled Engine. M.Sc. thesis. University of British Columbia, Vancouver, Canada.

Kittelson, D. B. (1998). Engines and Nanoparticles: A Review. *Journal of Aerosol Science*. 29:575–588.

Lee, K. O., Cole, R., Sekar, R., Choi, M. Y., Kang, J. S., Bae, C. S., and Shin, H. D. (2002). Morphological Investigation of the Microstructure, Dimensions, and Fractal

Geometry of Diesel Particulates. *Proceedings of the Combustion Institute*. 29(1): 647–653.

Liu, Z., Swanson, J., Kittleson, D., and Pui, D. (2012). Comparison of Methods for Online Measurement of Diesel Particulate Matter. *Environmental Science and Technology*. 46(11): 6127–6133.

Mabson, C. (2015). Emissions Characterization of Paired Gaseous Jets in a Pilot-Ignited Natural-Gas Compression-Ignition Engine. M.Sc. thesis. University of British Columbia, Vancouver, Canada.

Maricq, M., and Xu, N. (2004). The Effective Density and Fractal Dimension of Soot Particles from Premixed Flames and Motor Vehicle Exhaust. *Journal of Aerosol Science*. 35: 1251–1274.

McTaggart-Cowan, G. P., Jones, H. L., Rogak, S. N., Bushe, W. K., Hill, P. G., and Munshi, S. R. (2007). The Effects of High-Pressure Injection on a Compression-Ignition, Direct Injection of Natural Gas Engine. *ASME Journal for Engineering Gas Turbines and Power*. 129: 579–588.

McTaggart-Cowan, G. P., Mann, K., Huang, J., Wu, N., and Munshi, S. R. (2012). Particulate Matter Reduction from a Pilot-Ignited, Direct Injection of Natural Gas Engine. *Proceedings of the ASME Internal Combustion Engine Division Fall Technical Conference*. September 23–26, Vancouver, Canada, pp. 427–437.

Medalia, A. I., and Heckman, F. A. (1969). Morphology of Aggregates—II. Size and Shape Factors of Carbon Black Aggregates from Electron Microscopy. *Carbon*, 7(5): 567–582.

Mustafi, N. N., Raine, R. R., and James, B. (2010). Characterization of Exhaust Particulates from a Dual Fuel Engine by TGA, XPS, and Raman Techniques. *Aerosol Science and Technology.* 44(11): 954–963.

Neer, A., and Koylu, U. O. (2006). Effect of Operating Conditions on the Size, Morphology, and Concentration of Submicrometer Particulates Emitted from a Diesel Engine. *Combustion and Flame*. 146(1–2): 142–154.

Olfert, J. S., and Collings, N. (2005). New Method for Particle Classification—The Couette Centrifugal Particle Mass Analyzer. *Journal of Aerosol Science*. 36(11): 1338–1352.

Olfert, J. S., Symonds, J., and Collings, N. (2007). The Effective Density and Fractal Dimension of Particles Emitted from a Light-Duty Diesel Vehicle with a Diesel Oxidation Catalyst. *Journal of Aerosol Science.* 38: 69–82.

Park, K., Cao, F., Kittelson, D., and McMurry, P. (2003). Relationship between Particle Mass and Mobility for Diesel Exhaust Particles. *Environmental Science and Technology*. 37(3): 577–583.

Park, K., Kittelson, D. B., and McMurry, P. H. (2004). Structural Properties of Diesel Exhaust Particles Measured by Transmission Electron Microscopy (TEM): Relationships to Particle Mass and Mobility. *Aerosol Science and Technology*. 38(9): 881–889.

Park, S. H., Rogak, S. N., Bushe, W. K., Wen, J. Z., and Thomson, M. J. (2005). An Aerosol Model to Predict Size and Structure of Soot Particles. *Combustion Theory and Modelling*. 9(3): 499–513.

Patychuk, B. D. (2013). Particulate Matter Emission Characterization from a Natural Gas High-Pressure Direct-Injection Engine. M.Sc. thesis. University of British Columbia, Vancouver, Canada.

Patychuk, B. D., and Rogak, S. N. (2012). Particulate Matter Emission Characterization from a Natural Gas Fuelled High Pressure Direct Injection Engine. *Proceedings of the ASME Internal Combustion Engine Division Fall Technical Conference*. September 23–26, Vancouver, Canada, pp. 447–455.

Ristimäki, J., Vaaraslahti, K., Lappi, M., and Keskinen, J. (2007). Hydrocarbon Condensation in Heavy-Duty Diesel Exhaust. *Environmental Science and Technology*. 41: 6397–6402.

Rogak, S. N., Flagan, R. C., and Nguyen, H. V. (1993). The Mobility and Structure of Aerosol Agglomerates. *Aerosol Science and Technology*. 18(1): 25–47.

Sakurai, H., Park, K., McMurry, P. H., Zarling, D. D., Kittleson, D. B., and Ziemann, P. J. (2003). Size-Dependent Mixing Characteristics of Volatile and Nonvolatile Components in Diesel Exhaust Aerosols. *Environmental Science and Technology.* 37:5487–5495.

Seong, H., Choi, S., and Lee, K. (2014). Examination of Nanoparticles from Gasoline Direct-Injection (GDI) Engines Using Transmission Electron Microscopy (TEM). *International Journal of Automotive Technology*. 15(2): 175–181.

Slowik, J. G., Cross, E. S., Han, J. H., Kolucki, J., Davidovits, P., Williams, L. R., Onasch, T. B., Jayne, J. T., Kolb, C. E., and Worsnop, D. R. (2007). Measurements of Morphology Changes of Fractal Soot Particles Using Coating and Denuding Experiments: Implications for Optical Absorption and Atmospheric Lifetime. *Aerosol Science and Technology*. 41(8): 734–750.

Soewono, A. (2008). Morphology and Microsctructure of Diesel Particulates. M.Sc. thesis. University of British Columbia, Vancouver, Canada.

Tajima, N., Fukushima, N., Ehara, K., and Sakurai, H. (2011). Mass Range and Optimized Operation of the Aerosol Particle Mass Analyzer. *Aerosol Science and Technology*. 45(2): 196–214.

Tian, K., Liu, F., Yang, M., Thomson, K. A., Snelling, D. R., and Smallwood, G. J. (2007). Numerical Simulation Aided Relative Optical Density Analysis of TEM Images for Soot Morphology Determination. *Proceedings of the Combustion Institute*. 31(1): 861–868.

Wentzel, M., Gorzawski, H., Naumann, K.-H., Saathoff, H., and Weinbruch, S. (2003). Transmission Electron Microscopical and Aerosol Dynamical Characterization of Soot Aerosols. *Journal of Aerosol Science*. 34(10): 1347–1370.

Westport Innovations Inc. First Generation Westport HPDI Technology. http://www.westport.com/is/core-technologies/combustion/hpdi. Accessed July 30, 2015.

Wong, W., Midkiff, K., and Bell, S. (1991). Performance and Emissions of Natural Gas Dual-Fueled, Direct Injected Diesel Engine. *SAE International.* Doi: 10.4271/911766.

Zhu, J., Lee, K. O., Yozgatligil, A., and Choi, M. Y. (2005). Effects of Engine Operating Conditions on Morphology, Microstructure, and Fractal Geometry of Light-Duty Diesel Engine Particulates. *Proceedings of the Combustion Institute*. 30(2): 2781–2789.

3. Morphology and Volatility of Particulate Matter Emitted from a Gasoline Direct Injection Engine Fueled on Gasoline and Ethanol Blends

3.1 Introduction

The introduction of direct fuel injection to gasoline engines has led to an increase in fuel efficiency and engine performance in relation to traditional port injection. This is because direct injection allows for control of fuel injection timing, and because the liquid droplets sprayed into the cylinder cool the surrounding air as they evaporate, allowing more air into the cylinder. Unfortunately, these liquid fuel droplets also have less time to evaporate and mix with the incoming air, so particulate emissions of direct injection engines tend to be higher than those from port injection engines (Su et al., 2013; Liang et al., 2013; Karavalakis et al., 2014a; Bielaczyc et al., 2014).

The addition of ethanol to gasoline has advantages which include increased knock resistance as well as potential greenhouse gas benefits because ethanol is produced from renewable sources (U.S. Department of Energy, 2015). Moreover, there is evidence that ethanol reduces PM emissions (Fatouraie et al., 2013; Storey et al., 2014; and Zhang et al., 2014). A maximum fraction of 10% ethanol is allowed by the EPA to be blended with gasoline for use in all cars and light trucks, although the EPA has approved the use of 15% ethanol in vehicles of model year 2001 and newer (EIA, 2012). Ethanol consumption in the US is proposed to be 13.71 billion gallons in 2015 and 13.83 billion gallons in 2016 (up from 13.47 billion gallons in 2014 and 12.86 billion gallons in 2010) (EIA, 2015a; EIA, 2015b). One challenge facing the introduction of higher-percentage ethanol mixtures is its compatibility with materials used within engines. Vehicles compatible with ethanol will need to be commonplace if its content in gasoline is to increase significantly (EIA, 2012).

The addition of ethanol to gasoline produces some competing effects regarding the production of particulate matter. The oxygen contained in ethanol molecules is thought to help oxidize particles and ultimately reduce PM emissions (Chen et al., 2012).

Moreover, aromatic molecules have been linked to PM production (Vuk and Vander Griend, 2013; Chen et al., 2015) and the addition of ethanol leads to a fuel mixture with a smaller aromatic fraction than pure gasoline. Ethanol has been found to decrease particulate number and mass concentrations by Storey et al. (2010), Storey et al. (2012), Catapano et al. (2013), Vuk and Vander Griend (2013), Fatouraie et al. (2013), Storey et al. (2014), and Zhang et al. (2014). Despite this, there is also conflicting evidence that ethanol can increase particulate production in some instances (Chen et al., 2010; Chen et al., 2012; Catapano et al., 2013). This is suspected to be due to the higher heat of vaporization of ethanol in relation to gasoline, meaning that fuel droplets take longer to evaporate and the air-fuel mixture becomes less well mixed, leading to zones of fuel-rich combustion (Chen et al., 2012). Similar effects from the aromatic content and volatility of the gasoline itself have been observed by Khalek et al., (2010), Kim et al. (2013), and Storey et al. (2014). Other alcohols have also been investigated such as butanol, which decreased PM when mixed with gasoline (Gu et al., 2012; Zhang et al., 2014; Karavalakis et al., 2014a); although it also decreases the fuel's knock resistance. Liang et al. (2013) investigated blends of gasoline mixed with methanol and found that methanol also helps reduce PM emissions.

The solid portion of particulate matter (PM) generated by gasoline direct injection (GDI) engines is largely comprised of elemental carbon formed into small primary particles which agglomerate to form fractal-like aggregates. Primary particle size has been shown to increase with aggregate size (Lee et al., 2013; Dastanpour and Rogak, 2014; Seong et al., 2014), and ranges from < 5 nm (Sgro et al., 2012) to 55 nm (Kameya and Lee, 2013). The shape of an aggregate particle can be quantified using the mass-mobility exponent, which describes the scaling of particle mass (m) with mobility-equivalent diameter (d_{m}) as seen in equation 1.1, where C is a prefactor, and D_{m} is the mass-mobility exponent. The mass-mobility exponent can be used to estimate primary particle size with aggregates (Dastanpour et al., 2015). In the case of GDI soot, Symonds et al. (2008) determined the mass-mobility exponent to be 2.65 and Momenimovahed and Olfert (2015) calculated exponents between 2.5 and 2.7 for non-volatile particles. These exponents are higher than those for diesel soot (2.33 - 2.41 for

Park et al. (2003), 2.3 ± 0.1 for Maricq et al. (2004), and 2.22 - 2.48 for Olfert et al. (2007) when the volatility was low). Barone et al. (2012), Lee et al. (2013), and Kameya and Lee (2013) have noted similarities of GDI particulate to diesel particulate regarding particle shape and internal structure. To date, a study has not been conducted on the effects of ethanol on mass-mobility exponent for GDI engines.

In addition to solid carbon, particulate may also exist in the liquid phase. Droplets can be formed from impinged fuel or oil on a surface within the cylinder (Barone et al., 2012) or from condensed hydrocarbons in the exhaust (Sgro et al., 2012; Lee et al., 2013). Liquids can form separate droplets or they can condense on the solid soot aggregates. In the latter case, the proportion of volatile material to solid elemental carbon within a given particle is dependent on particle size. Sakurai et al. (2003) and Ristimäki et al. (2007) found that the relative amount of volatile material on a particle decreases with an increase in particle size on a volume basis and a mass basis for diesel engines. Ghazi et al. (2013) observed the same trend for particulate generated from McKenna and inverted burners, as did Graves et al. (2015) for a direct-injected natural gas compression ignition engine while at low loads. Momenimovahed and Olfert (2015) also noticed this effect on GDI engines at conditions where volatility was substantial (above approximately 20%). Depending on engine power, they observed mass-based volatility between 10% and 30%. Research has not yet been done to investigate the effects of ethanol in GDI engines on particle volatility.

In this study, tandem differential mobility analyzers (DMA) were used in conjunction with a centrifugal particle mass analyzer (CPMA) to determine the effect of ethanol on GDI particulate emissions in terms of their particle structure (size, mass-mobility exponent, and effective density) and volatility (or mixing state). Knowledge of PM structure and volatility will allow recommendations to be made regarding aftertreatment strategies (e.g. gasoline particulate filter (GPF), catalytic converter). Furthermore, the effective density allows the PM mass concentration to be determined using size distributions instead of time consuming filter methods which are susceptible to measurement artifacts (Liu et al., 2012).

3.2 Experimental Setup

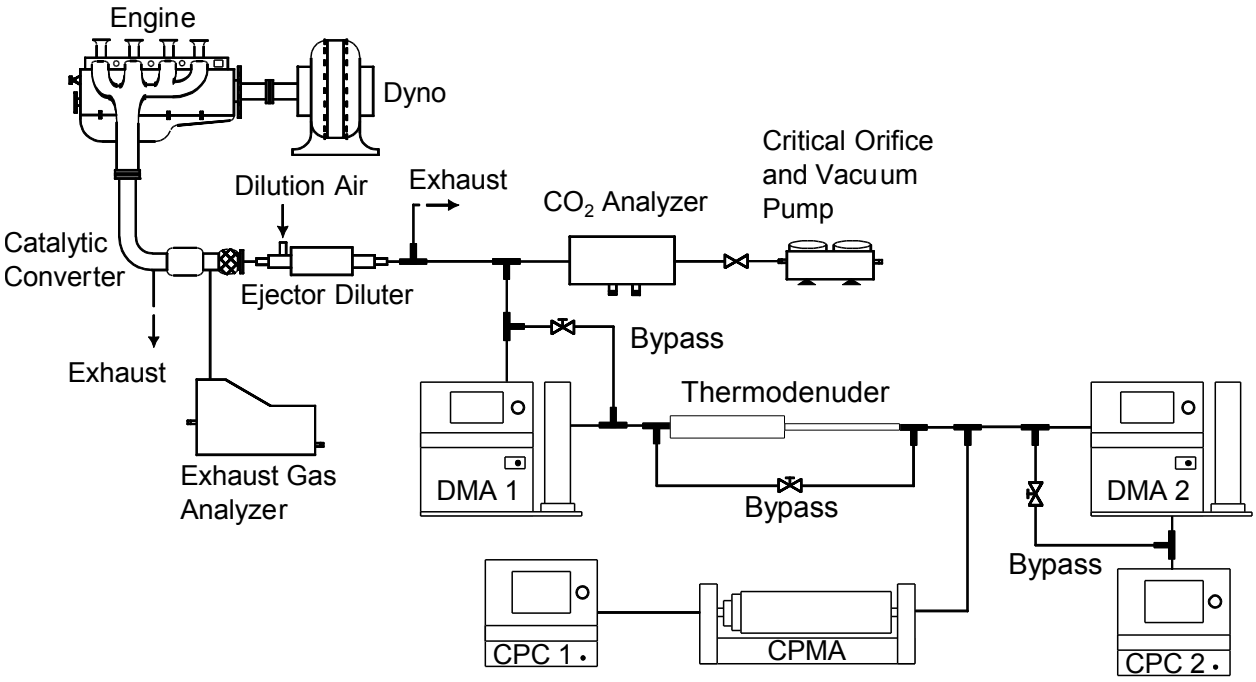

Figure 3.1: Experimental Setup.

The experimental setup is pictured in Figure 3.1. Measurements were taken from PM emissions emitted by a General Motors 2.0 litre, 4-cylinder, turbocharged, wall-guided GDI engine fitted with the production three-way catalytic converter and fueled with gasoline mixed with 0% (E0), 10% (E10), and 50% (E50) ethanol by volume. Commercially available, ethanol-free gasoline was used as the base fuel. The gasoline was analyzed and the results of the analysis are shown in Table 3.1. As expected the gasoline did not contain any oxygenates (i.e. ethanol). The most prominent constituents within the gasoline are aromatics and isoparaffins, the former is often associated with PM production. Also notable are the boiling points: the gasoline contains components which boil at both higher and lower temperatures than that of the ethanol. Ethanol does have a higher heat of vaporization however; so its charge cooling effect will be greater, and this may subsequently affect the fuel's ability to evaporate.

Table 3.1: Properties of gasoline and ethanol.

Property	**Gasoline (Shell 91 Octane)**	**Ethanol**
Formula	C3 – C12	C_2H_5OH
Density (kg/m^3)	785	790*
Boiling Point, 10% (°C)	38.1	78*
Boiling Point, 50% (°C)	102.2	
Boiling Point, 90% (°C)	159.2	
Anti-knock index **	91	100*
Aromatic Content (Volume %)	44.3	0.0
Isoparaffin Content (Volume %)	34.6	0.0
Napthene Content (Volume %)	4.8	0.0
Olefin Content (Volume %)	0.7	0.0
Paraffin Content (Volume %)	15.1	0.0
Oxygenate Content (Volume %)	0.0	100.0
Unidentified (Volume %)	0.4	0.0

*Catapano et al., 2013

**Anti-knock index (AKI) is equal to the mean of the research octane number (RON) and motor octane number (MON)

The engine was fitted to a 250 horsepower eddy current dynamometer (Dyne Systems Inc., Model MW1014W) and operated at four steady-state loads. The engine loads tested were chosen to match engine loads that are frequently encountered during the New European Driving Cycle (NEDC) (UNECE, 2013). The most common loads were approximately 15 N m and 45 N m and were chosen as test points alongside the idle condition (800 RPM). Another load of 90 N m was chosen since it is approximately the load encountered during acceleration in the NEDC. All three loads were operated at a speed of 2250 RPM. In relation to the engine's maximum torque output at 2250 RPM of 350 N m, these loads represent 4%, 13%, and 26% of the maximum achievable load. Fuel injection during idle was at the beginning of the intake stroke (350° before top dead

centre), and approximately the middle of the intake stroke while at 2250 RPM (280° before top dead centre).

Before taking measurements on a given day, the engine ran for approximately half an hour until parameters such as oil and catalyst temperatures became steady. In cases were multiple engine loads were tested without shutting the engine off, the engine was allowed to run for approximately fifteen minutes so the emissions could stabilize once again. After changing fuels, the engine was operated for at least an hour before any data was collected. Three replicate measurements were taken for each load and fuel, with the exception of size-segregated number concentrations, which were measured on one occasion but with five or six repeat measurements per size.

PM sampling was done by first passing the exhaust sample through a Dekati DI-1000 ejector diluter. A sensitivity study was conducted on the effects of heated dilution using a scanning mobility particle spectrometer (SMPS) and thermodenuder. No observable difference in the size distributions or the amount of volatile material was found for all four engine conditions. Unheated dilution was used subsequently. The dilution ratio (β) was calculated using measurements of upstream and downstream CO_2 concentration (measured by a Vetronix PXA-1100 exhaust gas analyzer and LI COR LI-840A CO_2 analyzer, respectively) and is

$$\beta = \frac{\varphi_1 - \varphi_{\mathrm{da}}}{\varphi_2 - \varphi_{\mathrm{da}}}. \qquad 3.1$$

φ_1 is the upstream concentration of CO_2, φ_2 is the downstream CO_2 concentration, and φ_{da} is the CO_2 concentration in the dilution air (Giechaskiel et al. 2009). The dilution ratio, which was calculated specifically for each PM measurement, was roughly 13:1.

After dilution, the flow passed into DMA1 (TSI Inc., Model 3081) which was maintained at a constant voltage to classify particles with a narrow range of electrical mobility. The shealth flow and aerosol flow rates of DMA1 were 18 L/min and 1.8 L/min, respectively. The aerosol sample was then sent to a thermodenuder (heated to 300°C) or its bypass (heating section 0.665 m long, 9.50 mm inner diameter; cooling section

1.435 m long, 2.75 mm inner diameter; 0.8 second residence time in heating section for 1.8 L/min aerosol flow rate), at which point the flow was split. 1.5 L/min of the flow was sent to a CPMA, which classifies an aerosol based on its mass to charge ratio (Olfert and Collings, 2005). The CPMA was stepped through various particle mass settings, by changing voltage and rotation speed. This results in a resolution which does not vary with particle mass. The CPMA resolution is defined as the inverse of the normalized full-width half-maximum of the transfer function, and was approximately 10 (i.e. the resolution was approximately a tenth of the CPMA set point) where possible, but at particle sizes of 30 nm and 45 nm it was set to 5 because the rotational speed would have otherwise exceeded the classifier's limitations. Particle counts were measured using a condensation particle counter (CPC; TSI Inc. Model 3776). The mass distribution function is approximately normal and its peak corresponds to the average classified particle mass, assuming multiply charged particles are not present and the effective density is constant across the distribution width (this is reasonable because the distributions are narrow, especially at high resolutions). Multiply charged particles may be seen as a second peak if DMA and CPMA resolutions are sufficiently high, although in our experiments, no significant fraction of multiply charged particles were observed. A log-normal distribution (or distribution comprised of two log-normal distributions), as seen in Tajima et al. (2011) was fit to the mass distribution to determine the average particle mass at that set point.

The remaining 0.3 L/min was sent to an SMPS system containing DMA2 (sheath flow 3 L/min) and CPC2, identical to the instruments mentioned above. The charge neutralizer of DMA2 was bypassed because the particles had already been charged while passing through DMA1. DMA2 was stepped through various particle sizes as CPC2 recorded the corresponding number concentration. An inversion code was applied to the data to determine the mobility-equivalent diameter of the particles (Stolzenburg and McMurry, 2008). The total particle size distribution data was also collected by conducting SMPS scans while bypassing DMA1. Number concentrations for denuded scans were corrected for diffusional and thermophoretic losses using an experimentally-determined relationship specific to the thermodenuder.

3.3 Experimental Results

3.3.1 Size Distributions

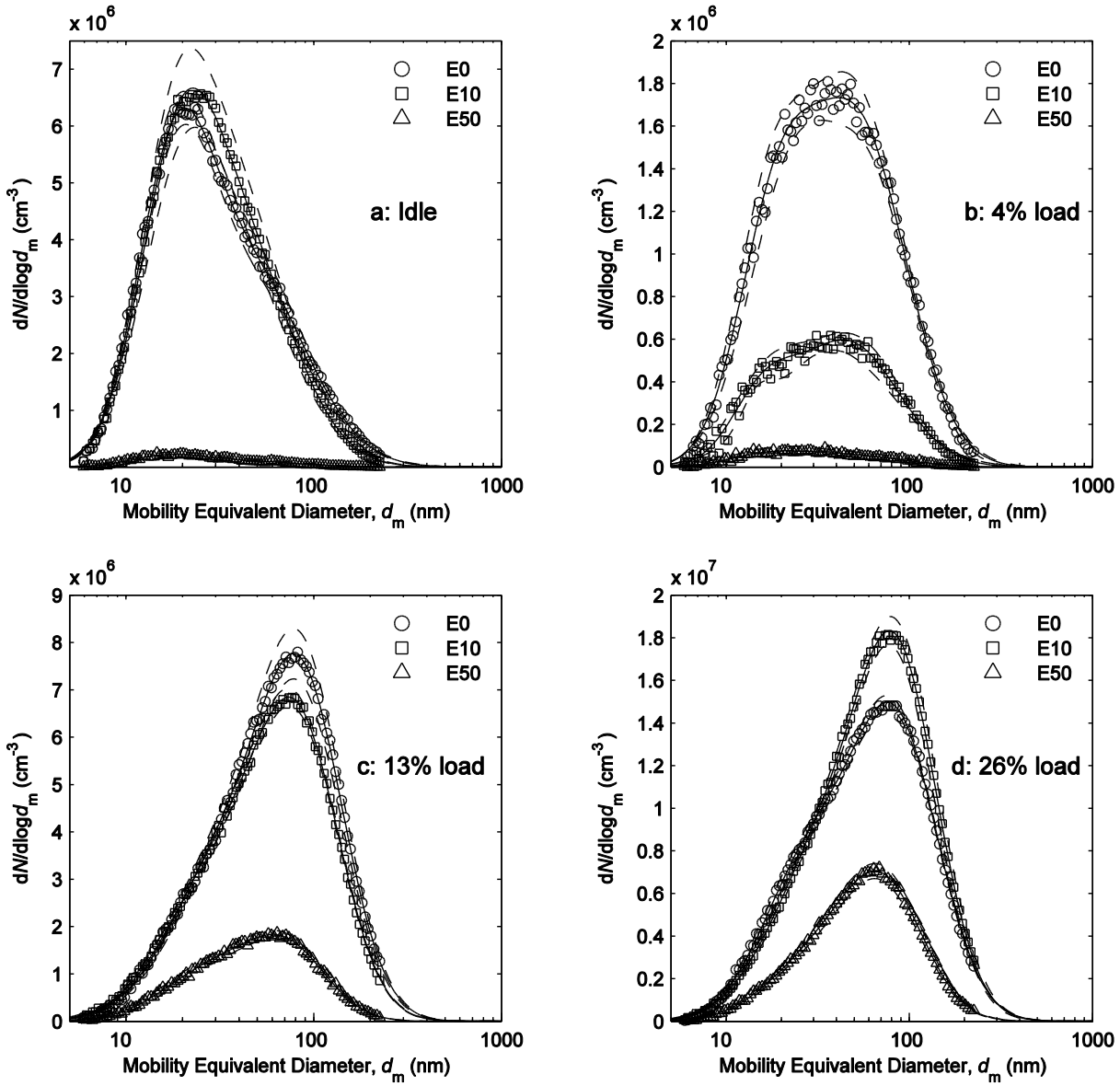

Figure 3.2: Undenuded particle size distributions for idle (a), 4% load (b), 13% load (c), and 26% load (d). Three replicate measurements were taken for each point except for E10 at idle, where seven measurements were taken. Dashed lines represent one standard deviation.

The undenuded size distributions for all fuels and loads are plotted in Figure 3.2. In relation to engine conditions, the geometric mean diameter (GMD) was lowest at idle and increased with load (GMDs at 13% load and 26% load were similar). A small

decrease in GMD was observed as ethanol fraction was increased. Likewise, Zhang et al. (2014) saw a decrease in GMD as ethanol fraction increased, although Storey et al. (2010) did not see a significant change in GMD with ethanol fraction.

It is apparent from Figure 3.2 that the size distributions are not log-normal, but appear to be skewed. It may be possible that these distributions appear skewed because the aerosol is comprised of two log-normal distributions: a nucleation mode (with GMD of ~20 nm) and an accumulation mode (with GMD of ~80 nm). However, this may not be appropriate. The terms imply that two species of PM, formed by two different mechanisms, are present within the particle size distribution. In diesel exhaust, for example, typically volatile liquids grow through nucleation into particles at small diameters (nucleation mode), while aggregates of solid particles accumulate at larger diameters (accumulation mode). As is evident in the next section, very little volatile material is present in the GDI aerosol and there is no distinction between particle morphology across the size range. The mechanism responsible for PM formation may simply result in size distributions which are not log-normal. The non-log-normal distribution shape measured here has been seen from other GDI engines (Gu et al., 2012; Zhang et al., 2014; Momenimovahed and Olfert 2015).

3.3.2 Volatility and mixing state

The number of volatile particles removed after passing through the thermodenuder divided by the total number concentration of the sample (N_{undenude}) is known as the number volatile fraction (f_{N}). This can also be expressed using the number of non-volatile particles measured after denuding (N_{denude}):

$$f_{\text{N}} = 1 - \frac{N_{\text{denude}}}{N_{\text{undenude}}}. \qquad 3.2$$

This value represents the fraction of particles which are purely volatile and contain no soot. N_{denude} and N_{undenude} are obtained by selecting a mobility-equivalent diameter using DMA1 in Figure 3.1 then measuring the number concentration through the heated and bypass lines of the denuder with CPC2 (while bypassing DMA2). f_{N} as a function of mobility equivalent diameter for E0 is displayed in Figure 3.3 (Size-segregated f_{N} plots

for other fuels are displayed in the appendices). f_N is relatively low throughout the size range, at approximately five percent, and there is no observable trend with particle size.

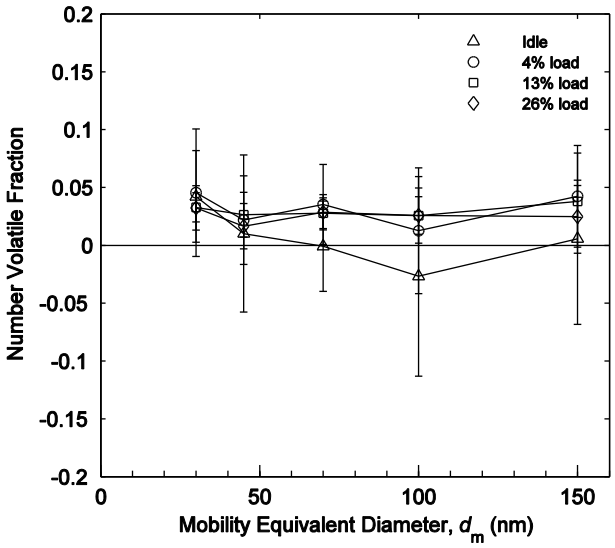

Figure 3.3: f_N as a function of mobility equivalent diameter for E0. Error bars represent one standard deviation.

Similarly, the mass volatile fraction (f_m) can be determined using separate mass measurements of denuded (m_{denude}) and undenuded particles ($m_{undenude}$) by dividing the mass of volatile material on a single particle by the total mass of that particle:

$$f_m = 1 - \frac{m_{denude}}{m_{undenude}}. \quad 3.3$$

This gives a measurement of internally mixed volatility, or a comparison of volatile material to total mass of a given particle. For a given mobility-equivalent diameter selected with the first DMA, m_{denude} and $m_{undenude}$ are the average particle masses measured with the CPMA and CPC1 (Figure 3.1) for particles passing through the heated and bypass lines of the thermodenuder, respectively. f_m as a function of mobility equivalent diameter for E0 is shown in Figure 3.4 (plots for other fuels are shown in the appendices). f_m trends are similar to f_N and remain under 10 percent for all loads and fuels. These results are lower than those from Momenimovahed and Olfert (2015), who determined f_m values in the range of 10% to 30%, and as the volatile fraction increased with power, a decrease with increasing particle size was observed. This negative correlation with size has also been observed by Ghazi et al. (2013) for inverted and

McKenna burners, as well as Graves et al. (2015) for a compression-ignition natural-gas engine.

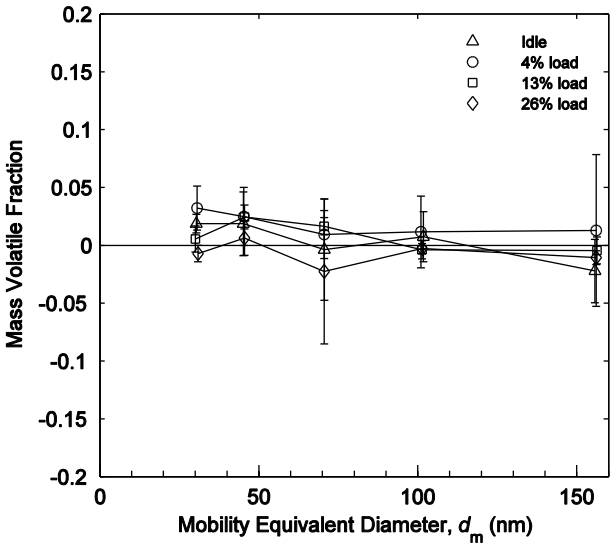

Figure 3.4: f_m as a function of mobility equivalent diameter for E0. Error bars represent one standard deviation.

Because the size-segregated values are relatively constant, it is sufficient to use the average values for subsequent calculations. The average f_N and f_m for each fuel and load are shown in Figure 3.5 and Figure 3.6 respectively. All fractions are seen to be under 5 percent, with some measurements negative due primarily to variability in the engine-out particle concentration. E50 at 4% load and idle have particularly high uncertainty because their number concentrations were extremely low.

Figure 3.5 and Figure 3.6 show that there is a relatively small amount of volatile particulate emitted from the GDI engine post-catalyst. The PM emitted by the engine may already contain little volatility, but even if that is not the case, the catalyst likely oxidizes most volatile material before it is sampled. Samuel et al. (2010) found that during a cold engine start, particle count was reduced by three orders of magnitude after the catalyst, and that during a low speed, low load condition the catalyst reduced PM number by 98 percent. They also note that it is unclear whether the catalyst removes the particles directly or removes their precursors; preventing them from forming or growing. Whelan et al. (2013) also found a sharp decrease in PM number

using a catalyst (65 percent reduction overall with up to 95 percent of particles smaller than 23 nm removed). They determined an effective lightoff temperature where the post-catalyst exhaust temperature is around 80 – 100°C at which point the downstream particle concentration becomes mostly steady. They note that this is significantly lower than the lightoff temperatures for carbon monoxide or hydrocarbons.

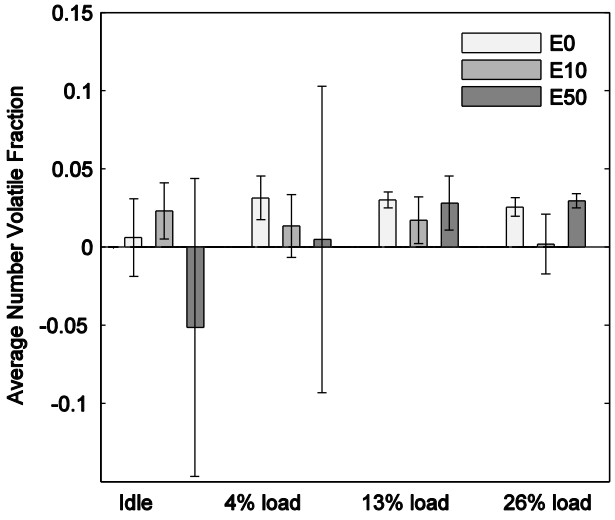

Figure 3.5: Average f_N for all loads and fuels. Error bars represent the standard deviation of data points of all sizes at that fuel and load.

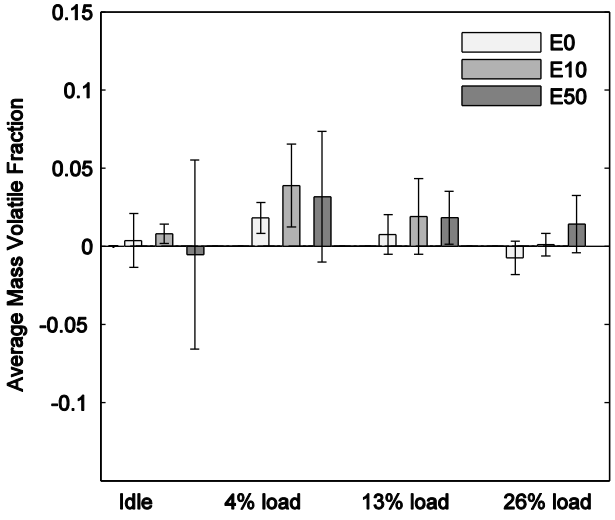

Figure 3.6: Average f_m for all loads and fuels. Error bars represent the standard deviation of data points of all sizes at that fuel and load.

Total number concentrations from undenuded SMPS scans can be multiplied by their respective average f_N values to show the number concentrations of purely volatile particles and particles containing non-volatile solid material ($N_{volatile}$ and $N_{non\text{-}volatile}$). These parameters can be determined as

$$N_{\mathrm{volatile}} = \sum \left(\frac{\mathrm{d}N}{\mathrm{dlog}d_{\mathrm{m}}}\right)(\mathrm{dlog}d_{\mathrm{m}})f_{\mathrm{N}}\ , \qquad 3.4$$

and

$$N_{\mathrm{non-volatile}} = \sum \left(\frac{\mathrm{d}N}{\mathrm{dlog}d_{\mathrm{m}}}\right)(\mathrm{dlog}d_{\mathrm{m}})(1 - f_{\mathrm{N}})\ , \qquad 3.5$$

respectively, where $\frac{\mathrm{d}N}{\mathrm{dlog}d_{\mathrm{m}}}$ is the number concentration of a given particle size bin, normalized by bin width. As shown in Figure 3.7, number concentration is seen to scale with load although idle produced roughly as many particles as at 13% load. Increases in PM with engine load have commonly been seen in the literature (Maricq et al., 1999; Farron et al., 2011; Su et al., 2013; Bonatesta et al., 2014), and this is believed to be due in part to the larger quantity of fuel itself, and also due to the greater cooling effect observed from the fuel evaporation. Number concentrations also decreased with an increase in ethanol fraction, with the exception of E10 at 26% load and idle where the concentration is equal to or slightly higher than the concentration from E0. Maricq et al. (2012) have observed similar trends, where relatively low fractions of ethanol (under 20%) showed a marginal decrease in PM production, while higher fractions (above 30%) reduced PM between 30% and 45%. Moreover, Storey et al. (2010), Storey et al. (2012), Vuk and Vander Griend (2013), and Zhang et al. (2014) also observed decreases in number concentration with the addition of ethanol. Externally mixed volatile particles (shown as the black shaded region) contribute little to the overall concentrations, and little trend is seen in relation to engine condition or fuel type.

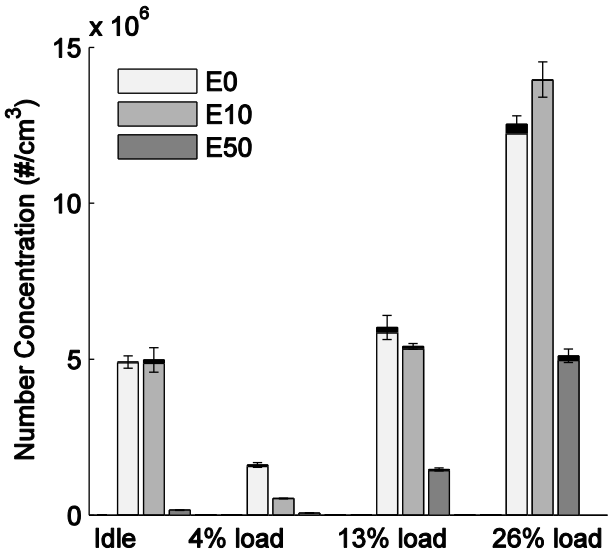

Figure 3.7: Total particle number concentrations. Error bars represent one standard deviation of the total number concentration. Black shading depicts purely volatile particles and other shades particles containing solid particulate.

3.3.3 Effective Density and Mass-Mobility Exponent

The relation between mass and mobility-equivalent diameter can be rearranged to determine particle effective density

$$\rho_{\mathrm{eff}} = \frac{m}{\frac{\pi}{6} {d_{\mathrm{m}}}^3} = \frac{6}{\pi} C {d_{\mathrm{m}}}^{D_{\mathrm{m}}-3} = k {d_{\mathrm{m}}}^{D_{\mathrm{m}}-3}. \qquad 3.6$$

The branching pattern of the aggregate particles incorporates more open space as the particle increases in size, and thus the effective density decreases accordingly. A power-law fit using masses at various mobility-equivalent diameters allows the prefactor k and exponent D_{m} to be calculated.

Denuded effective density measurements for all loads and fuels can be seen in Figure 3.8. Corresponding mass-mobility exponents and prefactors are listed in the legends. A two-way analysis of covariance (ANCOVA) confirmed that both engine condition and ethanol fraction indeed have small but highly statistically significant effects on effective density, with p-values << 0.001. The standard deviation of mass-mobility exponents is 0.10 and 95% of effective density data points are within 21% of a

trend line fit to all data. As can be seen from Figure 3.8, these differences in effective density due to ethanol content and engine condition are very small. Mass-mobility exponent was typically lowest at idle (2.29 – 2.43) and increased with load, although 13% load had exponents which fit inside the range of exponents observed at 26% load (2.49 to 2.60). An increase in ethanol fraction decreased effective density as well as mass-mobility exponent, except at idle. Effective densities observed here are similar to GDI engines tested by Quiros et al. (2015) and Momenimovahed and Olfert (2015), and mass-mobility exponents were also similar (2.3 to 2.5, and 2.61, respectively).

The contrasts in effective density seen at various loads while at 2250 RPM are likely due to the different amounts of fuel being injected, resulting in unique mixing properties. This may result in different levels of charge inhomogeneity and could ultimately dictate the manner in which particles grow. Changes in effective density could be explained with different primary particle sizes. Smaller primary particles will result in aggregates which contain more open space than an aggregate comprised of larger primaries for a given mobility-equivalent diameter. This would give a lower mass and effective density. This agrees well with the density trends seen above, because the increase in density with load may be explained by the fact that the larger quantity of fuel at high load does not mix as well, resulting in locally rich regions in which primary particles are able to grow larger. The addition of ethanol appears to limit this effect, and could be attributed to the oxygen the ethanol molecule providing poorer conditions for soot nucleation.

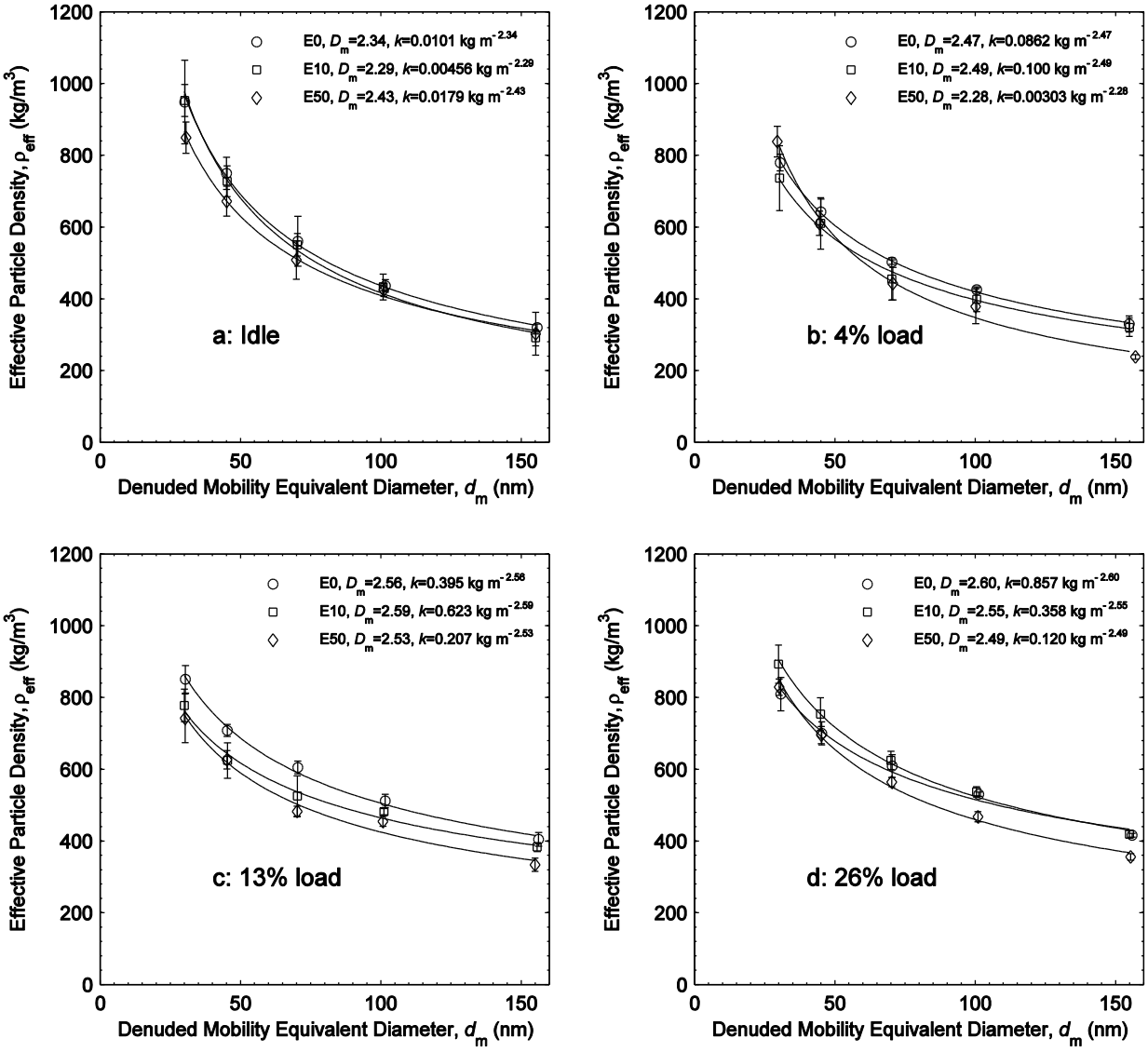

Figure 3.8: Denuded effective density as a function of particle mobility-equivalent diameter for idle (a), 4% load (b), 13% load (c), and 26% load (d). Three replicate measurements were taken for each point. Error bars represent one standard deviation.

The effective density trends produced at idle are noticeably different from the other three engine loads, having lower mass-mobility exponents and higher prefactors. This, along with the fact that many engine parameters are different while at speed versus idle (valve timing, ignition timing, etc.) suggest that idling results in dissimilar combustion in comparison to operation at higher speeds.

3.3.4 Mass Concentration

The SMPS scans were then combined with the number and mass volatile fractions and effective density trend line parameters to calculate the mass concentrations of volatile and non-volatile material. For a given engine condition and fuel, the mass concentration of non-volatile PM was determined by multiplying the number size distribution by particle mass and introducing the number and mass volatile fractions as follows:

$$\left(\frac{\mathrm{d}M}{\mathrm{dlog}d_{\mathrm{m}}}\right)_{\mathrm{non-volatile}} = C_{\mathrm{U}} {d_{\mathrm{m,U}}}^{D_{\mathrm{m,U}}} \left(\frac{\mathrm{d}N_{\mathrm{U}}}{\mathrm{dlog}d_{\mathrm{m,U}}}\right)(1-f_{\mathrm{N}})(1-f_{\mathrm{m}})\,. \qquad 3.7$$

C is the prefactor for the mass-mobility relation, and can be determined from the effective density prefactor ($C = \frac{\pi}{6}k$). f_{N} and f_{m} here are the averages of the size-segregated f_{N} and f_{m}, respectively, as no dependence on size was observed. While this equation calculates the mass distribution of denuded (purely non-volatile) particles, the undenuded diameter and *C* value must be used (as indicated by subscript "U"). Similarly, the internally mixed volatile portion is:

$$\left(\frac{\mathrm{d}M}{\mathrm{dlog}d_{\mathrm{m}}}\right)_{\mathrm{internal\ volatile}} = C_{\mathrm{U}} {d_{\mathrm{m,U}}}^{D_{\mathrm{m,U}}} \left(\frac{\mathrm{d}N_{\mathrm{U}}}{\mathrm{dlog}d_{\mathrm{m,U}}}\right)(1-f_{\mathrm{N}})f_{\mathrm{m}}\,. \qquad 3.8$$

The volatile mass concentration of externally mixed particles is,

$$\left(\frac{\mathrm{d}M}{\mathrm{dlog}d_{\mathrm{m}}}\right)_{\mathrm{external\ volatile}} = \rho_0 \left(\frac{\pi}{6} {d_{\mathrm{m,U}}}^{3}\right)\left(\frac{\mathrm{d}N_{\mathrm{U}}}{\mathrm{dlog}d_{\mathrm{m,U}}}\right) f_{\mathrm{N}}\,, \qquad 3.9$$

where ρ_0 is the density of the externally mixed volatile material assuming the particles are spherical. As density of these particles is not explicitly known, it was assumed they had a density of 1000 kg/m^3. Since the fraction of externally mixed volatile particles was relatively low, this assumption has little effect on the calculated mass concentration.

An example mass distribution is given in Figure 3.9 using E0 at 4% load. The data itself is plotted where possible (i.e. below 225 nm, the upper limit of the SMPS range). An equation comprised of two log-normal distributions was fit to the mass data and is used to extrapolate the mass distribution as shown in the figure. This was done in an

effort to represent the mass distribution without missing a portion of the mass found at larger mobility-equivalent diameters.

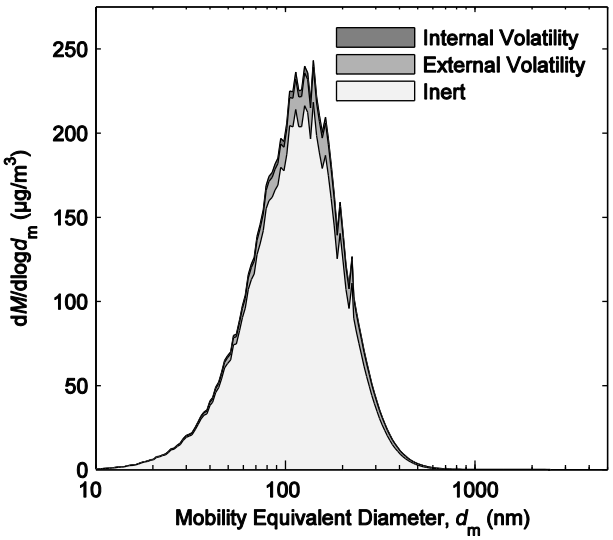

Figure 3.9: Mass distribution of volatile and non-volatile material at 4% load using E0.

The internally and externally mixed volatile mass concentrations can be combined using the formula

$$M_{\text{volatile}} = \sum \left(C_{\text{U}} {d_{\text{m,U}}}^{D_{\text{m,U}}} \left(\frac{\text{d}N_{\text{U}}}{\text{dlog}d_{\text{m,U}}} \right) (\text{dlog}d_{\text{m,U}})(1 - f_{\text{N}}) f_{\text{m}} + \rho_0 \left(\frac{\pi}{6} {d_{\text{m,U}}}^3 \right) \left(\frac{\text{d}N_{\text{U}}}{\text{dlog}d_{\text{m,U}}} \right) (\text{dlog}d_{\text{m,U}}) f_{\text{N}} \right), \quad 3.10$$

where M_{volatile} is the total mass concertation of volatile material. The mass concentration of non-volatile material ($M_{\text{non-volatile}}$) is determined as

$$M_{\text{non-volatile}} = \sum C_{\text{U}} {d_{\text{m,U}}}^{D_{\text{m,U}}} \left(\frac{\text{d}N_{\text{U}}}{\text{dlog}d_{\text{m,U}}} \right) (\text{dlog}d_{\text{m,U}})(1 - f_{\text{N}})(1 - f_{\text{m}}) . \quad 3.11$$

The volatile and non-volatile masses for all fuel and engine conditions are displayed in Figure 3.10. Because both f_{N} and f_{m} are similar between all engine conditions and fuels, the volatile mass concentration tends to scale with number concentration seen in Figure 3.7. Most differences between the two plots can be attributed to variations in size distributions (GMD), which have a large effect on mass concentration. For example, the number concentrations from idle and 13% load are similar, but between the two conditions, idle has the lower mass concentration due to its lower GMD.

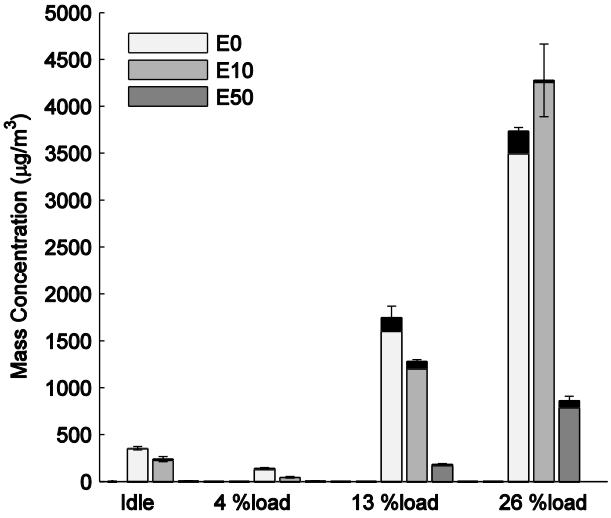

Figure 3.10: Mass concentration of volatile and non-volatile PM. Error bars represent one standard deviation in total mass concentration, black shading depicts volatile material and other shades are non-volatile material.

3.4 Conclusion

Particulate matter from a GDI engine fuelled with ethanol blends has been characterized by its volatility, size distribution, mass-mobility exponent, and effective density. In general, particle number concentration increased with engine load, but idle produced approximately the same number concentrations as 13% load. In terms of mass concentration, the idle condition produced approximately the same as the 4% load. Number and mass concentrations decreased with ethanol fraction, although E10 produced marginally higher number concentrations than E0 at idle and 26% load. Size distributions were not log-normal and were skewed. Both the f_N and f_m were under 10 percent in all instances. Mass-mobility exponent ranged from 2.28 to 2.60. Ethanol fraction and engine load were found to have statistically significant effects on effective density. Ethanol fraction tended to decrease effective density and mass-mobility exponent, except at idle. Effective density and mass-mobility exponent increased with load, and no significant changes were observed in GDI soot after denuding particle samples.

It is clear that blending ethanol with gasoline may be an effective method of reducing GDI particulate emissions. While some statistically significant changes in PM morphology attributable to ethanol (i.e. reductions in effective density and mass-mobility exponent) have been observed, these changes are relatively small and so particle mitigation strategies used for GDI engines fuelled on pure gasoline may not need to be adapted dramatically to suit engines fuelled on ethanol blends. Very little volatility has been observed for this engine, and so a gasoline particulate filter would be a logical next step if further reduction in PM output is desired.

3.4.1 Funding

Funding for this project was provided by the AUTO21 grant program.

3.4.2 Supplemental Material

Supplemental material for this chapter can be seen in Appendix B.

3.4.3 References

Barone, T., Storey, J., Youngquist, A., and Szybist, J. (2012). An Analysis of Direct-Injection Spark-Ignition (DISI) Soot Morphology. *Atmospheric Environment*. 49: 268–274.

Bielaczyc, P., Woodburn, J., and Szczotka, A. (2014). Particulate Emissions from European Vehicles Featuring Direct Injection Spark Ignition Engines Tested Under Laboratory Conditions. *SAE International Journal of Fuels and Lubricants*. 7(2): 580–590.

Bonatesta, F., Chiapetta, E., and La Rocca, A. (2014). Part-Load Particulate Matter from a GDI Engine and the Connection with Combustion Characteristics. *Applied Energy*. 124: 366–376.

Catapano, F., Di Iorio, S., Lazzaro, M., Sementa, P., and Vaglieco, B. (2013). Characterization of Ethanol Blends Combustion Processes and Soot Formation in a GDI Optical Engine. *SAE International*. Doi: 10.4271/2013-01-1316.

Chen, L., Braisher, M., Crossley, A., Stone, R., and Richardson, D. (2010). The Influence of Ethanol Blends on Particulate Matter Emissions from Gasoline Direct Injection Engines. *SAE International*. Doi: 10.4271/2010-01-0793.

Chen, L., Stone, R., and Richardson, D. (2012). Effect of the Valve Timing and the Coolant Temperature on Particulate Emissions from a Gasoline Direct-Injection Engine Fuelled with Gasoline and with a Gasoline–Ethanol Blend. *Proceedings of the Institution of Mechanical Engineers, Part D: Journal of Automobile Engineering*. Doi: 10.1177/0954407012444966.

Chen, L., Zhang, Z., Gong, W., and Liang, Z. (2015). Quantifying the Effects of Fuel Compositions on GDI-Derived Particle Emissions using the Optimal Mixture Design of Experiments. *Fuel*. 154: 252–260.

Dastanpour, R., and Rogak, S. N. (2014). Observations of a Correlation between Primary Particle and Aggregate Size for Soot Particles. *Aerosol Science and Technology*. 48(10): 1043–1049.

Dastanpour, R., Rogak, S., Graves, B., Olfert, J. S., Eggersdorfer, M., and Boies, A. (2015). Improved Sizing of Soot Primary Particles using Mass-Mobility Measurements. *Submitted to Aerosol Science and Technology*.

Energy Information Administration (EIA). Biofuels Issues and Trends. U.S. Department of Energy. Washington DC. October, 2012.

Energy Information Administration (EIA). How Much Ethanol is Produced, Imported, and Consumed in the United States?. http://www.eia.gov/tools/faqs/faq.cfm?id=90&t=4. Updated April 7, 2015. Accessed July 20, 2015.

Energy Information Administration (EIA). Short-Term Energy Outlook (STEO) July 2015. U.S. Department of Energy. Washington DC. July, 2015.

Farron, C., Matthias, N., Foster, D., Andrie, M., Krieger, R., Najt, P., Narayanaswamy, K., Solomon, A., and Zelenyuk, A. (2011). Particulate Characteristics for Varying Engine Operation in a Gasoline Spark Ignited, Direct Injection Engine. *SAE International*. Doi: 10.4271/2011-01-1220.

Fatouraie, M., Wooldridge, M., and Wooldridge, S. (2013). In-Cylinder Particulate Matter and Spray Imaging of Ethanol/ Gasoline Blends in a Direct Injection Spark Ignition Engine. *SAE International Journal of Fuels and Lubricants*. Doi: 10.4271/2013-01-0259.

Ghazi, R., Tjong, H., Soewono, A., Rogak, S. N., and Olfert, J. S. (2013). Mass, Mobililty, Volatility, and Morphology of Soot Particles Generated by a McKenna and Inverted Burner. *Aerosol Science and Technology*. 47(4):395–405.

Giechaskiel, B., Carriero, M., Martini, G., Krasenbrink, A., and Scheder, D. (2009). Calibration and Validation of Various Commercial Particle Number Measurement Systems. *SAE International Journal of Fuels and Lubricants.* 2(1): 512–530.

Graves, B., Olfert, J., Patychuk, B., Dastanpour, R., and Rogak, S. (2015). Characterization of Particulate Matter Morphology and Volatility from a Compression-Ignition Natural Gas Direct-Injection Engine. *Aerosol Science and Technology*. 49(8): 589–598.

Gu, X., Huang, Z., Cai, J., Gong, J., Wu, X., and Lee, C. (2012). Emission Characteristics of a Spark-Ignition Engine Fuelled with Gasoline-n-Butanol Blends in Combination with EGR. *Fuel*. 93: 611–617.

Kameya, Y., and Lee, K. (2013). Ultra-Small-Angle X-ray Scattering Characterization of Diesel/Gasoline Soot: Sizes and Particle-Packing Conditions. *Journal of Nanoparticle Research*. Doi: 10.1007/s11051-013-2006-6.

Karavalakis, G., Short, D., Vu, D., Villila, M., Asa-Awuku, A., and Durbin, T. (2014a). Evaluating the Regulated Emissions, Air Toxics, Ultrafine Particles, and Black Carbon from SI-PFI and SI-DI Vehicles Operating on Different Ethanol and Iso-Butanol Blends. *Fuel.* 128: 410–421.

Khalek, I., Bougher, T., and Jetter, J. (2010). Particle Emissions from a 2009 Gasoline Direct Injection Engine Using Different Commercially Available Fuels. *SAE International Journal of Fuels and Lubricants*. 3(2): 623–637.

Kim, Y. [Yongha], Kim, Y. [Youngjae], Kang, J., Jun, S., Rew, S., and Lee, D. (2013). Fuel Effect on Particle Emissions of a Direct Injection Engine. *SAE International*. Doi: 10.4271/2013-01-1559.

Lee, K., Seong, H., Sakai, S., Hageman, M., and Rothamer, D. (2013). Detailed Morphological Properties of Nanoparticles from Gasoline Direct Injection Engine Combustion of Ethanol Blends. *SAE International*. Doi: 10.4271/2013-24-0185.

Liang, B., Ge, Y., Tan, J., Han, X., Gao, L., Hao, L., Ye, W., and Dai, P. (2013). Comparison of PM Emissions from a Gasoline Direct Injected (GDI) Vehicle and a Port Fuel Injected (PFI) Vehicle Measured by Electrical Low Pressure Impactor (ELPI) with Two Fuels: Gasoline and M15 Methanol Gasoline. *Journal of Aerosol Science*. 57: 22–31.

Liu, Z., Swanson, J., Kittleson, D., and Pui, D. (2012). Comparison of Methods for Online Measurement of Diesel Particulate Matter. *Environmental Science and Technology*. 46(11): 6127–6133.

Maricq, M., Podsiadlik, D., Brehob, D., and Haghgooie, M. (1999). Particulate Emissions from a Direct-Injection Spark-Ignition (DISI) Engine. *Proceedings of the SAE International Spring Fuels and Lubricants Meeting*. Dearborn, MI.

Maricq, M., and Xu, N. (2004). The Effective Density and Fractal Dimension of Soot Particles from Premixed Flames and Motor Vehicle Exhaust. *Journal of Aerosol Science*. 35: 1251–1274.

Maricq, M., Szente, J., and Jahr, K. (2012). The Impact of Ethanol Fuel Blends on PM Emissions from a Light-Duty GDI Vehicle. *Aerosol Science and Technology*. 46(5): 576–583.

Momenimovahed, A., and Olfert, J. S. (2015). Effective Density and Volatility of Particles Emitted from Gasoline Direct Injection Vehicles and Implications for Particle Mass Measurement. *Submitted to Aerosol Science and Technology.*

Olfert, J. S., and Collings, N. (2005). New Method for Particle Classification—The Couette Centrifugal Particle Mass Analyzer. *Journal of Aerosol Science.* 36(11): 1338–1352.

Olfert, J. S., Symonds, J., and Collings, N. (2007). The Effective Density and Fractal Dimension of Particles Emitted from a Light-Duty Diesel Vehicle with a Diesel Oxidation Catalyst. *Journal of Aerosol Science*. 38: 69–82.

Park, K., Cao, F., Kittelson, D., and McMurry, P. (2003). Relationship between Particle Mass and Mobility for Diesel Exhaust Particles. *Environmental Science and Technology*. 37(3): 577–583.

Quiros, D., Hu, S. [Shaohua], Hu, S. [Shishan], Lee, E., Sardar, S., Wang, X., Olfert, J. Jung, H., Zhu, Y., and Huai, T. (2015). Particle Effective Density and Mass During Steady-State Operation of GDI, PFI, and Diesel Passenger Cars. *Journal of Aerosol Science*. 83: 39–54.

Samuel, S., Hassaneen, A., and Morrey, D. (2010). Particulate Matter Emissions and the Role of Catalytic Converter During Cold Start of GDI Engine. *SAE International*. Doi: 10.4271/2010-01-2122.

Seong, H., Choi, S., and Lee, K. (2014). Examination of Nanoparticles from Gasoline Direct-Injection (GDI) Engines using Transmission Electron Microscopy (TEM). International *Journal of Automotive Technology*. 15(2): 175–181.

Sgro, L. A., Sementa, P., Vaglieco, B. M., Rusciano, G., Andrea D'Anna, A., and Minutolo, P. (2012). Investigating the Origin of Nuclei Particles in GDI Engine Exhausts. *Combustion and Flame*. 159: 1687–1692.

Stolzenburg, M., and McMurry, P. (2008). Equations Governing Single and Tandem DMA Configurations and a New Lognormal Approximation to the Transfer Function. *Aerosol Science and Technology*. 42(6): 421–432.

Storey, J., Barone, T., Norman, K., and Lewis, S. (2010). Ethanol Blend Effects On Direct Injection Spark-Ignition Gasoline Vehicle Particulate Matter Emissions. *SAE International Journal of Fuels and Lubricants*. Doi: 10.4271/2010-01-2129.

Storey, J., Barone, T., Thomas, J., and Huff, S. (2012). Exhaust Particle Characterization for Lean and Stoichiometric DI Vehicles Operating on Ethanol-Gasoline Blends. *SAE International*. Doi: 10.4271/2012-01-0437.

Storey, J., Lewis, S., Szybist, J., Thomas, J., Barone, T., Eibl, M., Nafziger, E., and Kaul, B. (2014). Novel Characterization of GDI Engine Exhaust for Gasoline and Mid-Level Gasoline-Alcohol Blends. *SAE International Journal of Fuels and Lubricants*. Doi: 10.4271/2014-01-1606.

Su, J., Lin, W., Sterniak, J., Xu, M., and Bohac, S. (2013). Particulate Matter Emission Comparison of Spark Ignition Direct Injection (SIDI) and Port Fuel Injection (PFI) Operation of a Boosted Gasoline Engine. *Proceedings of the ASME 2013 Internal Combustion Engine Division Fall Technical Conference*. Dearborn, MI.

Symonds, J., Price, P., Williams, P., and Stone, R. (2008). Density of Particles Emitted from a Gasoline Direct Injection Engine. *Proceedings of the European Aerosol Conference*. Thessaloniki, Greece.

Tajima, N., Fukushima, N., Ehara, K. and Sakurai, H. (2011). Mass Range and Optimized Operation of the Aerosol Particle Mass Analyzer. *Aerosol Science and Technology*. 45(2): 196–214.

United Nations Economic Comission for Europe (UNECE). E/ECE/324/Rev.2/Add.100/Rev.3. Agreement Concerning the Adoption of Uniform Technical Prescriptions for Wheeled Vehicles, Equipment and Parts Which can be Fitted and/or be Used on Wheeled Vehicles and the Conditions for Reciprocal Recognition of Approvals Granted on the Basis of these Prescriptions. August, 2013.

U.S. Department of Energy. Ethanol Vehicle Emissions. http://www.afdc.energy.gov/vehicles/flexible_fuel_emissions.html. Accessed August 25, 2015.

Vuk, C., and Vander Griend, S. (2013). Fuel Property Effects on Particulates In Spark Ignition Engines. *SAE International*. Doi: 10.4271/2013-01-1124.

Whelan, I., Timoney, D., and Smith, W. (2013). The Effect of a Three-Way Catalytic Converter on Particulate Matter from a Gasoline Direct-Injection Engine During Cold-Start. *SAE International Journal of Fuels and Lubricants*. Doi: 10.4271/2013-01-1305.

Zhang, Z., Wang, T., Jia, M., Wei, Q., Meng, X., and Shu, G. (2014). Combustion and Particle Number Emissions of a Direct Injection Spark Ignition Engine Operating on Ethanol/Gasoline and n-Butanol/Gasoline Blends with Exhaust Gas Recirculation. *Fuel*. 130: 177–188.

4. Conclusions

Particulate morphology and volatility from direct injection engines of differing sizes, fuel types, and ignition methods has been studied, and while there are some clear discrepancies between their respective PM characteristics, some similarities exist as well. This section provides a summary of the research covered in the previous two chapters, and will compare and contrast the results.

The GDI engine produced fewer particles as ethanol content increased, and the HPDI engine had PM reductions from a decrease in EGR fraction and when the charge was partially premixed. Both engines produced more particles at higher load, which is expected from the larger amount of fuel being injected. At most conditions, both engines produced low levels of internally and externally mixed volatile material. In the case of the GDI, particles were sampled after the catalyst, so any volatile material present beforehand would likely have oxidized before being measured. A topic for follow-up work may be the effects of this catalyst on the PM. The HPDI engine was not fitted with a catalyst, so low volatility was representative of engine-out conditions. The HPDI's PM volatility increased significantly at low loads (and for the premixed mode to some extent) to the point where volatile material was the dominating constituent of internally mixed particles. This may be explained by the fact that production of non-volatile material is more sensitive to load, so a relatively invariable amount of volatile material represents a larger fraction of the PM when low loads produce low amounts of non-volatile material.

While the level of volatility affects the effective density and creates some differences between the undenuded PM of these two engines, the effective densities of inert aggregates are similar. The mass mobility exponent of the trend line combining all HPDI data is 2.45. If the same approach is applied to the GDI data and a single effective density trend is created, its mass-mobility exponent is 2.46. The denuded effective density trends from both engines have been plotted in Figure 4.1, along with data from several other studies. A single trend line was fit to all data sets (mass-mobility exponent of 2.49), and the shaded portion shows that 90% of data points have effective densities within 27% of this trend. There is good alignment between engines, considering the

differences in technologies and fuels. It is apparent however that the GDI densities are generally lower than those from the HPDI engine. Diesel engines tested by Maricq et al. (2004) and Olfert et al. (2007) produced effective densities which agree well with HPDI data and are slightly higher than GDI densities. Park et al. (2003) found densities from another diesel which are seen to be higher than most of the data depicted here, and constitute some of the points which are not enclosed inside the shaded margin. Data from Quiros et al. (2015) for both GDI and PFI engines is included as well. Their effective densities are near the cumulative trend for most sizes, but are low at small sizes. GDI results from Momenimovahed and Olfert (2015) are similar to the GDI results obtained in this study, although their effective densities are slightly higher (and very close to the overall trend line) at approximately 200 nm. As an approximate method, average effective density trends such as this could be used to estimate PM mass concentrations for a wide variety of vehicles with different types of engines and various fuels.

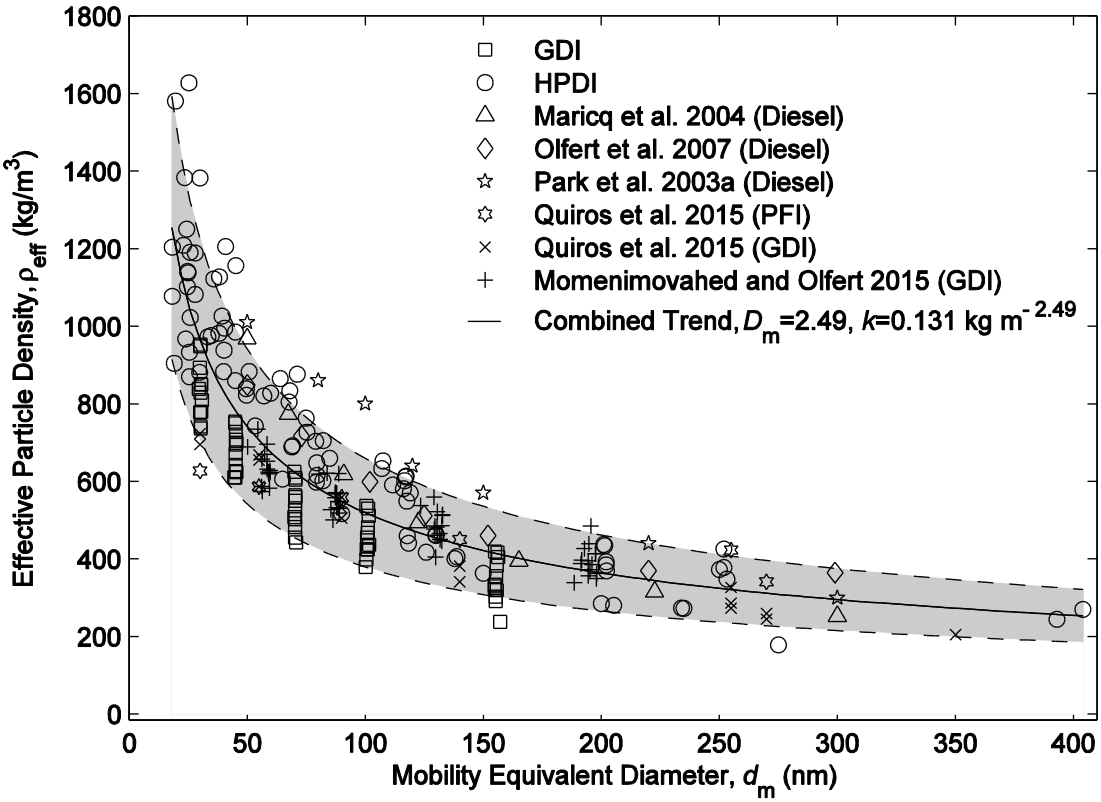

Figure 4.1: Effective density trend combining data from multiple engine types. Shaded region of ±27% encloses 90% of data points.

Regarding mitigation, the presence of both volatile and non-volatile in significant quantities from the HPDI engine suggests that a catalyst as well as a particulate filter would be beneficial. Interestingly, the catalyst is primarily needed for low loads, but it is here that exhaust temperatures are lowest and the catalyst may be less effective. While temperatures are likely to stay above the effective lightoff temperature for PM, strategies to heat the catalyst could be used, such as those discussed in chapter 1.

The GDI was equipped with a TWC, so any further reduction in emissions must come from the installation of a GPF to remove non-volatile PM. As discussed above, it is speculated that the TWC removes almost all volatile material; however the volatility of the engine-out PM remains unknown. A future project may involve characterizing the engine-out PM, and quantifying the effects of the TWC.

This research has elucidated the morphological and volatility properties of PM from these direct injection engines, and has identified strategies for reducing their PM emissions. This information can be applied to future vehicles and can contribute to the development of new regulations. More efficient and sustainable transportation will lead to a reduction of its impact on people and the environment.

4.1 References

Abegglen, M., Durdina, L., Brem, B., Wang, J., Rindlisbacher, T., Corbin, J., Lohmann, U., and Sierau, B. (2015) Effective Density and Mass-Mobility Exponents of Particulate Matter in Aircraft Turbine Exhaust: Dependence on Engine Thrust and Particle Size. *Journal of Aerosol Science*. 88: 135–147.

Albrecht, B. (1989). Aerosols, Cloud Microphysics, and Fractional Cloudiness. *Science*. 245 (4923): 1227–1230.

Alger, T., Gingrich, J., Khalek, I., and Mangold, B. (2010). The Role of EGR in PM Emissions from Gasoline Engines. *SAE International Journal of Fuels and Lubricants*. 3(1): 85–98.

Anderson, J., Thundiyil, J., and Stolbach, A. (2012) Clearing the Air: A Review of the Effects of Particulate Matter Air Pollution on Human Health. *Journal of Medical Toxicology*. 8: 166–175.

Balasubramanian, S., Jittiwat, J., Manikandan, J., Ong, C., Yu, L., and Ong, W. (2010). Biodistribution of Gold Nanoparticles and Gene Expression Changes in the Liver and Spleen after Intravenous Administration in Rats. *Biomaterials*. 31: 2034−2042.

Barone, T. L., Lall, A. A., Storey, J. M. E., Mulholland, G. W., Prikhodko, V. Y., Frankland, J. H., Parks, J. E., and Zachariah, M. R. (2011). Size- Resolved Density Measurements of Particle Emissions from an Advanced Combustion Diesel Engine: Effect of Aggregate Morphology. *Energy and Fuels*. 25(5): 1978–1988.

Barone, T., Storey, J., Youngquist, A., and Szybist, J. (2012). An Analysis of Direct-Injection Spark-Ignition (DISI) Soot Morphology. *Atmospheric Environment*. 49: 268–274.

Bielaczyc, P., Woodburn, J., and Szczotka, A. (2014). Particulate Emissions from European Vehicles Featuring Direct Injection Spark Ignition Engines Tested Under Laboratory Conditions. *SAE International Journal of Fuels and Lubricants*. 7(2): 580–590.

Bonatesta, F., Chiapetta, E., and La Rocca, A. (2014). Part-Load Particulate Matter from a GDI Engine and the Connection with Combustion Characteristics. *Applied Energy*. 124: 366–376.

Boucher, O., Randall, D., Artaxo, P., Bretherton, C., Feingold, G., Forster, P., Kerminen, V. M., Kondo, Y., Liao, H., Lohmann, U., Rasch, P., Satheesh, S., Sherwood, S., Stevens, B., and Zhang, X. (2013). Clouds and Aerosols. In: Climate Change 2013: The Physical Science Basis. Contribution of Working Group I to the Fifth Assessment Report of the Intergovernmental Panel on Climate Change. Cambridge University Press, Cambridge, United Kingdom and New York, NY, USA.

Brasil, A. M., Farias, T. L., and Carvalho, M. G. (1999). A Recipe for Image Characterization of Fractal-Like Aggregates. *Journal of Aerosol Science*. 30(10): 1379–1389.

Bullock, D. S., and Olfert, J. S. (2014). Size, Volatility, and Effective Density of Particulate Emissions from a Homogeneous Charge Compression Ignition Engine Using Compressed Natural Gas. *Journal of Aerosol Science*. 75: 1–8.

Burtscher, H. (2005) Physical Characterization of Particulate Emissions from Diesel Engines: a Review. *Journal of Aerosol Science*. 36: 896–932.

Canadian Medical Association (CMA). No Breathing Room: National Illness Costs of Air Pollution. Summary Report. August, 2008.

Car and Driver. 2009 Chevrolet Cobalt SS Sedan. http://buyersguide.caranddriver.com/chevrolet/cobalt/2009/chevrolet-cobalt-ss-sedan/specs. Accessed June 2, 2014.

Catapano, F., Di Iorio, S., Lazzaro, M., Sementa, P., and Vaglieco, B. M. (2013). Characterization of Ethanol Blends Combustion Processes and Soot Formation in a GDI Optical Engine. *SAE International*. Doi: 10.4271/2013-01-1316.

Chan, T., Meloche, E., Kubsh, J., Brezny, R., Rosenblatt, D., and Rideout, G. (2013). Impact of Ambient Temperature on Gaseous and Particle Emissions from a Direct Injection Gasoline Vehicle and its Implications on Particle Filtration. *SAE International Journal of Fuels and Lubricants*. Doi: 10.4271/2013-01-0527.

Chen, L., Braisher, M., Crossley, A., Stone, R., and Richardson, D. (2010). The Influence of Ethanol Blends on Particulate Matter Emissions from Gasoline Direct Injection Engines. *SAE International*. Doi: 10.4271/2010-01-0793.

Chen, L., Stone, R., and Richardson, D. (2012). Effect of the Valve Timing and the Coolant Temperature on Particulate Emissions from a Gasoline Direct-Injection Engine Fuelled with Gasoline and with a Gasoline–Ethanol Blend. Proceedings of the Institution of Mechanical Engineers, Part D: *Journal of Automobile Engineering*. Doi: 10.1177/0954407012444966.

Chen, L., Zhang, Z., Gong, W., and Liang, Z. (2015). Quantifying the Effects of Fuel Compositions on GDI-Derived Particle Emissions using the Optimal Mixture Design of Experiments. *Fuel*. 154: 252–260.

Chuepeng, S., Xu, H., Tsolakis, A., Wyszynski, M., and Price, P. (2011). Particulate Matter Size Distribution in the Exhaust Gas of a Modern Diesel Engine Fuelled with a Biodiesel Blend. *Biomass and Bioenergy*. 35: 4280–4289.

Clancy L, Goodman P, Sinclair H, and Dockery D. (2002). Effect of Air-Pollution Control on Death Rates in Dublin, Ireland: an Intervention Study. *Lancet*. 360: 1210–1214.

Dastanpour, R., and Rogak, S. N. (2014). Observations of a Correlation between Primary Particle and Aggregate Size for Soot Particles. *Aerosol Science and Technology*. 48(10): 1043–1049.

Dastanpour, R., Rogak, S., Graves, B., Olfert, J. S., Eggersdorfer, M., and Boies, A. (2015). Improved Sizing of Soot Primary Particles using Mass-Mobility Measurements. *Submitted to Aerosol Science and Technology*.

Durdina, L., Brem, B. T., Abegglen, M., Lobo, P., Rindlisbacher, T., Thomson, K. A., Smallwood, G. J., Hagen, D. E., and Wang, J. (2014). Determination of PM Mass Emissions from an Aircraft Turbine Engine using Particle Effective Density. *Atmospheric Environment*. 99: 500–507.

Edmunds. 2009 Chevrolet Cobalt – Features & Specs. http://www.edmunds.com/chevrolet/cobalt/2009/features-specs.html. Accessed June 2, 2014.

Energy Information Administration (EIA). Biofuels Issues and Trends. U.S. Department of Energy. Washington DC. October, 2012.

Energy Information Administration (EIA). How Much Ethanol is Produced, Imported, and Consumed in the United States?. http://www.eia.gov/tools/faqs/faq.cfm?id=90&t=4. Updated April 7, 2015. Accessed July 20, 2015.

Energy Information Administration (EIA). Short-Term Energy Outlook (STEO) July 2015. U.S. Department of Energy. Washington DC. July, 2015.

Environmental Protection Agency (EPA). Application for Certification 2009 Model Year: Chevrolet Cobalt. August, 2008.

Environmental Protection Agency (EPA). Technical Bulletin: Diesel Particulate Filter Operation and Maintenance. May, 2010.

European Union (EU) Directive 1999/96/EC of the European Parliament and of the Council. December, 1999.

European Union (EU) Directive 2003/17/EC of the European Parliament and of the Council. March, 2003.

European Environment Agency (EEA). Regulation (EC) No 715/2007 of the European Parliament and of the council. June, 2007.

European Environment Agency (EEA). Regulation (EC) No 692/2008. Implementing and amending Regulation (EC) No 715/2007 of the European Parliament and of the Council on Type-Approval of Motor Vehicles with Respect to Emissions from Light Passenger and Commercial Vehicles (Euro 5 and Euro 6) and on Access to Vehicle Repair and Maintenance Information. July, 2008.

European Environment Agency (EEA). Regulation (EC) No 459/2012. Amending Regulation (EC) No 715/2007 of the European Parliament and of the Council and Commission Regulation (EC) No 692/2008 as Regards Emissions from Light Passenger and Commercial Vehicles (Euro 6). May, 2012.

Faghani, E., Patychuk, B. D., McTaggart-Cowan, G. P., and Rogak, S. N. (2013). Soot Emission Reduction from Post Injection Strategies in a High Pressure Direct-Injection Natural Gas Engine. *SAE International*. Doi: 10.4271/2013-24-0114.

Farron, C., Matthias, N., Foster, D., Andrie, M., Krieger, R., Najt, P., Narayanaswamy, K., Solomon, A., and Zelenyuk, A. (2011). Particulate Characteristics for Varying Engine Operation in a Gasoline Spark Ignited, Direct Injection Engine. *SAE International*. Doi: 10.4271/2011-01-1220.

Fatouraie, M., Wooldridge, M., and Wooldridge, S. (2013). In-Cylinder Particulate Matter and Spray Imaging of Ethanol/ Gasoline Blends in a Direct Injection Spark Ignition Engine. *SAE International Journal of Fuels and Lubricants*. Doi: 10.4271/2013-01-0259.

Fujita, E., Zielinska, B., Campbell, D., Arnott, P., Sagebiel, J., Mazzoleni, L., Chow, J., Gabele, P., Crews, W., Snow, R., Clark, N., Wayne, S., and Lawson, D. (1995) Variations in Speciated Emissions from Spark-Ignition and Compression-Ignition Motor Vehicles in California's South Coast Air Basin. *Journal of the Air and Waste Management Association*. 57(6): 705–720.

Ghazi, R., and Olfert, J. S. (2013). Coating Mass Dependence of Soot Aggregate Restructuring Due to Coatings of Oleic Acid and Dioctyl Sebacate. *Aerosol Science and Technology*. 47(2):192–200.

Ghazi, R., Tjong, H., Soewono, A., Rogak, S. N., and Olfert, J. S. (2013). Mass, Mobililty, Volatility, and Morphology of Soot Particles Generated by a McKenna and Inverted Burner. *Aerosol Science and Technology*. 47(4):395–405.

Giechaskiel, B., Carriero, M., Martini, G., Krasenbrink, A., and Scheder, D. (2009). Calibration and Validation of Various Commercial Particle Number Measurement Systems. *SAE International Journal of Fuels and Lubricants*. 2(1): 512–530.

Giechaskiel, B., Maricq, M., Ntziachristos, L., Dardiotis, C., Wang, X., Azmann, H., Bergmann, A., and Schindler, W. (2014). Review of Motor Vehicle Particulate Emissions Sampling and Measurement: From Smoke and Filter Mass to Particle Number. *Journal of Aerosol Science*. 67: 48–86.

Giordano, M., Espinoza, C., and Asa-Awuku, A. (2015). Experimentally Measured Morphology of Biomass Burning Aerosol and its Impacts on CCN Ability. *Atmospheric Chemistry and Physics*. 15(4): 1807–1821.

Glassman, I. (1989). Soot Formation in Combustion Processes. *Symposium (International) on Combustion*. 22(1): 295–311.

Goldenberg, E., Prigent, M., and Caillod, J. (1983) Depolluting Exhaust Gases from Diesel Engines by Catalytic Mufflers. *Oil and Gas Technology*. 38(6): 793–805.

Gormley, P. G., and Kennedy, M. (1949). Diffusion from a Stream Flowing Through a Cylindrical Tube. *Proceedings of the Royal Irish Academy*. 52A: 163–169.

Graves, B., Olfert, J., Patychuk, B., Dastanpour, R., and Rogak, S. (2015). Characterization of Particulate Matter Morphology and Volatility from a Compression-Ignition Natural Gas Direct-Injection Engine. *Aerosol Science and Technology*. 49(8): 589–598.

Gu, X., Huang, Z., Cai, J., Gong, J., Wu, X., and Lee, C. (2012). Emission Characteristics of a Spark-Ignition Engine Fuelled with Gasoline-n-Butanol Blends in Combination with EGR. *Fuel*. 93: 611–617.

Gupta, J., Agarwal, A., and Aggarwal, S. (2014) Particulate Emissions from Karanja Biodiesel Fuelled Turbocharged CRDI SUV Engine. Proceedings of the *ASME Internal Combustion Engine Division Fall Technical Conference*. October 19 – 22. Columbus, IN.

Hedge, M., Weber, P., Gingrich, J., Alger, T., and Khalek, I. (2011). Effect of EGR on Particle Emissions from a GDI Engine. *SAE International Journal of Engines*. Doi: 10.4271/2011-01-0636.

Hinds, W. (1999) Aerosol Technology: Properties, Behavior, and Measurement of Airborne Particles, 2nd Edition. John Wiley and Sons. Hoboken, NJ.

Hoet, P., Brüske-Hohlfeld, I., and Salata, O. (2004). Nanoparticles – Known and Unknown Health Risks. *Journal of Nanobiotechnology*. Doi: 10.1186/1477-3155-2-12

Intergovernmental Panel on Climate Change (IPCC). (2013) Climate Change 2013: The Physical Science Basis, Working Group 1.

Johnson, T. (2012). Vehicular Emissions in Review. *SAE International Journal of Engines*. 5: 216–234.

Johnson, T., Olfert, J. S., Symonds, J., Johnson, M., Rindlisbacher, T., Swanson, J. J., Boies, A. M., Thomson, K., Smallwood, G., Walters, D., Sevcenco, Y., Crayford, A., Durdina, L., Bahk, Y. K., Brem, B., and Wang, J. (2015). Effective Density and Mass-Mobility Exponent of Aircraft Turbine Particulate Matter. *Journal of Propulsion and Power*. 31(2): 573–582.

Jones, H. L. (2004). Source and Characterization of Particulate Matter from a Pilot-Ignited Natural Gas Fuelled Engine. M.Sc. thesis. University of British Columbia, Vancouver, Canada.

Kameya, Y., and Lee, K. (2013). Ultra-Small-Angle X-Ray Scattering Characterization of Diesel/Gasoline Soot: Sizes and Particle-Packing Conditions. *Journal of Nanoparticle Research*. Doi: 10.1007/s11051-013-2006-6.

Karavalakis, G., Short, D., Vu, D., Villela, M., Asa-Awuku, A., and Durbin, T. D. (2014a). Evaluating the Regulated Emissions, Air Toxics, Ultrafine Particles, and Black Carbon from SI-PFI and SI-DI Vehicles Operating on Different Ethanol and Iso-Butanol Blends. *Fuel*. 128: 410–421.

Karavalakis, G., Short, D., Russell, R., Jung, H., Johnson, K., Asa-Awuku, A., and Durbin, T. (2014b). Assessing the Impacts of Ethanol and Isobutanol on Gaseous and Particulate Emissions from Flexible Fuel Vehicles. *Environmental Science and Technology*. 48: 14016–14024.

Karavalakis, G., Short, D., Vu, D., Russell, R., Hajbabaie, M., Asa-Awuku, A., and Durbin, T. (2015). Evaluating the Effects of Aromatics Content in Gasoline on Gaseous and Particulate Matter Emissions from SI-PFI and SIDI Vehicles. *Environmental Science and Technology*. 49: 7021–7031.

Khalek, I., Bougher, T., and Jetter, J. (2010). Particle Emissions from a 2009 Gasoline Direct Injection Engine Using Different Commercially Available Fuels. *SAE International Journal of Fuels and Lubricants*. 3(2): 623–637.

Kim, Y. [Yongha], Kim, Y. [Youngjae], Kang, J., Jun, S., Rew, S., and Lee, D. (2013). Fuel Effect on Particle Emissions of a Direct Injection Engine. *SAE International*. Doi: 10.4271/2013-01-1559.

Kittelson, D. B. (1998). Engines and Nanoparticles: A Review. *Journal of Aerosol Science*. 29:575–588.

Lee, K. O., Cole, R., Sekar, R., Choi, M. Y., Kang, J. S., Bae, C. S., and Shin, H. D. (2002). Morphological Investigation of the Microstructure, Dimensions, and Fractal Geometry of Diesel Particulates. *Proceedings of the Combustion Institute*. 29(1): 647–653.

Lee, K., Seong, H., Sakai, S., Hageman, M., and Rothamer, D. (2013). Detailed Morphological Properties of Nanoparticles from Gasoline Direct Injection Engine Combustion of Ethanol Blends. *SAE International*. Doi: 10.4271/2013-24-0185.

Liang, B., Ge, Y., Tan, J., Han, X., Gao, L., Hao, L., Ye, W., and Dai, P. (2013). Comparison of PM Emissions from a Gasoline Direct Injected (GDI) Vehicle and a Port Fuel Injected (PFI) Vehicle Measured by Electrical Low Pressure Impactor (ELPI) with Two Fuels: Gasoline and M15 Methanol Gasoline. *Journal of Aerosol Science*. 57: 22–31.

Liu, B., Hayes, R., Checkel, M., Zheng, M., and Mirosh, E. (2000). Reversing Flow Catalytic Converter for a Natural Gas/Diesel Dual Fuel Engine. *Chemical Engineering Science*. 56: 2641–2658.

Liu, Z., Swanson, J., Kittleson, D., and Pui, D. (2012). Comparison of Methods for Online Measurement of Diesel Particulate Matter. *Environmental Science and Technology*. 46(11): 6127–6133.

Mabson, C. (2015). Emissions Characterization of Paired Gaseous Jets in a Pilot-Ignited Natural-Gas Compression-Ignition Engine. M.Sc. thesis. University of British Columbia, Vancouver, Canada.

Maricq, M., Podsiadlik, D., Brehob, D., and Haghgooie, M. (1999). Particulate Emissions from a Direct-Injection Spark-Ignition (DISI) Engine. *Proceedings of the SAE International Spring Fuels and Lubricants Meeting*. Dearborn, MI.

Maricq, M., and Xu, N. (2004). The Effective Density and Fractal Dimension of Soot Particles from Premixed Flames and Motor Vehicle Exhaust. *Journal of Aerosol Science*. 35: 1251–1274.

Maricq, M. (2007) Chemical Characterization of Particulate Emissions from Diesel Engines: A Review. *Journal of Aerosol Science*. 38: 1079–1118.

Maricq, M., Szente, J., and Jahr, K. (2012). The Impact of Ethanol Fuel Blends on PM Emissions from a Light-Duty GDI Vehicle. *Aerosol Science and Technology*. 46(5): 576–583.

Mathis, U., Mohr, M., and Forss, A. (2005). Comprehensive Particle Characterization of Modern Gasoline and Diesel Passenger Cars at Low Ambient Temperatures. *Atmospheric Environment*. 39: 107–117.

McTaggart-Cowan, G. P., Jones, H. L., Rogak, S. N., Bushe, W. K., Hill, P. G., and Munshi, S. R. (2007). The Effects of High-Pressure Injection on a Compression-Ignition, Direct Injection of Natural Gas Engine. *ASME Journal for Engineering Gas Turbines and Power*. 129: 579–588.

McTaggart-Cowan, G. P., Mann, K., Huang, J., Wu, N., and Munshi, S. R. (2012). Particulate Matter Reduction from a Pilot-Ignited, Direct Injection of Natural Gas Engine. *Proceedings of the ASME Internal Combustion Engine Division Fall Technical Conference*, September 23–26, Vancouver, Canada, pp. 427–437.

Medalia, A. I., and Heckman, F. A. (1969). Morphology of Aggregates—II. Size and Shape Factors of Carbon Black Aggregates from Electron Microscopy. *Carbon*. 7(5): 567–582.

Miller K., Siscovick D., Sheppard L., Shepherd K., Sullivan J., Anderson, G., and Kaufman, J. (2007). Long-Term Exposure to Air Pollution and Incidence of Cardiovascular Events in Women. *New England Journal of Medicine*. 356: 447–458.

Momenimovahed, A., and Olfert, J. S. (2015). Effective Density and Volatility of Particles Emitted from Gasoline Direct Injection Vehicles and Implications for Particle Mass Measurement. *Submitted to Aerosol Science and Technology.*

Mustafi, N. N., Raine, R. R., and James, B. (2010). Characterization of Exhaust Particulates from a Dual Fuel Engine by TGA, XPS, and Raman Techniques. *Aerosol Science and Technology*. 44(11): 954–963.

Neer, A., and Koylu, U. O. (2006). Effect of Operating Conditions on the Size, Morphology, and Concentration of Submicrometer Particulates Emitted from a Diesel Engine. *Combustion and Flame*. 146(1–2): 142–154.

Oh, C., and Cha, G. (2012). Influence of Oxygenate Content on Particulate Matter Emission in Gasoline Direct Injection Engine. *International Journal of Automotive Technology*. 14(6): 829–836.

Olfert, J. S., and Collings, N. (2005). New Method for Particle Classification—The Couette Centrifugal Particle Mass Analyzer. *Journal of Aerosol Science*. 36(11): 1338–1352.

Olfert, J. S., Symonds, J., and Collings, N. (2007). The Effective Density and Fractal Dimension of Particles Emitted from a Light-Duty Diesel Vehicle with a Diesel Oxidation Catalyst. *Journal of Aerosol Science.* 38: 69–82.

Park, K., Cao, F., Kittelson, D., and McMurry, P. (2003). Relationship between Particle Mass and Mobility for Diesel Exhaust Particles. *Environmental Science and Technology*. 37(3): 577–583.

Park, K., Kittelson, D.B., and McMurry, P.H. (2004). Structural Properties of Diesel Exhaust Particles Measured by Transmission Electron Microscopy (TEM): Relationships to Particle Mass and Mobility. *Aerosol Science and Technology*. 38(9): 881–889.

Park, S. H., Rogak, S. N., Bushe, W. K., Wen, J. Z., and Thomson, M. J. (2005). An Aerosol Model to Predict Size and Structure of Soot Particles. *Combustion Theory and Modelling*. 9(3): 499–513.

Patychuk, B. D. (2013). Particulate Matter Emission Characterization from a Natural Gas High-Pressure Direct-Injection Engine. M.Sc. thesis. University of British Columbia, Vancouver, Canada.

Patychuk, B. D., and Rogak, S. N. (2012). Particulate Matter Emission Characterization from a Natural Gas Fuelled High Pressure Direct Injection Engine. *Proceedings of the ASME Internal Combustion Engine Division Fall Technical Conference*. September 23–26, Vancouver, Canada, pp. 447–455.

Pei, Y., Qin, J., and Pan, S. (2014). Experimental Study on the Particulate Matter Emission Characteristics for a Direct-Injection Gasoline Engine. *Proceedings of the Institution of Mechanical Engineers, Part D: Journal of Automobile Engineering*. Doi: 10.1177/0954407013493899.

Quiros, D., Hu, S. [Shaohua], Hu, S. [Shishan], Lee, E., Sardar, S., Wang, X., Olfert, J. Jung, H., Zhu, Y., and Huai, T. (2015). Particle Effective Density and Mass During Steady-State Operation of GDI, PFI, and Diesel Passenger Cars. *Journal of Aerosol Science*. 83: 39–54.

Riediker, M., Cascio, W., Griggs, T., Herbst, M., Bromberg, P., Neas, L., Williams, R., and Delvin, R. (2004) Particulate Matter Exposure in Cars is Associated with Cardiovascular Effects in Healthy, Young Men. *American Journal of Respiratory and Critical Care Medicine*. Doi: 10.1164/rccm.200310-1463OC.

Ristimäki, J., Vaaraslahti, K., Lappi, M., and Keskinen, J. (2007). Hydrocarbon Condensation in Heavy-Duty Diesel Exhaust. *Environmental Science and Technology*. 41: 6397–6402.

Rogak, S. N., Flagan, R. C., and Nguyen, H. V. (1993). The Mobility and Structure of Aerosol Agglomerates. *Aerosol Science and Technology*. 18(1): 25–47.

Sabathil, D., Koenigstein, A., Schaffner, P., Fritzsche, J., and Doehler, A. (2011). The Influence of DISI Engine Operating Parameters on Particle Number Emissions. *SAE International*. Doi: 10.4271/2011-01-0143.

Saeed, K., Fletcher, N., and Salvage, J. (2014). Measurements of the Characteristics of Particle Emissions from a Port Fuel Injection Engine. *Journal of Automobile Engineering*. Doi: 10.1177/0954407014559564.

Sakai, S., Hageman, M., and Rothamer, D. (2013). Effect of Equivalence Ratio on the Particulate Emissions from a Spark-Ignited, Direct-Injected Gasoline Engine. *SAE International*. Doi: 10.4271/2013-01-1560.

Sakurai, H., Park, K., McMurry, P. H., Zarling, D. D., Kittleson, D. B., and Ziemann, P. J. (2003). Size-Dependent Mixing Characteristics of Volatile and Nonvolatile Components in Diesel Exhaust Aerosols. *Environmental Science and Technology*. 37: 5487–5495.

Samuel, S., Hassaneen, A., and Morrey, D. (2010). Particulate Matter Emissions and the Role of Catalytic Converter During Cold Start of GDI Engine. *SAE International*. Doi: 10.4271/2010-01-2122.

Seong, H., Choi, S., and Lee, K. (2014). Examination of Nanoparticles from Gasoline Direct-Injection (GDI) Engines Using Transmission Electron Microscopy (TEM). *International Journal of Automotive Technology*. 15(2): 175–181.

Sgro, L. A., Sementa, P., Vaglieco, B. M., Rusciano, G., Andrea D'Anna, A., and Minutolo, P. (2012). Investigating the Origin of Nuclei Particles in GDI Engine Exhausts. *Combustion and Flame*. 159: 1687–1692.

Slowik, J. G., Cross, E. S., Han, J. H., Kolucki, J., Davidovits, P., Williams, L. R., Onasch, T. B., Jayne, J. T., Kolb, C. E., and Worsnop, D. R. (2007). Measurements of Morphology Changes of Fractal Soot Particles Using Coating and Denuding

Experiments: Implications for Optical Absorption and Atmospheric Lifetime. *Aerosol Science and Technology*. 41(8): 734–750.

Soewono, A. (2008). Morphology and Microsctructure of Diesel Particulates. M.Sc. thesis. University of British Columbia, Vancouver, Canada.

Steimle, F., Kulzer, A., Richter, H., Schwarzenthal, D., and Romberg, C. (2013). Systematic Analysis and Particle Emission Reduction of Homogeneous Direct Injection SI Engines. *SAE International*. Doi: 10.4271/2013-01-0248.

Stolzenburg, M., and McMurry, P. (2008). Equations Governing Single and Tandem DMA Configurations and a New Lognormal Approximation to the Transfer Function. *Aerosol Science and Technology*. 42(6): 421–432.

Stone, R. (1999). Introduction to Internal Combustion Engines, 3rd Edition. Palgrave Macmillan. Basingstoke, UK.

Stone, R. (2012). Introduction to Internal Combustion Engines, 4th Edition. Palgrave Macmillan. Basingstoke, UK.

Storey, J., Barone, T., Norman, K., and Lewis, S. (2010). Ethanol Blend Effects On Direct Injection Spark-Ignition Gasoline Vehicle Particulate Matter Emissions. *SAE International Fall Fuels and Lubricants*. Doi: 10.4271/2010-01-2129.

Storey, J., Barone, T., Thomas, J., and Huff, S. (2012). Exhaust Particle Characterization for Lean and Stoichiometric DI Vehicles Operating on Ethanol-Gasoline Blends. *SAE International*. Doi: 10.4271/2012-01-0437.

Storey, J., Lewis, S., Szybist, J., Thomas, J., Barone, T., Eibl, M., Nafziger, E., and Kaul, B. (2014). Novel Characterization of GDI Engine Exhaust for Gasoline and Mid-

Level Gasoline-Alcohol Blends. *SAE International Journal of Fuels and Lubricants*. Doi: 10.4271/2014-01-1606.

Su, J., Lin, W., Sterniak, J., Xu, M., and Bohac, S. (2013). Particulate Matter Emission Comparison of Spark Ignition Direct Injection (SIDI) and Port Fuel Injection (PFI) Operation of a Boosted Gasoline Engine. *Proceedings of the ASME Internal Combustion Engine Division Fall Technical Conference*. Dearborn, MI.

Symonds, J., Price, P., Williams, P., and Stone, R. (2008). Density of Particles Emitted from a Gasoline Direct Injection Engine. *Proceedings of the European Aerosol Conference*. Thessaloniki, Greece.

Tajima, N., Fukushima, N., Ehara, K., and Sakurai, H. (2011). Mass Range and Optimized Operation of the Aerosol Particle Mass Analyzer. *Aerosol Science and Technology*. 45(2): 196–214.

Tian, K., Liu, F., Yang, M., Thomson, K. A., Snelling, D. R., and Smallwood, G. J. (2007). Numerical Simulation Aided Relative Optical Density Analysis of TEM Images for Soot Morphology Determination. *Proceedings of the Combustion Institute*. 31(1): 861–868.

Vuk, C., and Vander Griend, S. (2013). Fuel Property Effects on Particulates In Spark Ignition Engines. *SAE International*. Doi: 10.4271/2013-01-1124.

United Nations Economic Comission for Europe (UNECE). E/ECE/324/Rev.2/Add.100/Rev.3. Agreement Concerning the Adoption of Uniform Technical Prescriptions for Wheeled Vehicles, Equipment and Parts Which can be Fitted and/or be Used on Wheeled Vehicles and the Conditions for Reciprocal Recognition of Approvals Granted on the Basis of these Prescriptions. August, 2013.

U.S. Department of Energy. Ethanol Vehicle Emissions. http://www.afdc.energy.gov/vehicles/flexible_fuel_emissions.html. Accessed August 25, 2015.

Wentzel, M., Gorzawski, H., Naumann, K.-H., Saathoff, H., and Weinbruch, S. (2003). Transmission Electron Microscopical and Aerosol Dynamical Characterization of Soot Aerosols. *Journal of Aerosol Science*. 34(10): 1347–1370.

Westport Innovations Inc. First Generation Westport HPDI Technology. http://www.westport.com/is/core-technologies/combustion/hpdi. Accessed July 30, 2015.

Whelan, I., Timoney, D., and Smith, W. (2013). The Effect of a Three-Way Catalytic Converter on Particulate Matter from a Gasoline Direct-Injection Engine During Cold-Start. *SAE International Journal of Fuels and Lubricants*. Doi: 10.4271/2013-01-1305.

Wirojsakunchai, E., Aroonsrisopon, T., Wannatong, K., and Akarapanjavit, N. (2009). A Simulation Study of an Aftertreatment System Level Model for Diesel Dual Fuel (DDF) Engine Emission Control. *SAE International*. Doi: 10.4271/2009-01-1966.

Wong, J. (2001). Theory of Ground Vehicles, 3rd edition. John Wiley & Sons, New York, p.10.

Wong, W., Midkiff, K., and Bell, S. (1991). Performance and Emissions of Natural Gas Dual-Fueled, Direct Injected Diesel Engine. *SAE International*. Doi: 10.4271/911766.

World Health Organization (WHO) (2014). Ambient (Outdoor) Air Quality and Health. http://www.who.int/mediacentre/factsheets/fs313/en/. Accessed July 30, 2015.

Young, L., Liou, Y., Cheng, M., Lu, J., Yang, H., Tsai, Y., Wang, L., Chen, C., and Lai, J. (2012). Effects of Biodiesel, Engine Load and Diesel Particulate Filter on Nonvolatile

Particle Number Size Distributions in Heavy-Duty Diesel Engine Exhaust. *Journal of Hazardous Materials*. 199–200: 282–289.

Zhang, Z., Wang, T., Jia, M., Wei, Q., Meng, X., and Shu, G. (2014). Combustion and Particle Number Emissions of a Direct Injection Spark Ignition Engine Operating on Ethanol/Gasoline and n-Butanol/Gasoline Blends with Exhaust Gas Recirculation. *Fuel*. 130: 177–188.

Zhao, F., Lai, M., and Harrington, D. (1997) A Review of Mixture Preparation and Combustion Control Strategies for Spark-Ignited Direct-Injection Gasoline Engines. *SAE International*. Doi: 10.4271/970627.

Zhao, F., Lai, M., and Harrington, D. (1999) Automotive Spark-Ignited Direct-Injection Gasoline Engines. *Progress in Energy and Combustion Science*. 25: 437–562.

Zhu, J., Lee, K. O., Yozgatligil, A., and Choi, M. Y. (2005). Effects of Engine Operating Conditions on Morphology, Microstructure, and Fractal Geometry of Light-Duty Diesel Engine Particulates. *Proceedings of the Combustion Institute*. 30(2): 2781–2789.

Appendices

Appendix A: Chapter 2 Supplemental Information

Description of Research Engine

Table A1: Single cylinder research engine specifications.

Base Engine	Westport 15 L HD
Bore, stroke, connecting rod length	137 mm, 169 mm, 261 mm
Swept volume per cylinder	2.49 L
Compression ratio	17:1
Valves	4 per cylinder; Maximum lift: intake: 13.9 mm, exhaust: 14.4 mm
Air handling	Air compressor, back pressure valve, charge heater / cooler, cooled EGR
Injector	Westport Innovations J36 Injector
Injector hole number / angle	Diesel: 7 / 18^{o}; Gas: 9 / 18^{o}

Determining Mass Volatile Fraction through DMA-CPMA Measurements

The mass fraction of volatile material within a single particle (internally mixed volatility) is defined as the mass of volatile material condensed on a particle divided by the total mass of the internally mixed particle. The mass volatile fraction (f_m) can be calculated using the mass of a mobility-classified particle with and without the denuder between DMA1 and the CPMA (Figure 2.2). This approach requires that the mass peak corresponding to the internally mixed particles is correctly identified in the CPMA mass spectra. This is potentially complicated if internally and externally mixed particles have very different densities, resulting in multiple or broadened peaks. Fortunately, it was not difficult to identify the correct peaks, as shown in Figure A1. The figure shows CPMA mass spectra of DMA-selected particles (undenuded and using the same DMA and CPMA resolution) of mode B75 20% EGR (low number volatile fraction) and B25 20%

EGR (high number volatile fraction, ~45%). If the effective densities of the volatile particles and the internally-mixed particles were significantly different, one would expect to see two peaks or a broadening of the mass spectra for the case of B25 20% EGR. However, the mass spectra of B25 20% EGR and B75 20% EGR have a single peak and almost identical widths, meaning that effective densities of the volatile particles and the internally-mixed particles in mode B25 20% EGR are almost identical. This would be expected if the volatile material would contribute to most of the mass of the internally-mixed particle. Given that these effective densities are almost the same, we can define the mass volatile fraction of the internally mixed particles as the ratio of the volatile mass on the particle divided by the total mass of the particle.

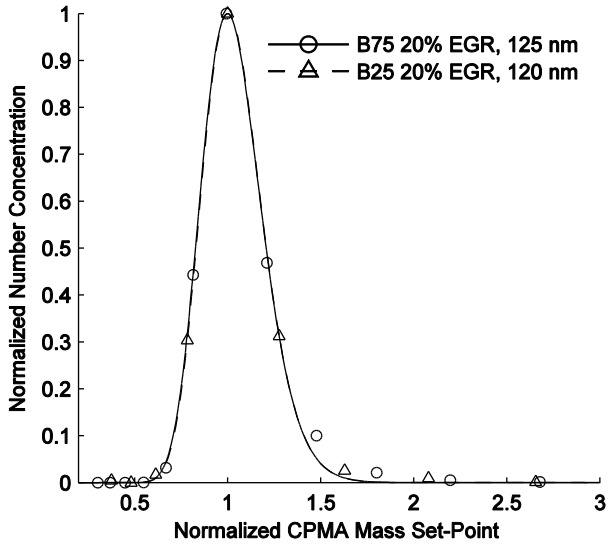

Figure A1: Normalized undenuded CPMA mass spectra from modes B75 20% EGR and B25 20% EGR for DMA-selected mobility-equivalent diameters of 125 nm and 120 nm, respectively. In both cases the resolution of the DMA and CPMA were 10 with respect to mobility and mass.

Size Segregated Volume Volatile Fraction

In addition to the mass volatile fraction, internally mixed volatility can also be expressed using the volume volatile fraction (f_v). f_v can be determined by calculating the difference in volume between the undenuded and denuded particles and dividing it by the undenuded particle volume, assuming spherical particles. The volume volatile fractions as a function of mobility-equivalent diameter are plotted in Figure A2.

Because f_v assumes spherical particles, its resemblance to f_m is closest for particles with larger mass-mobility exponents. The comparison between f_v and f_m is illustrated in Figure A3 using the ratio of the two fractions. This ratio is nearest to unity for the smallest mobility-equivalent diameters of modes B25 20% EGR and B37 20% EGR. The high mass-mobility exponents and low number of primary particles lead to nearly spherical aggregates and their mass and volume of volatile material will correlate well. However as mobility-equivalent diameter increases, the aggregates become less spherical and the agreement between the two volatile fractions is diminished, with f_v being smaller than f_m. The low volatility of the higher-load conditions results in a relatively large amount of uncertainty between f_v and f_m, as seen with modes B75 20% EGR and B50 20% EGR which have ratios which range from approximate 0.5 to 2.

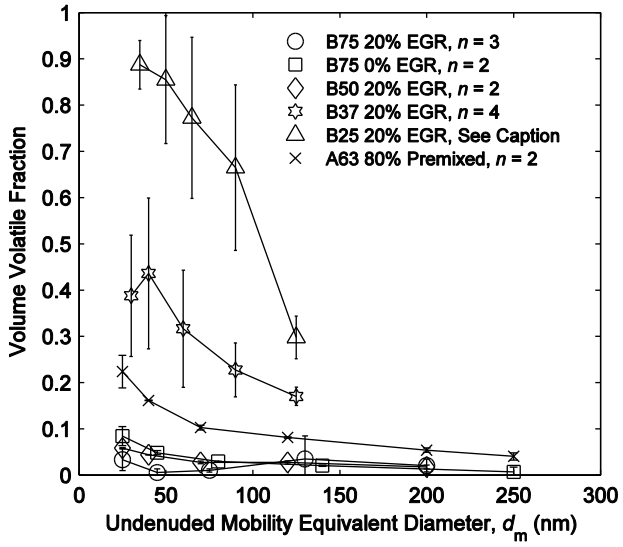

Figure A2: Volume volatile fraction of exhaust particles. Error bars represent one standard deviation. Mode B75 20% EGR at 45 nm was reproduced n = 2 times, and mode B25 20% EGR was reproduced n = 5 times at 35 nm, n = 4 times at 50 and 65 nm, and n = 3 times at 90 and 125 nm.

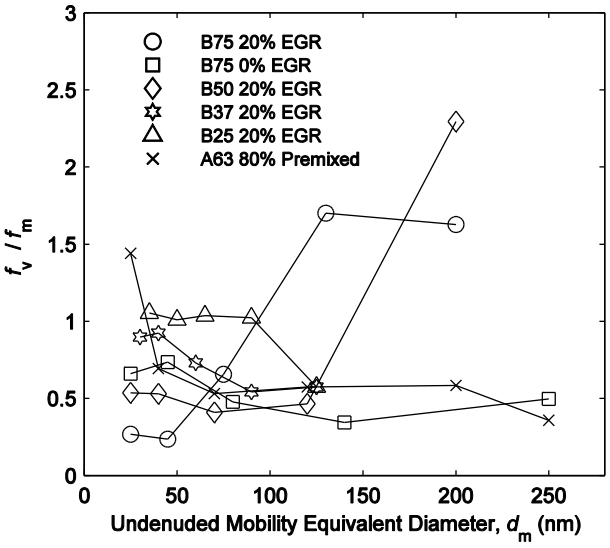

Figure A3: Size segregated ratio of volume volatile fraction to mass volatile fraction.

Summary of Transmission Electron Microscopy Analysis

Table A2: Summary of TEM image processing results.

Mode	B25 20% EGR	B37 20% EGR	B50 20% EGR	B75 20% EGR	B75 0% EGR	A63 80% Premixed
N_{p}	238	529	836	1373	729	824
N_{agg}	38	66	107	142	93	89
d_{p} (nm)	21.0 (±10.1)	13.5 (±4.1)	14.4 (±5.5)	25.7 (±7.8)	18.6 (±6.4)	19.9 (±9.4)
Mean d_{a} (nm)	80.9 (±53.4)	56.3 (±24.2)	76.6 (±48.8)	123.3 (±76.9)	82.1 (±52.6)	95.0 (±80.9)
Geometric mean d_{a} (nm)	68.1	55	63.6	105.9	69.6	66.8
Gyration radius R_{g} (nm)	38.2 (±33.2)	25.3 (±13.4)	38.1 (±26.9)	62.6 (±45.6)	40.0 (±31.3)	50.0 (±52.1)
k_{TEM}	3.00 (0.84, 5.17)*	3.08 (1.84, 4.31)	7.93 (5.35, 10.51)	14.58 (10.82, 18.35)	12.12 (7.32, 16.91)	5.09 (3.35, 6.83)
D_{TEM}	0.44 (0.28, 0.6)	0.37 (0.27, 0.46)	0.14 (0.06, 0.21)	0.12 (0.06, 0.17)	0.10 (0.01, 0.19)	0.28 (0.21, 0.36)
R^2	0.44	0.46	0.10	0.12	0.05	0.42

* Numbers in parenthesis for k_{TEM} and D_{TEM} represent 95% confidence intervals.

N_{p} and N_{agg} are the measured total number of primary particles and aggregates, respectively. d_{p} and d_{a} are the diameters of the primary particles and projected area equivalent diameter of aggregates, respectively. Values shown in parenthesis for d_{p} and d_{a} are standard deviations of these parameters.

Appendix B: Chapter 3 Supplemental Information

Number and Mass Volatile Fractions

The size-segregated number volatile fractions for fuels not shown in chapter 3 are presented here. f_N for E10 and E50 is displayed in Figure B1 and Figure B2, respectively. Similarly, mass volatile fractions (f_m) as a function of mobility-equivalent diameter for E10 and E50 are shown in Figure B3 and Figure B4, respectively.

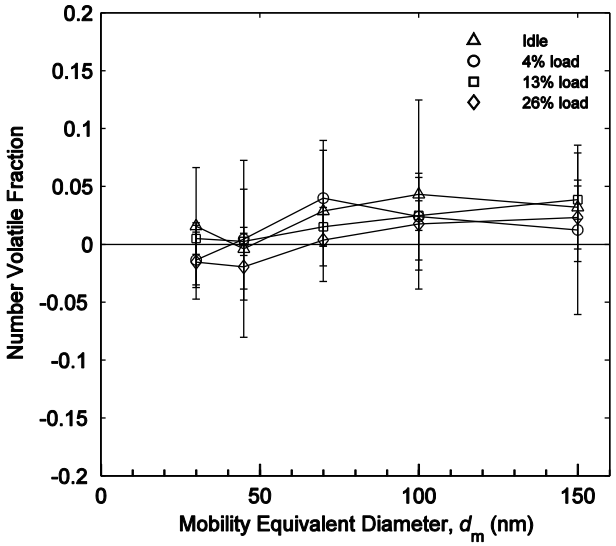

Figure B1: Size-segregated f_N for all loads using E10 fuel.

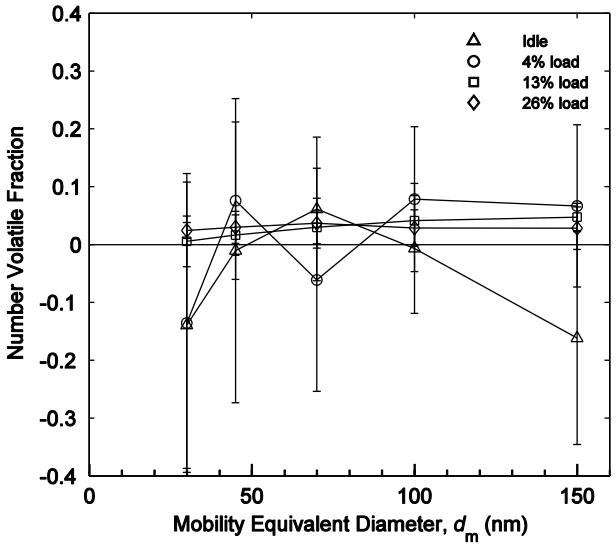

Figure B2: Size-segregated f_N for all loads using E50 fuel.

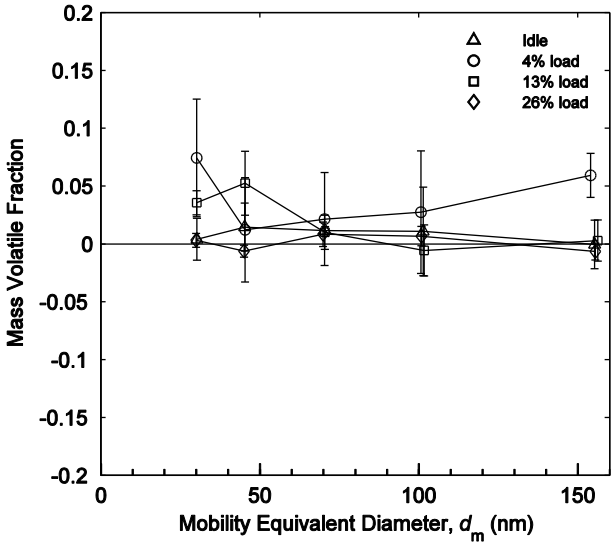

Figure B3: Size-segregated f_m for all loads using E10 fuel.

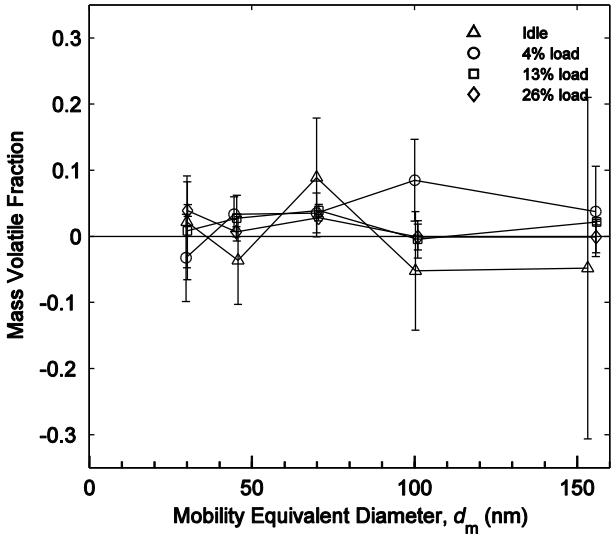

Figure B4: Size-segregated f_m for all loads using E50 fuel.

Appendix C: Conversion of New European Driving Cycle (NEDC) to engine speeds and loads for determination of dynamometer test points

To choose relevant dynamometer set points, the New European Driving Cycle UNECE, 2013) was converted to engine speeds and loads. Power required at each second of the drive cycle was determined, and using the car's gearing, the engine's speed and load throughout the test was computed. Engine speed can be related to the vehicle's driving speed as

$$\omega_{\mathrm{Engine}} = \frac{\vec{V}}{r_{\mathrm{w}}}(R_{\mathrm{A}})(R_{\mathrm{T}}) \,, \qquad \text{C.1}$$

$\vec{V}$ is the vehicle speed, R_{A} is the axle ratio, R_{T} is the transmission gear ratio, and r_{w} is the wheel and tire assembly radius. This is computed as

$$r_{\mathrm{w}} = \frac{d_{\mathrm{wheel}}}{2} + (d_{\mathrm{tire}})(d_{\mathrm{side}}). \qquad \text{C.2}$$

d_{wheel} is the diameter of the wheel, d_{tire} is the width of the tire, and d_{side} is the fractional thickness of the tire sidewall. Determination of engine load from a driving cycle requires that the tractive power be calculated. This can be done using the equation

$$P_{\mathrm{Trac}} = \left(F_{\mathrm{Aero}} + F_{\mathrm{Rolling}} + F_{\mathrm{Inertia}}\right)\vec{V}. \qquad \text{C.3}$$

Here, F_{Aero}, F_{Rolling}, and F_{Inertia} are aerodynamic drag, rolling resistance, and inertia forces, respectively. $\vec{V}$ is the vehicle speed. The aerodynamic drag is equal to

$$F_{\mathrm{Aero}} = \frac{1}{2}\rho C_{\mathrm{d}} A \vec{V}^2 \,, \qquad \text{C.4}$$

where ρ is the air density, C_{d} is the drag coefficient, A is the vehicle's frontal area, and $\vec{V}$ is the vehicle speed. Air density is determined using the equation

$$\rho = \frac{PM_{\mathrm{m}}}{RT} \,. \qquad \text{C.5}$$

P is the atmospheric pressure, M_{m} is the molar mass of air, R is the universal gas constant, and T is the air temperature. The rolling resistance force is equal to

$$F_{\mathrm{Rolling}} = C_{\mathrm{rr}} mg \,. \qquad \text{C.6}$$

C_{rr} is the rolling resistance coefficient, m is the vehicle mass, and g is the acceleration due to gravity. The inertia force is

$$F_{\text{Inertia}} = ma \,. \qquad \text{C.7}$$

Here, a is the longitudinal acceleration. The required engine load can then be determined using the tractive power and the engine speed:

$$T_{\text{Engine}} = \frac{P_{\text{Trac}}}{(1-\alpha)\omega_{Engine}} \,. \qquad \text{C.8}$$

Here, α is the percentage of power lost in the powertrain. The values for the constants used in these equations are listed in Table C1. Transmission ratios are shown in Table C2.

Table C1: Constants used for engine load and speed calculations.
Dimensions are for 2009 Chevrolet Cobalt SS.

Air Temperature, *T* (K)	298
Air pressure, *P* (kPa)	101.3
Universal Gas Constant, *R* (kJ/kmol/K)	8.314
Molar Mass of Air, M_m (kg/kmol)	28.97
Drag Coefficient, C_d	0.34 (Edmunds)
Frontal Area, *A* (m^2)	1.95 (Estimation)
Vehicle Mass, *m* (kg)	1360 (Edmunds)
Rolling Resistance Coefficient, C_{rr}	0.014 (Wong, 2001)
Gravitational Acceleration, *g* (m/s^2)	9.81
Wheel Size, d_{wheel} (inch)	18 (EPA, 2008)
Tire Width, d_{tire} (mm)	225 (EPA, 2008)
Fractional Sidewall Thickness, d_{side}	0.4 (EPA, 2008)
Powertrain Losses, α	0.15 (Estimation)

Table C2: Transmission and Axle Ratios for 2009 Chevrolet Cobalt SS.*

Gear	Ratio (:1)
1st	3.58
2nd	2.02
3rd	1.35
4th	0.98
5th	0.69
Reverse	3.31
Axle	3.84

*Car and Driver

Alternatively, power required can be calculated by using the road load, as determined by the EPA. This consists of three coefficients used in a quadratic polynomial, which relates the vehicle's speed (miles per hour) to resistive force (pounds force). The equation has the form:

$$F_{\text{Road Load}} = F_0 + F_1\vec{V} + F_2\vec{V}^2 + ma \ . \qquad \text{C.9}$$

Here, $\vec{V}$ is the speed, a is the vehicle's acceleration, m is its mass, and F_0, F_1, and F_2 are the coefficients determined by the EPA (EPA, 2008). These values are outlined in Table C3.

Table C3: Road Load Coefficients
for 2009 Chevrolet Cobalt SS.*

Constant	Value
F_0	33.38
F_1	0.4264
F_2	0.01635

*EPA, 2008

When multiplied by velocity, the road load gives the required power. This value can then be used in place of the tractive power from above.

Appendix D: Determination of Particle Losses in Thermodenuder

Particle losses are incurred within the thermodenuder for two dominating reasons: diffusion and thermophoresis. These losses were quantified so upstream concentrations can be calculated. Alternatively, concentrations from the denuded line can be corrected with respect to the bypass line. The particle losses are a function of the flow rate through the denuder, so multiple flow rates were examined. The chosen flow rates were those which could be achieved with either one or two CPCs operating at low or high flow modes. Various configurations were used to achieve these flow rates and the simplest configuration, that used for 0.3 L/min or 1.5 L/min is displayed in Figure D1.

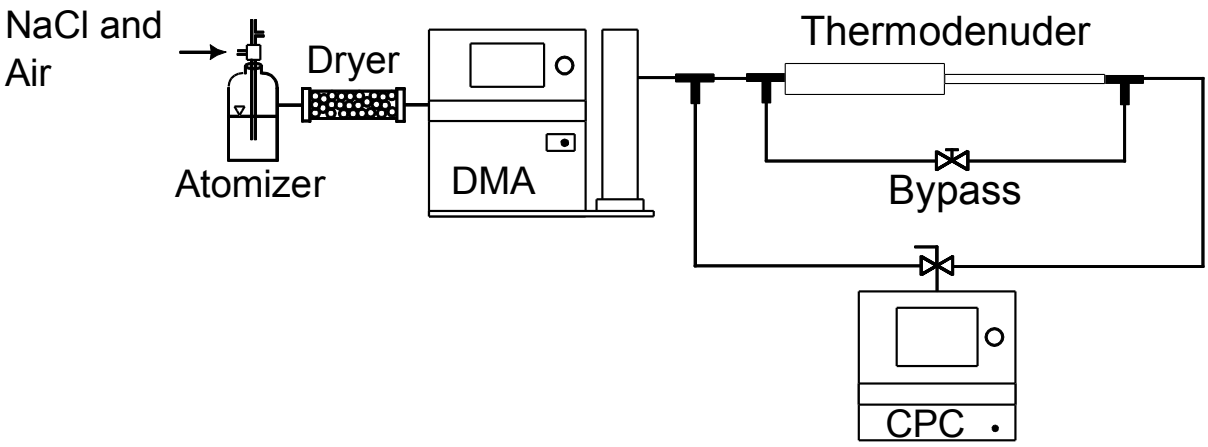

Figure D1: Experimental setup for thermodenuder losses at 0.3 L/min or 1.5 L/min.

Particles were generated by atomizing salt water then passing it through a dryer. The particles were sent to a 3081 series DMA at which point a mobility-equivalent diameter was selected. The resultant concentration was measured with a 3776 series CPC as it exited the DMA. Concentrations were measured from the heated line as well as the unheated bypass line.

Likewise, to achieve flow rates of 0.6 L/min and 1.8 L/min, a second CPC was introduced. The CPC used to measure the concentrations was set to either its low or high flow modes (0.3 L/min and 1.5 L/min), while the secondary CPC was set to low flow mode. The setup can be seen in Figure D2.

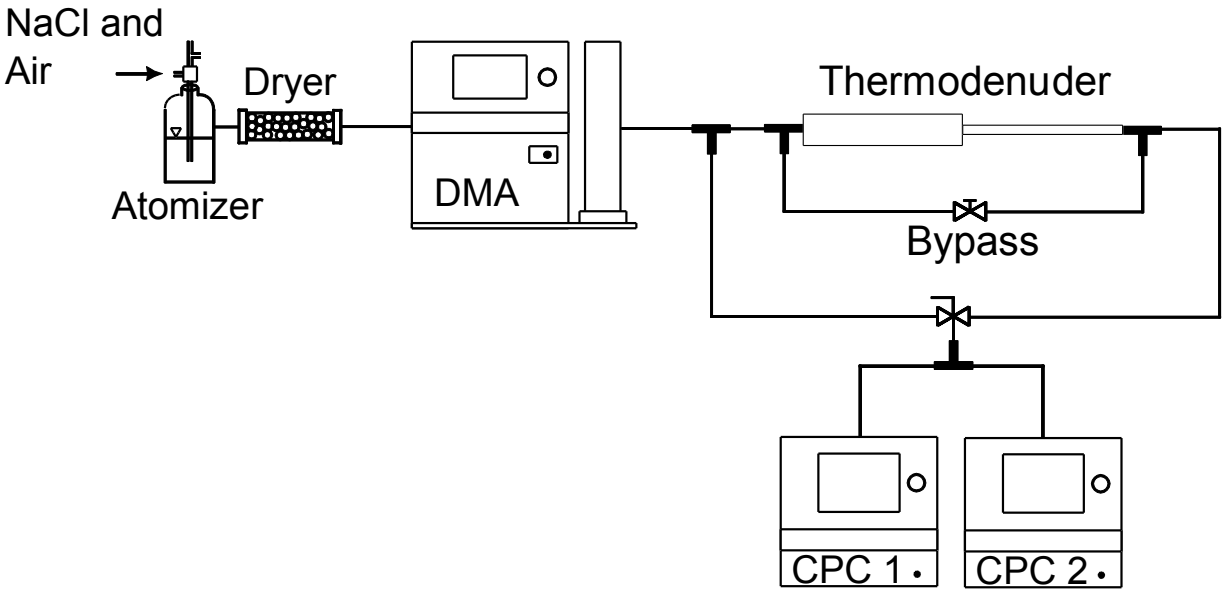

Figure D2: Experimental setup for thermodenuder losses at 0.6 L/min or 1.8 L/min.

The transmission efficiency through the denuder, η_{denude}, can be determined using the ratio of particle concentration from the heated line (denuded, N_{denude}) to that of the non-heated line (bypass, N_{bypass});

$$\eta_{\mathrm{denude}} = \frac{N_{\mathrm{denude}}}{N_{\mathrm{undenude}}}. \quad \text{D.1}$$

A sigmoidal trend was fit to the data. The trendlines have the form

$$\eta_{\mathrm{denude}} = \frac{C_1}{1+e^{-(C_2 d_{\mathrm{m}} - C_3)}} + C_4\,, \quad \text{D.2}$$

where d_{m} is particle mobility-equivalent diameter and C_1,C_2, C_3, and C_4 are manipulated parameters which control the sigmoid's amplitude, horizontal stretch, horizontal offset, and vertical offset, respectively. The transmission efficiency with respect to the bypass line for 1.5 L/min is shown as an example in Figure D3.

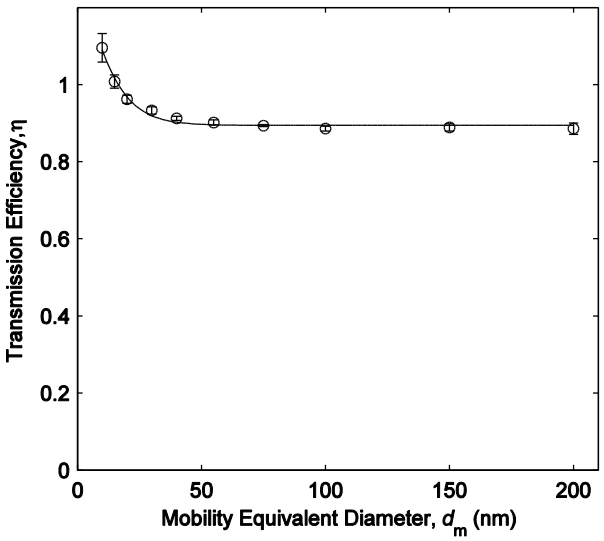

Figure D3: Size-segregated transmission in relation to bypass line for thermodenuder. Error bars are one standard deviation.

Appendix E: Determination of Dilution Ratio and Particle Losses in Diluter

To prevent condensation of water water droplets from engine exhaust, a Dekati DI-1000 ejector diluter was used to lower the partial pressure of the water vapour in the sample line. The dilution ratio must be determined to compensate for the associated drop in number concentation. Moreover, the losses within the diluter must be determined. A single stage of the diluter was used. The experimental setup used to measure the dilution ratio is shown in Figure E1.

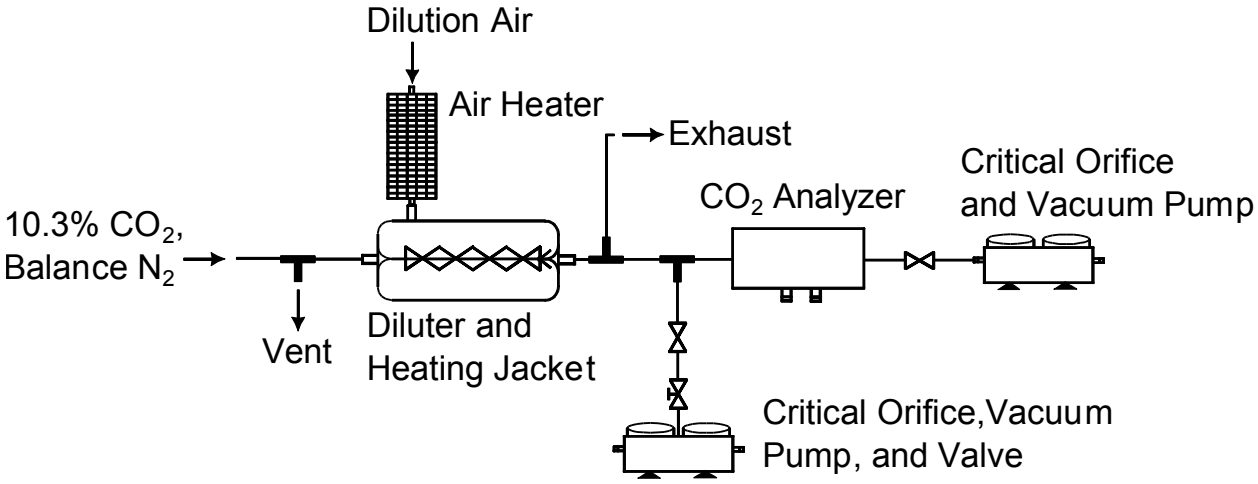

Figure E1: Experimental setup used for testing dilution ratio.

A bottle of CO_2 (balance Nitrogen) was first tested with a Vetronix PXA-1100 exhaust gas analyzer, and found to have a CO_2 concentration of 10.3%. The bottle was then connected to the dilution system. Dilution air with a known CO_2 concentration was then passed into the system at 2 Bar (gauge). A variable flowrate of sample gas was taken using two vacuum pumps. One pump pulled flow through a LI COR LI-840A CO_2 analyzer at a constant rate of approximately 0.3 L/min using a critical orifice. The second pump was also choked with a critical orifice: limiting its maximum flowrate. A valve was adjusted to vary the total sample flow pulled from the diluter, to check that the dilution ratio is relatively independent of sample flowrate. The dilution ratio (β) can be calculated using

$$\beta = \frac{\varphi_1 - \varphi_{da}}{\varphi_2 - \varphi_{da}} , \qquad \text{E.1}$$

where φ_1 is the upstream concentration of CO_2, φ_2 is the downstream CO_2 concentration, and φ_{da} is the CO_2 concentration in the dilution air (Giechaskiel et al. 2009). The dilution ratio as a function of sample flowrate is displayed in Figure E2.

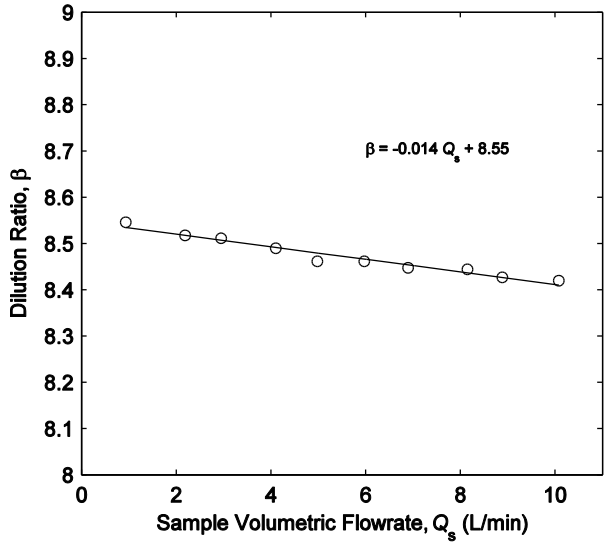

Figure E2: Dilution ratio as sample flowrate is varied.

A linear decrease is seen in dilution ratio as sample flow rate (Q_S) is increased. Between approximately 1 and 10 L/min, the dilution ration varies by 0.13, or 1.5% of its value. This change is sufficiently low, such that the dilution ratio is approximately constant over the range in flowrate.

The diluter transmission efficiency was also quantified over a range of DMA (TSI Inc., 3081 series) classified particle sizes. The dilution ratio was calculated using two methods: the first was with measurements of the CO_2 concentrations before and after the diluter. The second method used mass flowrate measurements of the gas streams. The CO_2 method was performed once, then the bottle was substituted for dry, filtered air. The flowrate method was performed for every particle loss data point. The experimental setup for this section can be seen in Figure E3.

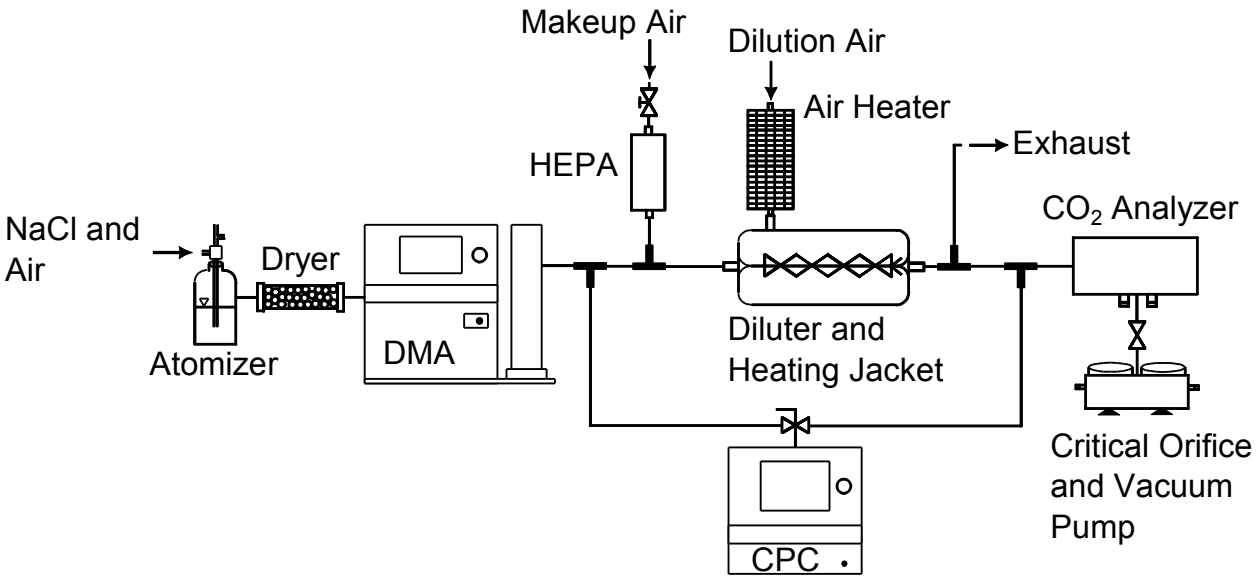

Figure E3: Experimental setup used for measuring PM transmission efficiency through diluter.

The CO_2 bottle was connected to the DMA inlet. The DMA outlet mixed with a filtered air stream so the diluter could achieve its natural inlet flowrate. DMA and makeup air volumetric flowrates were measured with a Gillibrator bubble flow meter, where the dilution air flowrate was measured with a wide-open analog mass flow controller. The valve on the makeup air stream was adjusted so that the DMA aerosol flow was 1.5 L/min.

A salt solution was atomized (TSI Inc., 3076 series) and passed through the DMA. Mobility-equivalent diameters were selected, and their concentrations were measured upstream and downstream of the makeup air and diluter using a CPC (TSI Inc., 3776 series). For each particle size, the DMA flowrate, makeup air flowrate, dilution air flowrate, and internal DMA pressure were recorded. The dilution ratio (β) was calculated from mass flowrates, using the equation

$$\beta = \frac{\dot{m}_{DMA}+\dot{m}_{da}+\dot{m}_{makeup}}{\dot{m}_{DMA}}, \qquad \text{E.2}$$

where $\dot{m}_{DMA}$, $\dot{m}_{da}$, and $\dot{m}_{makeup}$ are the mass flowrates of the DMA, dilution air and makeup air streams, respectively. The transmission efficiency through the diluter can be calculated using the formula

$$\eta_{\text{dilute}} = \frac{N_2 \beta}{N_1}, \qquad \text{E.3}$$

where N_1 and N_2 are the upstream and downstream particle concentrations respectively. While the dilution ratios calculated from the CO_2 method and flowrate method were similar, the flowrate method was used for subsequent calculations because it could be determined for each individual test. The PM tranmission efficiency for the diluter is plotted in Figure E4. The highest losses occur at the smallest particle sizes. Also of interest is the slight drop in transmission efficiency seen at the large end of the size distribution. This could be attributed to impaction losses.

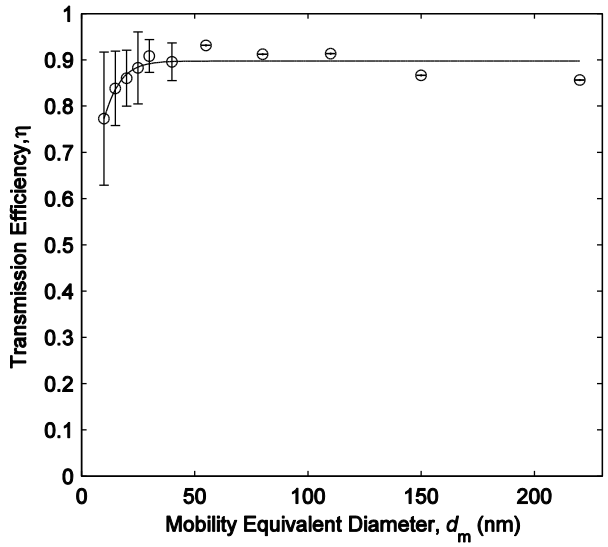

Figure E4: Relation between PM transmission efficiency and mobility-equivalent diameter for one diluter stage.